Atomic-Scale Scanning Transmission Electron Microscopy and First-Principles Study of Functional Oxides

by

Liang Hong
B.Sc. (Dalian University of Technology, China) 2012

Thesis submitted in partial fulfillment of the requirements
for the degree of Doctor of Philosophy in Physics
in the Graduate College of the
University of Illinois at Chicago, 2018

Chicago, Illinois

Defense Committee:
Robert F. Klie, Chair and Advisor
Serdar Öğüt, Co-Advisor
Hyowon Park
Alan W. Nicholls, Research Resource Center
Ravi Droopad, Texas State University

To my parents,

Lingzhen Wang and Ming Hong,

and my girlfriend,

Lingwen Luo,

whose love encourages me towards excellence.

ACKNOWLEDGMENTS

I would first like to thank my advisor, Dr. Robert Klie, for his continuous guidance and support during my Ph.D. research. It was a real privilege and an honor for me to share of his exceptional knowledge and charming personality. Dr. Klie provided me with the opportunities to learn and use the most advanced electron microscopy techniques but also the chances to communicate with extraordinary researchers all around the world. I could not have imagined having a better advisor for my Ph.D. study. Besides my advisor, I would like to express my sincere gratitude to my co-advisor, Dr. Serdar Öğüt. He is the most knowledgeable and brilliant theoretical physicist I have known, and I always enjoyed the conversation with him. His insightful comments and guidance helped me in all the time of my Ph.D. research and writing of this dissertation. I would like to thank Dr. Alan Nicholls for teaching me electron microscopy and assisting me with my experimental problems. This work could never be done successfully without the help from Dr. Nicholls, who maintained the lab work highly efficient. I would also like to thank the rest of my dissertation committee members, Dr. Ravi Droopad and Dr. Hyowon Park, for generously offering their time and guidance throughout the preparation and review of this dissertation. In addition, I would like to thank every other member in the Nanoscale Physics group: Xuan Hu, Xue Rui, Jinglong Guo, Bilash KC and Dr. Jacob Jokisaari, as well as the past members: Dr. Arijita Mukherjee, Dr. Canhui Wang, Dr. Ahmet Gulec, Dr. Tadas Paulauskas and Dr. Patrick Phillips. I really enjoyed the wonderful time learning and working with all of them.

ACKNOWLEDGMENTS (Continued)

This work was supported by the National Science Foundation (Grant No. DMR-1408427) and used resources of the National Energy Research Scientific Computing Center, a DOE Office of Science User Facility supported by the Office of Science of the U.S. Department of Energy under Contract No. DE-AC02-05CH11231. The acquisition of University of Illinois at Chicago (UIC) JEOL JEM ARM200CF is supported by an MRI-R^2 grant from the National Science Foundation (Grant No. DMR-0959470). This work also made use of instruments in the Electron Microscopy Service and the High Performance Computing Clusters at Research Resources Center, UIC.

CONTRIBUTION OF AUTHORS

The oxide-semiconductor heterostructure samples used in Chapter 3 were integrated by Dr. Ravi Droopad's group in Texas State University. The TEM sample used for *in-situ* electrical experiment in Chapter 3 was prepared by Dr. Daniel Huber in Ohio State University. The lithium cobalt oxide nanoplatelets sample used in Chapter 5 was synthesized and prepared by Dr. Jordi Cabana's group in UIC. The X-ray absorption spectroscopy data in Chapter 5 were acquired by Dr. Linhua Hu in UIC and Dr. John Freeland in Argonne National Laboratory. The barium titanate nanocube samples used in Chapter 6 were synthesized and prepared by Dr. Gabriel Caruntu's group in Central Michigan University.

TABLE OF CONTENTS

TABLE OF CONTENTS (Continued)

CHAPTER **PAGE**

LIST OF TABLES

LIST OF FIGURES

LIST OF FIGURES (Continued)

FIGURE **PAGE**

LIST OF FIGURES (Continued)

LIST OF FIGURES (Continued)

FIGURE **PAGE**

LIST OF FIGURES (Continued)

FIGURE **PAGE**

LIST OF FIGURES (Continued)

FIGURE **PAGE**

LIST OF FIGURES (Continued)

FIGURE **PAGE**

LIST OF FIGURES (Continued)

FIGURE **PAGE**

LIST OF ABBREVIATIONS

ABF	Annular bright-field
ADF	Annular dark-field
ANR	Armchair nanoribbon
BF	Bright-field
CBM	Conduction band minimum
DFT	Density functional theory
DOS	Density of states
EC	Electron counting
EEL	Electron energy-loss
EELS	Electron energy-loss spectroscopy
EDS	Energy dispersion spectroscopy
ELNES	Energy-loss near-edge structure
FEG	Field-emission gun
FIB	Focused ion beam
GGA	Generalized gradient approximation
HAADF	High-angle annular dark-field
HPC	High-performance computing

LIST OF ABBREVIATIONS (Continued)

LAADF	Low-angle annular dark-field
LDA	Local-density approximation
MBE	Molecular beam epitaxy
MOS	Metal-oxide-semiconductor
PAW	Projector-augmented-wave
ROI	Region of interest
STEM	Scanning transmission electron microscopy/microscope
TEM	Transmission electron microscopy/microscope
TEY	Total electron yield
UIC	University of Illinois at Chicago
VASP	Vienna Ab initio Simulation Package
VBM	Valence band maximum
XAS	X-ray absorption spectroscopy
XANES	X-ray absorption near-edge structure
XRD	X-ray diffraction
ZLP	Zero-loss peak
ZNR	Zigzag nanoribbon
1D	One-dimensional

LIST OF ABBREVIATIONS (Continued)

2D	Two-dimensional
2DEG	Two-dimensional electron gas

SUMMARY

Nanostructured transition-metal oxides have shown fascinating physical properties such as ferroelectricity, ferromagnetism and superconductivity. Most of these remarkable properties stem from the interplay between spin, lattice, charge, and orbital degrees at nanoscale surfaces, edges, defects and interfaces that are present in the nanostructures. In this Ph.D. dissertation, I investigate the atomic-scale structures and properties of several representative types of functional transition-metal oxide nanomaterials, including strontium titanate and barium titanate thin films, oxygen-functionalized MXene nanoribbons, lithium cobalt oxide nanoplatelets, and barium titanate nanocubes, using scanning transmission electron microscopy techniques and first-principles density functional theory simulations. The electronic properties of strontium titanate and barium titanate thin films with gallium arsenide are found to be correlated to the atomic arrangement and vacancies at the interfaces. The semiconducting property of MXene nanoribbons is demonstrated to be dependent on the size and edge shape of the nanoribbons. Lithium cobalt oxide nanoplatelets exhibit surface magnetism which are found to be tunable via introduction of aluminum. Ferroelectric orders in barium titanate nanocubes are found to be affected by surface and size effects. My research results reveal the importance of the structural confinement, atomic arrangement and bonding states between transition-metal and oxygen atoms to the physical properties of oxide materials. A fundamental understanding of the structure-property relationship in these oxide nanomaterials advances our ability to design and develop novel functional devices at nanoscale.

CHAPTER 1

INTRODUCTION

Transition-metal oxides are known to possess a rich variety of functionalities due to the unique nature of the transition-metal *d*-electrons. They have been widely used for device applications including high-mobility transistors, gas sensors, non-volatile memories and energy-conversion devices. Nanostructured transition-metal oxides, on the other hand, exhibit fascinating physical properties, such as magnetism, ferroelectricity, piezoelectricity and superconductivity. Most of these remarkable properties originate from the interplay between spin, lattice, charge, and orbital degrees of freedom of the oxide materials [1], and are tunable through engineering their structures and/or compositions. For instance, the dielectric and magnetic properties of perovskite oxide thin films are known to be strong functions of the oxygen stoichiometry. Furthermore, the stability and functionality of the oxide materials are often governed by the presence of atomic-scale surfaces, edges, defects and interfaces, which are unavoidable in nanostructures such as thin films, nanoparticles, one-dimensional and two-dimensional materials. Accordingly, fundamental research of the structure-property relationship of the transition-metal oxides at atomic scale is essential to continuing the design and development of novel devices at nanoscale.

Aberration-corrected scanning transmission electron microscopy (STEM) techniques provide the opportunity of achieving both high spatial resolution and high energy resolution for studying the oxide materials. In particular, by using the correlated annular dark/bright field

imaging and electron energy loss spectroscopy (EELS), the structure, composition and bonding can be quantitatively characterized at atomic scale. Additionally, the effects of localized structures, such as defects and interfaces, on the physical properties of the oxide materials can be tested inside the microscope column at atomic resolution by *in-situ* electrical, heating or cooling experiments. First-principles density functional theory (DFT) calculations, on the other hand, capable of offering robust predictions for the atomic and electronic structures of complex materials, have become affordable through high-performance computing (HPC) clusters. DFT modeling provides insights not only into the lowest-energy structures, but also into the atomic-scale behavior of materials. By combining the STEM experiments with DFT modeling, one can test and validate the theoretical models in terms of developing sophisticated models of atomic-scale structures, as well as understanding the fundamental physics of the materials beyond the limitation of either experimental characterization alone or theoretical prediction alone.

The general purpose of this Ph.D. study is to investigate the atomic-scale models that are used to describe the boundaries and defects in nanostructured transition-metal oxides with respect to their functionalities. In this dissertation, several types of functional oxide nanostructures, including strontium titanate ($SrTiO_3$) and barium titanate ($BaTiO_3$) thin films, oxygen-functionalized MXene nanoribbons, lithium cobalt oxide ($LiCoO_2$) nanoplatelets and $BaTiO_3$ nanocubes, will be studied focusing on their crystal structures, transition-metal $3d$ and oxygen $2p$ states, and the tunable physical properties, using atomic-resolution STEM charac-

terization and first-principles DFT calculations. The rest of this dissertation is organized as follows.

In Chapter 2, the physical principles behind the experiment and modeling techniques are discussed. The experimental part includes the theoretical background of the aberration-corrected STEM and EELS, the practical sample preparation process, and the JEOL ARM200CF STEM at University of Illinois at Chicago. The modeling part includes the quantum mechanics basis of DFT, and the software used for running calculations. In Chapter 3, the heterostructures of $SrTiO_3$ and $BaTiO_3$ thin films with GaAs are studied to explore the growth mechanism and electronic properties of epitaxial oxide thin films, as well as the effects of interfacial defects. The atomic structure of the heterointerface is characterized, and the interfacial vacancies are found to play an important role in determining the electronic properties. Intrinsic two-dimensional electron gas is predicted to present at the $SrTiO_3$/GaAs interface, and can be tuned through the interfacial vacancies. In addition, ferroelectric switching in $BaTiO_3$ thin film on $SrTiO_3$/GaAs substrate is directly observed through STEM-EELS imaging. In Chapter 4, a novel class of two-dimensional materials, known as MXenes, is studied with the focus on the edge- and size-dependent properties of Ti_2CO_2 and Sc_2CO_2 nanoribbons. The semiconducting versus metallic property is found to be dependent on the two edge types (armchair versus zigzag) of the nanoribbon. Electron counting rule and quantum confinement are successfully used to explain the nature of band gap variation. In Chapter 5, Al-doped $LiCoO_2$ nanoplatelets are investigated to explore the surface electronic structure of the particle in terms of enhancing surface stability and chemical performance. Intermediate and high spin state Co^{3+} is found to

present at the particle surfaces with tunable concentration by introduction of Al. In Chapter 6, the ferroelectric patterns in $BaTiO_3$ nanocubes with different sizes are studied. The surface and size effects on the local polar distortion are discussed. Finally, my conclusions from current results and outlook on the future work are summarized in Chapter 7.

CHAPTER 2

METHODS

2.1 Scanning Transmission Electron Microscopy

A scanning transmission electron microscope (STEM) is a type of transmission electron microscope (TEM) with electron beam focused to a small probe and scanned across the specimen in a raster illumination system. The first STEM was designed and constructed by Manfred von Ardenne in 1937. He demonstrated an image of ZnO crystals with a spatial resolution of 40 nm in his 1938 paper [2]. The technique was not developed further until 1969, when Albert Crewe developed the field-emission gun and added a high-quality objective lens to build a modern STEM [3]. Nowadays, high-resolution STEM has become a powerful and versatile instrument for characterization and analysis of nanoscale materials. The addition of aberration correction to a STEM enables electron probes to be focused to sub-Angstrom (picometer) diameters, allowing direct imaging of atoms or atomic columns with unprecedented clarity. The schematic of a general aberration-corrected STEM is shown in Figure 2.1.1. The incident electron probe forms and interacts with the thin specimen, producing a wide range of signals. The commonly collected signals for characterization include the annular dark-field (ADF), the bright-field (BF), the electron energy-loss spectroscopy (EELS), and the X-ray energy dispersive spectroscopy (EDS) signals. Moreover, the correlated imaging and spectroscopic signals can be acquired simultaneously from a specific area of the specimen in the STEM.

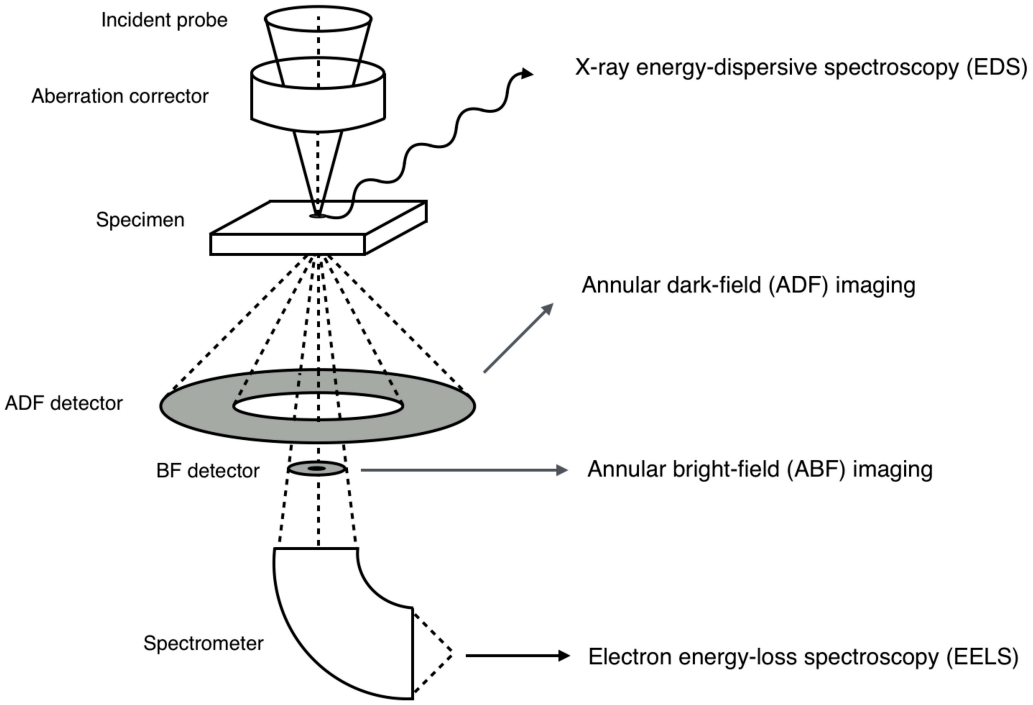

Figure 2.1.1. Schematic of a general STEM with a probe aberration corrector, ADF, BF detectors and EEL spectrometer.

2.1.1 Probe Formation

The STEM probe formation begins with the accelerated electrons from the emission source, followed by demagnification through a set of condenser lenses and an objective lens. A small probe is required for high image resolution. However, the smaller the probe, the lower the current available and the higher the brightness needed to provide a reasonable current. It is for this reason that the development of the modern STEM requires a high-brightness source [4].

There are two types of electron sources: thermionic and field-emission sources. The thermionic emission sources heat up filament and excite electrons to overcome the work function energy barrier. The sources used in thermionic emission are tungsten (W) filaments or lanthanum hexaboride (LaB_6) crystals, and are relatively blunt due to the temperature necessary to overcome the work function. On the other hand, field emission sources pull out electrons with an electrical field, which can be further enhanced in the presence of a sharp tungsten tip. Thus, field-emission gun (FEG) would provide a smaller source and render better spatial resolution. In recent years, the usage of cold FEG has seen a resurgence of interest due to the enhanced gun vacuum and emission current stability. The greatest advantage of using cold FEG sources over conventional FEG sources is the significantly improved energy resolution and thermal broadening of the source size because cold FEG sources are operated at room temperature.

Brightness (B) is the current density per unit solid angle of the source. It is defined as

$$B = \frac{I}{\pi A \theta^2,} \tag{2.1}$$

where I is the beam current, A is the area of the beam, and θ is the illumination semi-angle. The cold FEG is capable of providing a source size of 5 nm and brightness of approximately 2×10^9 $\mathrm{Asr^{-1}cm^2}$ at accelerating voltage of 100 kV [5]. Brightness scales with beam energy, hence the value can be twice or three times higher at accelerating voltage of 200 kV or 300 kV. Brightness is conserved in a perfect optical system that is free of aberrations. However, in practice, the angular aperture has to be restricted at some point in the optical column to avoid broadening the probe due to lens aberrations. This means only a small fraction of the incident

electron beam will end up in the probe. Therefore, the choice of probe size becomes a trade-off between resolution and signal-to-noise ratio [6].

2.1.2 Aberration Correction

Lens aberrations in real illumination system are inevitable and will affect the size of the probe. Therefore, aberration correction of the illumination system is important for improving the resolution of STEM images. Lens aberrations fall into two main classes: (1) Geometric aberrations due to errors in the optical path lengths, and (2) Chromatic aberration due to a spread in energy of the beam. Geometric aberrations mean that rays traveling at an angle to the optic axis are focused at a different point to rays traveling almost parallel to the optic axis, which defines the Gaussian focus point. Spherical aberration is the most well-known geometric aberration because it was the dominant aberration before correction became possible. A schematic depiction of geometric and chromatic aberration is presented in Figure 2.1.2.

With the development of aberration correctors, chromatic aberration now becomes a limiting factor while spherical aberration is the dominant factor in determining the spatial resolution. It is conventional to express the aberration function as a power series in semi-angle θ:

$$\chi(\theta) = \frac{1}{2}\Delta f\theta^2 + \frac{1}{4}C_s\theta^4 + \frac{1}{6}C_5\theta^6 + \frac{1}{8}C_7\theta^8 + ..., \tag{2.2}$$

where Δf is the defocus, C_s is the coefficient of third-ordered spherical aberration, which is the dominant geometric aberration in an uncorrected microscope, and C_5 and C_7 are the coefficients of the fifth- and seventh-order spherical aberrations, respectively. For round magnetic lenses, these are all positive coefficients and have dimensions of length. The amount of sideways

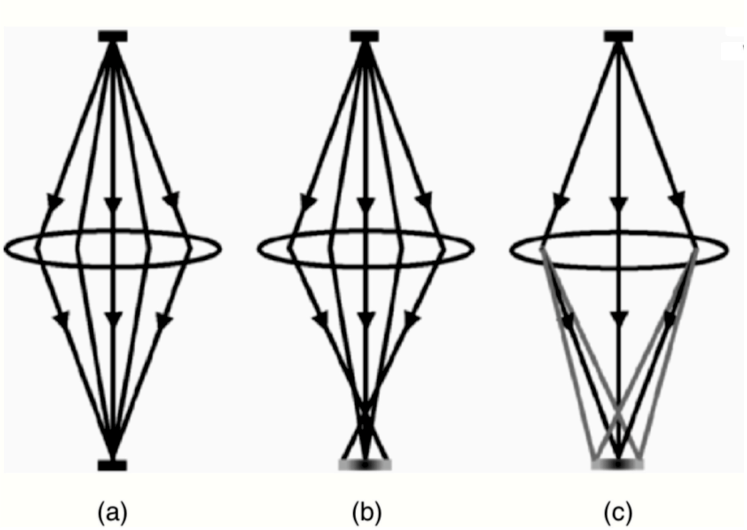

Figure 2.1.2. Schematic showing (a) a perfect lens that focuses all the rays at the same point, (b) geometric aberration that brings rays at different angles to a different focus, and (c) chromatic aberration that blurs any single ray path. Adapted from Ref. [5]. Reuse license is shown in Appendix A.

displacement δ for geometric aberrations is then expressed as the gradient of the aberration function:

$$\delta(\theta) = \Delta f\theta + C_s\theta^3 + C_5\theta^5 + C_7\theta^7 + ..., \tag{2.3}$$

which is the reason why the C_s term is referred to as third-order spherical aberration (C_3). The separate contribution of each term in Equation 2.3 is shown in Figure 2.1.3 as function of the semi-angle θ. For an uncorrected probe, the conditions around point A represent the optimum probe size. If C_3 is corrected, then the probe will be limited by C_5 and the optimum probe

will be achieved around point B, approximately a factor of two smaller. Accordingly, after the correction of C_5, the limiting geometric aberration will become C_7, and another factor of two reduction in probe size can be achieved, leading to sub-Angstrom electron probes [7].

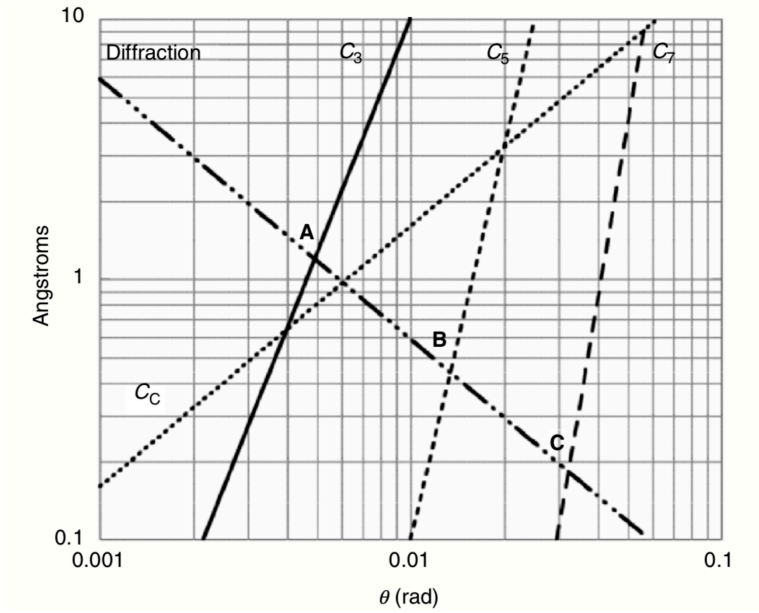

Figure 2.1.3. Sideways image spread introduced by the third-, fifth-, and seventh-order geometric aberrations, by chromatic aberration and by diffraction by the aperture of semi-angle θ. Adapted from Ref. [5]. Reuse license is shown in Appendix A.

2.1.3 STEM Imaging

After the electron probe interacts with the specimen, the scattered electrons can be collected by a bright-field (BF) detector and annular dark-field (ADF) detectors including a high-angle

annular dark-field (HAADF) detector and a low-angle annular dark-field (LAADF) detector. These detects can record images simultaneously at each focus value.

The HAADF detector is used to collect elastically scattered electrons at high angles, usually spanning from 80 to 200 mrad, to form an incoherent HAADF image. The HAADF imaging is also called Z-contrast imaging since the image intensity strongly relies on the specimen composition through the Z^2 dependence of the Rutherford scattering cross section, where Z represents atomic number [8]. In Z-contrast imaging, the total scattered electron intensity reaching the annular detector only depends on the incident intensity at each atomic site and on the atomic number of the illuminated atomic column. Thus, changing specimen thickness and defocus does not reserve the image contrast. These characteristics are important and make HAADF imaging technique useful for direct interpretation of local structures such as defects, surfaces and interfaces. Additionally, the LAADF detector is used to collect diffracted or inelastically scattered electrons at low to medium angles, usually spanning from 25 to 80 mrad. LAADF imaging can be used to probe elastic strains in crystalline specimens since LAADF image shows diffraction contrast and specimen thickness dependence.

The BF detector, on the other hand, is used to collect transmitted electrons (direct beam) to form a coherent BF image. The BF image shows phase contrast which changes with specimen thickness and electron beam defocus. Atoms appear dark on a bright background when in focus, while bright on a dark background when out of focus. The ADF and BF images are complementary and can be collected simultaneously for a comprehensive view of the specimen structures. ADF imaging is not sensitive to light elements due to the intrinsic weak electron

scattering amplitude of the light elements, whereas BF imaging is sensitive to light elements but phase contrast in BF makes direct interpretation of the images impossible. Recently, annular bright-field (ABF) imaging technique was introduced by Okunishi *et al.* [9]. The ABF method preferentially receives only the ring-shaped circumference (12 to 24 mrad) of the direct beam disk by using an inner-angle limiting disc, to block the central part of the BF disk. The greatest advantage of ABF imaging is that it enables simultaneously observation of both atomic columns of light and heavy elements with the same contrast. In addition, ABF image is composed of incoherently scattered electrons, which means more non-periodic features can be directly interpreted [10].

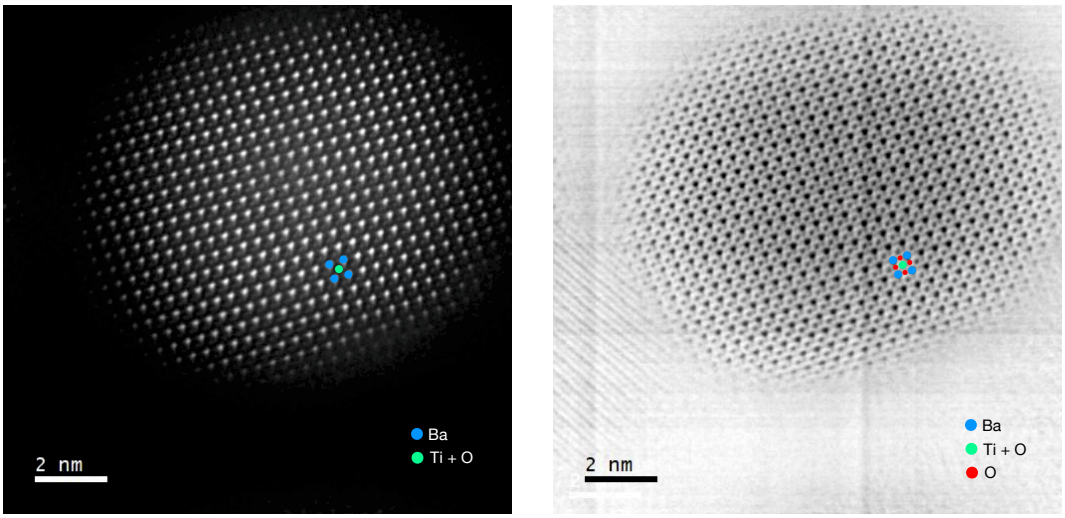

Figure 2.1.4. Atomic-resolution HAADF (left) and ABF (right) images showing the $BaTiO_3$ [100]-type structure taken from a 10-nm $BaTiO_3$ nanoparticle. The Ba, Ti+O, and O columns are marked by blue, green and red circles, respectively.

An example of the atomic-resolution HAADF and ABF images of the barium titanate ($BaTiO_3$) nanoparticle (size of 10 nm) recorded simultaneously is shown in Figure 2.1.4. In the HAADF image, Ba columns and Ti/O mixed (Ti+O) columns, which are composed of relatively heavy atoms, are clearly visualized. Additionally, the intensity of Ba columns are higher than that of the Ti+O columns since Ba ($Z = 56$) is heavier than Ti ($Z = 22$) and O ($Z = 8$). However, the light-atom O columns cannot be observed as bright spots. In the ABF image, the light-atom O columns, which cannot be seen in the HAADF image, can be clearly observed as dark spots.

2.1.4 Electron Energy-Loss Spectroscopy

When the incident electrons pass through the specimen, some of them experience inelastic scattering, resulting in the electrons in the solids undergoing transition from inner shell into the unoccupied states above the Fermi level. Electron energy-loss spectroscopy (EELS) is used for measuring the distribution of energies lost by the incident electrons. Analysis of this energy distribution can yield a variety of information about the specimen including the chemical composition, bonding, valence state, dielectric response, local electron density, band gap, and specimen thickness.

A typical EEL spectrum, shown in Figure 2.1.5 can be divided into three regions: Zero-loss peak (ZLP), low-loss and core-loss regions, each carrying characteristic information of the specimen. The ZLP corresponds to transmitted electrons without measurable energy loss, including elastically scattered electrons and those that excite phonon modes with energy loss less than the experimental energy resolution. The width of the ZLP can be used to characterize

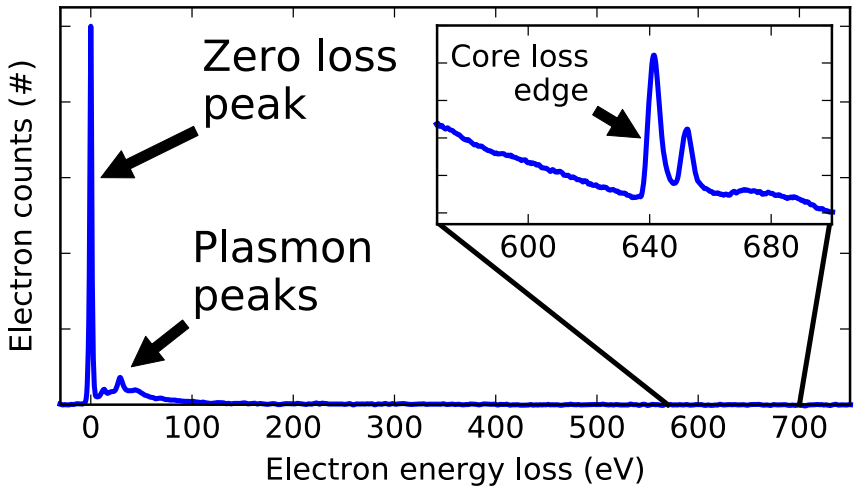

Figure 2.1.5. Example of a typical EEL spectrum, showing the major features, including the manganese core-loss edge. Attribution: Magnunor from Wikimedia Commons.

the energy resolution of the microscope. The low-loss, also known as plasmon peaks, refers to the signals from 0 to 50 eV, corresponding to the interaction of incident electrons with the outer-shell electrons. The ratio of ZLP and the integrated low-loss peaks is usually used to estimate the specimen thickness. Additionally, low-loss peaks with good enough resolution, usually requires monochromatic EELS, can be used to measure the band gap of the specimen. The core-loss refers to signals in higher energies, corresponding to the transitions from occupied core-level states to unoccupied states. The core-loss is used to determine the elements as well as studying the fine structure and chemical bonding of atoms. Unlike the low-loss peaks, the core-loss signals are in the form of sharp edges since the inner-shell intensity rises rapidly and falls slowly into higher energies. Edges corresponding to the transitions from core levels with

principal quantum number $n = 1, 2, 3, 4$ are called K-, L-, M- and N-edge, respectively. A numerical subscript is added to denote the different angular momentum j of the same quantum number of the core level. For instance, transitions from $2s$ orbitals are called L_1-edge, while transitions from $2p_{1/2}$ ($j = 1/2$) orbitals are called L_2-edge and transitions from $2p_{3/2}$ ($j = 3/2$) orbitals are called L_3-edge. The L_2-edge and L_3-edge are usually referred together as $L_{3,2}$-edge (the onset of L_3-edge is prior to that of L_2-edge) since the energy splitting is relatively small compared to the energy-loss range.

The ionization edges exhibit the fine structure, known as energy-loss near-edge structure (ELNES), which can be explained in terms of the density of states (DOS) of the atom. As shown in Figure 2.1.6, the Fermi energy is equivalent to the ionization edge onset, and the ELNES effectively mirrors the unfilled DOS above the Fermi level E_{F}. Electrons ejected from the inner shells reside preferentially in regions of the DOS that have the greatest density of unfilled states. The importance of ELNES is that the DOS is extremely sensitive to changes in the bonding or the valence state of the atom [11]. For instance, the carbon K ELNES is different for graphite, diamond and fullerene, and the shape of Ti $L_{3,2}$ ELNES changes as the valence state of Ti changes.

EELS can be performed simultaneously with ADF imaging to obtain both structural and electronic information from the specimen. However, the main limitation of the EELS technique is the effect of specimen thickness. As the specimen thickness increases, the strong interaction of primary electrons within the specimen results in the electrons undergoing plural scattering, which tends to reduce the signal-to-noise ratio of the EELS edges. This problem can be relieved

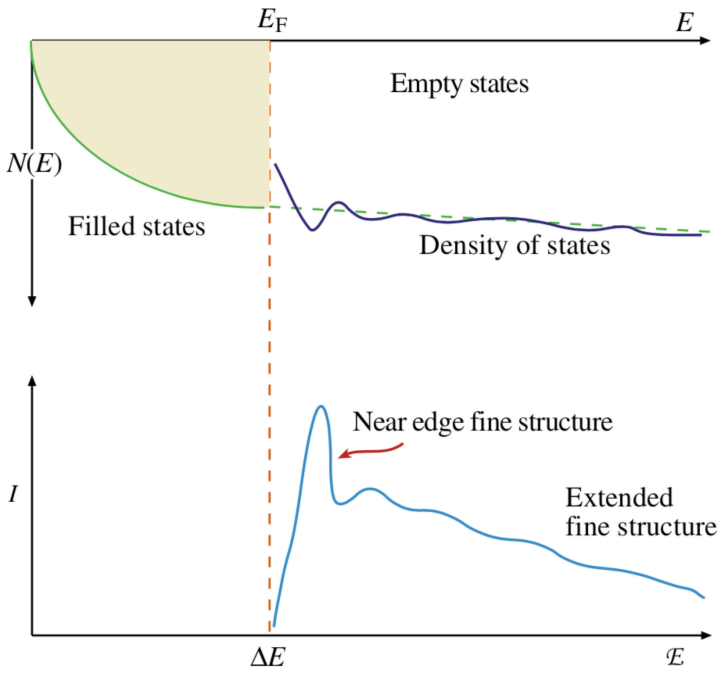

Figure 2.1.6. Relationship between the empty DOS and the ELNES intensity in the ionization edge fine structure. The filled states below E_F are drawn as a quadratic function, but this is an approximation. Adapted from [11]. Reuse license is shown in Appendix B.

by making the specimen thin enough, usually less than 50 nm, or using numerical methods such as deconvolution and principal component analysis.

2.1.5 Sample Preparation

Sample preparation is an important part of TEM characterization. There are two main principles for TEM sample preparation: 1) The sample or at least the region of interest (ROI) must be thin enough (usually < 100 nm) to achieve electron transparent; 2) The sample should

be representative of the material that is being studied. The crystal structure or composition should not be changed during the sample preparation process.

The method chosen for making a TEM sample depends on the properties of the material as well as the information is needed from the material. TEM samples are either self-supported or mounted on a grid for analysis. Copper (Cu) grids are the most commonly used for supporting TEM samples. For high temperature *in-situ* experiments, Molybdenum (Mo) grids are used due to the high melting point of Mo (2623°C). For nanoparticles, a thin carbon film is used as support. For two-dimensional materials, a holey or lacey carbon film is used as support, and the ROI should be suspended in the hole area. For thin film interfaces, a cross-section sample is made using polishing methods. In the rest of this section, I will introduce the normal procedure of preparing a wedge-shape cross-section sample for studying thin films.

The bulk specimen is cut into two 2 mm $\times$ 2 mm square slices using the diamond saw. The two slices are then glued together with the thin films in the middle using adhesive. The slice is cut into smaller size ($\sim$ 2 mm $\times$ 0.8 mm) to fit the Cu grid, and then mounted on the polishing stage for mechanical polishing. Both of the two surfaces of the slice are polished using lapping films and a wedge of $2^\circ - 3^\circ$ is made by titling the polishing stage. The thinnest part of the wedge, which is the ROI, should be polished down to 1 μm by using fine lapping films and sometime lubricant. The slice is then glued on a Cu grid with the ROI in the middle of the grid, as shown in Figure 2.1.7. The ROI in the sample is further thinned down to $<$ 100 nm using low-angle argonne ion milling. For sensitive samples, a liquid-nitrogen-cooled stage is required during the ion milling process to minimize the ion beam damage. Finally, the sample

is cleaned using chemical solutions, such as methanol and isopropyl alcohol, as well as physical cleaning by argonne and/or oxygen plasma.

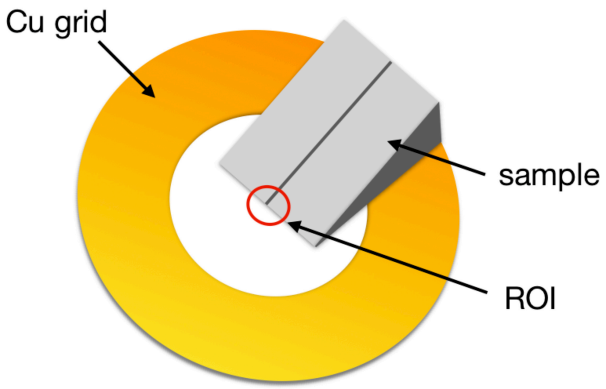

Figure 2.1.7. Schematic of the wedge-shape cross-section TEM sample mounted on Cu grid.

2.1.6 JEOL JEM-ARM200CF

The JEOL JEM-ARM200CF STEM/TEM (shown in Figure 2.1.8), equipped with a Gatan Enfina EEL spectrometer and a Oxford Instruments X-Max80 SDD EDS detector, was delivered to University of Illinois at Chicago (UIC) in July 2011, and at the time was the first aberration-corrected STEM/TEM with cold FEG in the United States [12]. The ARM200CF can be operated at acceleration voltage ranging from 80 kV to 200 kV, and is capable of routinely achieving a spatial resolution that exceeds 70 pm at 200 kV and 100 pm at 80 kV. The energy resolution of the EELS at any energy between 80 kV and 200 kV is 350 meV. The EEL

spectrometer has been upgraded to the Gatan Quantum EEL spectrometer with Dual EELS capability, and the EDS has been upgraded to the Oxford X-Max100TLE SDD X-ray detector.

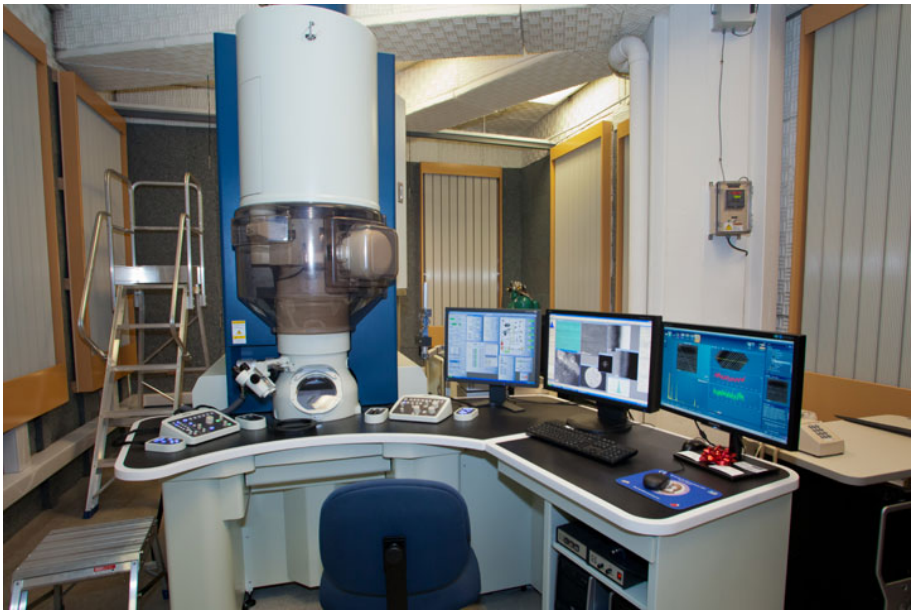

Figure 2.1.8. The JEOL JEM-ARM200CF STEM/TEM at UIC.

In addition to the standard single-tilt and double-tilt TEM holders, a variety of environmental holders, including a Gatan double-tilt heating holder (1200°C), a Gatan double-tilt cooling holder (−170°C), a Protochips Aduro double-tilt electrical/heating holder, and a Protochips Poseidon liquid holder, are available for performing *in-situ* experiments in the ARM200CF.

2.2 First-Principles Density Functional Theory

Density functional theory (DFT) is a computational quantum mechanical modeling method that has been widely used in solid-state physics, computational chemistry and materials science to study the ground-state and electronic structures of many-body systems. First-principles (also called *ab initio*) DFT calculations allow the prediction and simulation of material behavior on the basis of quantum mechanical theories, without requiring empirical parameters [13]. DFT has been very popular for calculations in solid-state physics since the 1970s. However, DFT was not considered accurate enough for calculations in quantum chemistry until the 1990s, when the approximations used in the theory were greatly refined to better calculate the exchange-correlation interactions. Despite these improvements, DFT still has difficulties in describing phenomena such as intermolecular interactions, transition states, band gaps in semiconductors, and some strongly correlated systems. The recent development of new DFT methods that are designed to overcome these problems by alterations to the exchange-correlation functional [14] or by the inclusion of empirical corrections [15; 16; 17; 18].

2.2.1 Born-Oppenheimer Approximation

For many-body systems in a solid, the Schrödinger equation with Hamiltonian, which involves both electronic and ionic degrees of freedom, as well as the electron-electron and electron-ion interactions, is not solvable exactly. The Born-Oppenheimer approximation is the assumption that the motion of atomic nuclei (ions) and electrons can be separated. Based on the huge difference of mass between ions and electrons, the ions can be viewed as classical particles which move slowly in space while the electrons respond instantaneously to any ionic motion. There-

fore, the ionic degrees of freedom can be simply treated as parameters, and the Hamiltonian has the explicit dependence on the electronic degrees of freedom alone.

The stationary electronic state of a solid is then described by a wavefunction $\Psi(\vec{r}_1, ..., \vec{r}_N)$ satisfying the N-electron Schrödinger equation written as

$$\hat{H}\Psi = \left[\hat{T} + \hat{V} + \hat{U}\right]\Psi = \left[\sum_i^N \left(-\frac{\hbar^2}{2m_i}\nabla_i^2\right) + \sum_i^N V(\vec{r}_i) + \sum_{i<j}^N U(\vec{r}_i, \vec{r}_j)\right]\Psi = E\Psi, \qquad (2.4)$$

where $\hat{H}$ is the Hamiltonian, $\hat{T}$ is the kinetic energy, $\hat{V}$ is the potential energy from the external field due to positively charged nuclei, $\hat{U}$ is the electron-electron interaction energy, and E is the total energy.

Even with this simplification, however, solving the equation for $\Psi(\vec{r}_1, ..., \vec{r}_N)$ is still a difficult task due to the complicated nature of the electrons such as the exchange and correlation properties. Scientists have developed many sophisticated methods for solving Equation 2.4 based on the expansion of the wavefunction in Slater determinants. The simplest one is the Hartree-Fork (H-F) method (also called the self-consistent field method). However, the H-F method demands huge computational efforts, making it difficult to efficiently calculate large and complex systems. Moreover, the H-F method ignores correlation between electrons, leading to inaccurate results. DFT provides an appealing alternative by systematically mapping the many-body problem with $\hat{U}$ onto a single-body problem without $\hat{U}$.

2.2.2 Hohenberg-Kohn Theorems

DFT was first put on a firm theoretical footing by Hohenberg and Kohn in the framework of the two Hohenberg-Kohn (H-K) theorems in 1964 [19]. In DFT, the key variable is the electron density $n(\vec{r})$, expressed in terms of the normalized wavefunction Ψ as

$$n\left(\vec{r}\right) = N \int \mathrm{d}^3 r_2 \cdots \int \mathrm{d}^3 r_N \, \Psi^* \left(\vec{r}, \vec{r}_2, \ldots, \vec{r}_N\right) \Psi \left(\vec{r}, \vec{r}_2, \ldots, \vec{r}_N\right). \tag{2.5}$$

The first H-K theorem states that the ground-state properties of a many-electron system are uniquely determined by the ground-state electron density $n_0(\vec{r})$. This reduces the many-body problem of N electrons with $3N$ spatial coordinates to determining a function of only three spatial coordinates. The second H-K theorem defines a universal functional for the total energy $E[n]$ as

$$E[n] = T[n] + U[n] + \int V(\vec{r}) n(\vec{r}) \, \mathrm{d}^3 r. \tag{2.6}$$

The density which minimizes the energy yields the ground-state density n_0 and the minimum energy is the ground-state energy E_0.

Although the two H-K theorems prove the existence of a universal functional $E[n]$ without having to know the many-body wavefunction Ψ, they do not provide the form as to the nature of the functional, or how to actually calculate the ground-state density n_0.

2.2.3 Kohn-Sham Equations

The H-K theorems were further developed by Kohn and Sham in 1965 [20]. They expressed the total energy of an interacting system of N electrons as that of a fictitious auxiliary system of N non-interacting electrons at the same density. The total energy $E[n]$ is then given by

$$E[n] = T_s[n] + \int V(\vec{r})n(\vec{r})\mathrm{d}^3r + E_H[n] + E_{\mathrm{xc}}[n], \tag{2.7}$$

where T_s is the kinetic energy for non-interacting electrons, E_H is the Hartree energy, and E_{xc} is the exchange-correlation energy.

To minimize $E[n]$ in Equation 2.7, varying $n(\vec{r})$ with the constraint introduced by Lagrange multiplier gives

$$\left[-\frac{\hbar^2}{2m}\nabla^2 + V_s(\vec{r})\right]\psi_i = \epsilon_i\psi_i, \tag{2.8}$$

which yields the orbitals ψ_i that reproduce the density $n(\vec{r})$ of the original many-body system

$$n(\vec{r}) = n_s(\vec{r}) = \sum_i^N |\psi_i(\vec{r})|^2. \tag{2.9}$$

The effective single-particle potential V_s can be written in details as

$$V_s(\vec{r}) = V(\vec{r}) + \int \frac{e^2 n_s(\vec{r}')}{|\vec{r} - \vec{r}'|}\mathrm{d}^3r' + \frac{\delta E_{\mathrm{xc}}[n_s(\vec{r})]}{\delta n_s(\vec{r})}, \tag{2.10}$$

where the second term is the Hartree term describing the electron-electron Coulomb repulsion, and the third term is the exchange-correlation potential, which includes all quantum mechanical interaction effects beyond the classical Hartree terms.

Equation 2.8, Equation 2.9 and Equation 2.10 are called the Kohn-Sham (K-S) equations. The K-S equations need to be solved self-consistently due to the dependence of $V_s(\vec{r})$ on $n(\vec{r})$.

2.2.4 Exchange-Correlation Functionals

The major problem with DFT is that the exact exchange-correlation energy E_{xc} is unknown except for free electron gas. Approximations that permit the accurate calculation of certain physical properties are necessary to proceed further. In physics, the most widely used approximation is the local-density approximation (LDA), which assumes the E_{xc} only depends on the value of electron density at each point in space

$$E_{\mathrm{xc}}^{\mathrm{LDA}}[n] = \int n(\vec{r})\epsilon_{\mathrm{xc}}[n]\mathrm{d}^3r, \tag{2.11}$$

where $\epsilon_{\mathrm{xc}}[n]$ is the exchange-correlation energy per particle of uniform electron gas of density $n(\vec{r})$, which can be derived from homogeneous electron gas model.

LDA has a tendency to underestimate the exchange energy and over-estimate the correlation energy since the exchange and correlation parts tend to compensate each other to a certain degree [21]. In order to correct this error, it is common to expand the E_{xc} in terms of the gradient of the density to account for the non-homogeneity of the true electron density. This correction is referred to as generalized gradient approximation (GGA), which yields

$$E_{\mathrm{xc}}^{\mathrm{GGA}}[n, \vec{\nabla} n] = \int n(\vec{r}) \epsilon_{\mathrm{xc}}[n] F_{\mathrm{xc}}[n, \vec{\nabla} n] \mathrm{d}^3 r, \tag{2.12}$$

where F_{xc} is the enhancement factor.

There are various methods used to introduce the electron density gradient corrections. Perdew-Wang-91 (PW91) is a well-established method, proposed by Perdew and Wang in 1991 [22], to describe the GGA exchange-correlation functional, which is purely first-principles and fulfills almost all scaling relations except high density limit of uniform scaling. Perdew-Burke-Ernzerhof (PBE) [23] is a simplified and improved PW91 method that best fulfills many of the physical and mathematical requirements of DFT.

2.2.5 Hubbard U Correction

One of the well-known problems for first-principles DFT calculations within the LDA or GGA is the underestimation of band gaps of many transition-metal oxides [24; 25]. This error arises from the strongly correlated d or f electrons that can not be correctly described by LDA and GGA. DFT+U method provides a simple means to treat the strong on-site Coulomb interaction of localized electrons with an additional Hubbard-like term [26]. The strength of the on-site interactions is usually described by parameters U (on-site Coulomb) and J (on-site exchange). These parameters U and J can be extracted from first-principles calculations, but usually are obtained semi-empirically [27].

There are two main branches for DFT+U corrections. One is introduced by Lienchtenstein *et al.* [28], where U and J are used as independent corrections in the calculations. The other one is proposed by Dudarev *et al.* [29], in which only a single effective $U_{\mathrm{eff}} = U - J$ parameter

accounts for the Coulomb interaction, neglecting thereby any higher multi-polar terms. The DFT+U total energy for the latter approach is

$$E_{\mathrm{DFT+U}} = E_{\mathrm{DFT}} + \sum_{\sigma} \frac{U_{\mathrm{eff}}}{2}[\mathrm{Tr}\rho^{\sigma} - \mathrm{Tr}(\rho^{\sigma}\rho^{\sigma})], \tag{2.13}$$

where ρ^{σ} is the atomic orbital occupation matrix. This method can be understood as correcting the DFT total energy by adding a penalty functional that forces the on-site occupation matrix in the direction of idempotency, i.e. either fully occupied or fully unoccupied levels.

2.2.6 Vienna Ab initio Simulation Package

The DFT calculations performed in this work are implemented in the Vienna Ab initio Simulation Package (VASP) [30]. VASP is a computer software on Linux platform used for atomic-scale materials modeling, such as electronic structure calculations and quantum-mechanical molecular dynamics, from first principles. VASP computes an approximate solution to the many-body Schrödinger equation within DFT by solving the self-consistent K-S equations. Other methods such as the hybrid functionals that mix the H-F approach with DFT, Green's functions and many-body perturbation theory methods are also implemented in VASP [31].

In VASP, central quantities, such as the local potential, the one-electron orbitals, and the electronic charge density, are expressed in plane wave basis sets. The interactions between the electrons and ions are described using norm-conserving or ultrasoft pseudopotentials, or the projector-augmented-wave (PAW) method [31]. VASP basically uses four input files, including `INCAR` (input parameters), `POSCAR` (geometry data), `POTCAR` (pseudopotentials), and `KPOINTS` (k-point grid), for standard production runs. The output files normally include `OUTCAR` (de-

tailed summary of results), `OSZICAR` (brief summary of results), `CONTCAR` (optimized geometry), `DOSCAR` (density of states), `CHGCAR` (charges), and `WAVECAR` (wavefunction coefficients). These VASP calculations are usually performed in parallel mode on supercomputers or HPC clusters with multiple computing cores and nodes.

CHAPTER 3

OXIDE-SEMICONDUCTOR HETEROSTRUCTURES

(Section 3.1 and 3.2 were previously published as Hong, L., Bhatnagar, K., Droopad, R., Klie, R., Öğüt, S.: Atomic-scale structural and electronic properties of $SrTiO_3$/GaAs interfaces: A combined STEM-EELS and first-principles study. Physical Review B, 96:035311, 2017. Reuse license is shown in Appendix C. Section 3.3 was previously published as Hong, L., Huber, D., Contreras-Guerrero, R., Droopad, R., Klie, R.: *In-situ* STEM-EELS observation of ferroelectric switching of $BaTiO_3$ film on GaAs. Microscopy and Microanalysis, 23:1628, 2017. Reuse license is shown in Appendix D.)

3.1 Introduction

The properties of a hybrid thin film heterostructure are often dominated by the interface between the materials that comprise the structure. Extensive research has revealed key mechanisms and material properties that control an interface between chemically similar, isostructural materials. Integrating thin films with dramatically dissimilar chemical bonding, crystal symmetries and electronic structures, represents a promising new approach to engineer novel functional materials. For example, ultrathin strontium titanate ($SrTiO_3$) films grown on silicon (Si) or gallium arsenide (GaAs) that exhibit ferroelectric properties can facilitate the implementation of optical nonlinearities and carrier modulation at extremely high carrier densities. Successful

integration of $SrTiO_3$ thin film on Si substrate was first demonstrated by McKee *et al.* [32]. Compared to Si, compound semiconductors, such as GaAs, have much higher electron mobility, wider and direct band gap, making them promising for applications in electronics and photonics by directly coupling the polarization of a ferroelectric to the properties of a semiconductor. Perovskite oxide thin films, exhibiting enormous optical nonlinearities, can, therefore, serve as a key component for hybrid semiconductor-photonic systems. However, deposition of perovskite oxides directly with semiconductors is challenging, due to the structural difference and the potential oxidation of semiconductor surface [33]. Since the stability and performance of these heterojunctions are often governed by atomic-scale defects and interfaces between the two dissimilar materials, an understanding of the interfacial structural and electronic properties is critical.

The $SrTiO_3$/GaAs hetero-interfaces have been studied both theoretically and experimentally during the last decade [34; 35; 36; 37; 38; 39; 40; 41; 42; 43; 44; 45; 46]. $SrTiO_3$ thin film was epitaxially deposited on GaAs (001) without any amorphous interfacial layer using molecular beam epitaxy (MBE) method first by Liang *et al.* [34; 35]. A Ti prelayer was used to facilitate the growth of $SrTiO_3$ on GaAs substrate. Epitaxial $SrTiO_3$ thin film was found to be rotated by 45° with respect to GaAs so that the lattice mismatch between $SrTiO_3$ (a_{SrTiO_3} = 3.905 Å) and GaAs ($a_{GaAs}/\sqrt{2}$ = 3.997 Å) can be minimized to 2.3%. The $SrTiO_3$/GaAs interfaces were then characterized using STEM imaging at atomic-resolution by Klie *et al.* [36] It was reported that SrO-terminated $SrTiO_3$ film is epitaxially grown on As-terminated GaAs with atomically sharp interfaces. In addition, $SrTiO_3$ thin films deposited with and without Ti

prelayer on GaAs have structurally identical interfaces. A more detailed characterization of the atomic and electronic structures of the $SrTiO_3$/GaAs interfaces was carried out by Qiao *et al.* [37] using low-energy EELS along with first-principles calculations. By analyzing the O vacancies and Ti concentrations in the $SrTiO_3$ film and across the interface, it was suggested that without the presence of Ti prelayer, the interfacial As gets oxidized which results in the Fermi-level pinning, while in the presence of Ti prelayer, Ti diffuses into surface GaAs and alleviates the oxidation which unpins the Fermi level. From a computational perspective, there have been few first-principles total energy calculations performed using DFT to determine the stable structures of the $SrTiO_3$/GaAs interfaces. By comparing the formation energies of various interface configurations, the SrO/Ga heterostructure with Ga-O bonds was found to be the most favorable [43; 44; 45; 46], which is consistent with the recent X-ray photoemission spectroscopy characterization of the $SrTiO_3$/GaAs interface [40]. However, a more systematic and detailed study with a combination of experimental and theoretical investigations is needed to determine the structure of the $SrTiO_3$/GaAs interface. Since GaAs (001) was used experimentally as a substrate with fixed As-termination in the previous STEM-EELS studies, it was not possible to determine the energetic preference of Ga- or As-termination at the interface. This can be potentially solved by depositing GaAs films on $SrTiO_3$, which was achieved more than a decade ago by Droopad *et al.* [47; 48], but the atomic structure of this heterointerface has not yet been characterized. In addition, the effects of atomic-scale interfacial defects on the electronic properties of the heterostructure, including Fermi-level pinning and band alignment, need to

be studied to establish a better understanding of the structure-property relationship of the $SrTiO_3$/GaAs interface.

In Section 3.2, I will present results and analyses of a combined experimental and theoretical study of the $SrTiO_3$/GaAs heterointerfaces at atomic scale. Epitaxial GaAs is grown on Si substrate with a $SrTiO_3$ buffer layer using MBE method. The $SrTiO_3$/GaAs interface in my sample is characterized using atomic-resolution STEM imaging and EELS. (2×2) structural models with various interface compositions are constructed and optimized using first-principles DFT calculations. My results show that O-deficient SrO layer in contact with As layer is the most favorable interface structure and the experimentally observed interface structure is reproduced in the DFT simulation. Ga-termination is favored over As-termination at the interface under O-rich condition but the GaAs surface is easily oxidized by forming a Ga_2O_3 interlayer. The interface structure is determined by the accommodation of polar discontinuity which is related to the interface composition. Interfacial vacancies are found to play an important role in determining the electronic properties of the heterointerfaces.

Upon integration of the $SrTiO_3$/GaAs heterostructure, it can be used as a substrate to grow other functional oxides with similar lattice parameters, such as the ferroelectric barium titanate ($BaTiO_3$) [40], lead zirconate titanate ($PbZr_xTi_{1-x}O_3$) [46], ferromagnetic lanthanum strontium manganite ($La_{1-x}Sr_xMnO_3$) and multiferroic bismuth ferrite ($BiFeO_3$) [49], for the purpose of coupling multiple functionalities on a single platform. Epitaxial single-crystalline $BaTiO_3$ thin film with a thickness of 7.5 nm has been successfully grown on polar GaAs substrate with a 2-unit-cell $SrTiO_3$ interlayer using MBE method. A coercive voltage of $1-2$ V and piezoresponse

amplitude $\sim$ 5 pm/V were measured using the piezoresponse force microscopy [40]. The sample was then characterized using STEM-EELS and DFT methods. A spontaneous polarization in the $BaTiO_3$ thin film was measured directly from HAADF and ABF imaging, and the pinned polarization was attributed to the O vacancies present at the $SrTiO_3$/GaAs interface [50]. In Section 3.3, I will present results and analyses of the ferroelectric switching behavior in $BaTiO_3$ thin film using *in-situ* STEM-EELS imaging. The sample is successfully assembled into a dedicated electrical chip for *in-situ* TEM characterization. The switched displacement of Ti atomic columns in the $BaTiO_3$ unit cell is directly observed from the atomic-resolution HAADF images under different external electrical biases, and the structural change is confirmed by energy shift in the O K-edge ELNES.

3.2 $SrTiO_3$/GaAs Heterointerfaces

3.2.1 Experimental Setup

The $SrTiO_3$/GaAs heterostructure sample is grown using the MBE method. A 10-nm-thick SrO-terminated $SrTiO_3$ thin film is grown on Si (001) wafer with a 4° miscut in the [110] direction. During the growth, oxygen diffuses through the perovskite $SrTiO_3$ layer and reacts with the interfacial Si atoms forming a SiO_2 interlayer. The surface termination of the $SrTiO_3$ film can be chosen after the growth layer growth by monitoring the reflection high-energy electron diffraction reconstruction and opening the relevant shutters. By default, the $SrTiO_3$ growth is performed under a stoichiometric regime that can be switched to either a Ti-rich or Sr-rich surface by closing the shutter for the respective metal cell and keeping the other one open until specific termination is achieved [51]. The SrO-termination of $SrTiO_3$ film is achieved

by closing the shutter of Ti effusion cell while keeping that of Sr effusion cell open in the oxide MBE chamber. The wafer is then transferred into a second MBE chamber for the growth of III-V semiconductor layer. Simultaneous Ga and As_2 are exposed to the $SrTiO_3$ surface to form a 1-μm-thick epitaxial GaAs layer.

Two cross-section TEM samples are polished in two directions that are 90° rotated with respect to each other using standard wedge polishing methods and then thinned down to electron transparency (< 50 nm) using low-energy ($0.5-3$ kV) and low-angle ($6°-10°$) argon ion milling on a liquid-nitrogen-cooled stage to minimize the ion beam damage.

The STEM-HAADF images are acquired at 200 kV with a convergence semi-angle of 29 mrad and a collection angle from 90 to 170 mrad. The atomic-resolution HAADF images are recorded at magnification of 2×10^7 (pixel size of 0.02 nm) and pixel dwell time of 31 μs. For EELS at 200 kV, a convergence angle of 30 mrad and a collection angle with 35 mrad are used. Energy dispersions of 0.1 eV/channel and 0.3 eV/channel are used for the measurement of Ti $L_{3,2}$-edge and O K-edge, respectively. The atomic-resolution EELS line scan is recorded using pixel size of 0.06 nm and pixel dwell time of $0.5 - 0.7$ s. The exponential EEL spectrum background is subtracted from each spectrum and the resulting data are normalized with respect to the post edge intensity. No obvious beam damage to the sample is observed during both imaging and EELS collection at 200 kV.

3.2.2 Computational Setup

First-principles DFT calculations are carried out using the PAW method [52], as implemented in VASP, and the exchange-correlation functional of PBE [23]. Plane wave energy

cutoff is set as 400 eV. Periodic slabs with (2×2) surface cell, as shown in Figure 3.2.1, are constructed to simulate the $SrTiO_3$/GaAs interfaces. The slabs are fully optimized with a maximum force criterion of 10^{-2} eV/Å. $4 \times 4 \times 1$ and $12 \times 12 \times 1$ Monkhorst-Pack k-point grids are used during structural optimization and density of states (DOS) calculations, respectively.

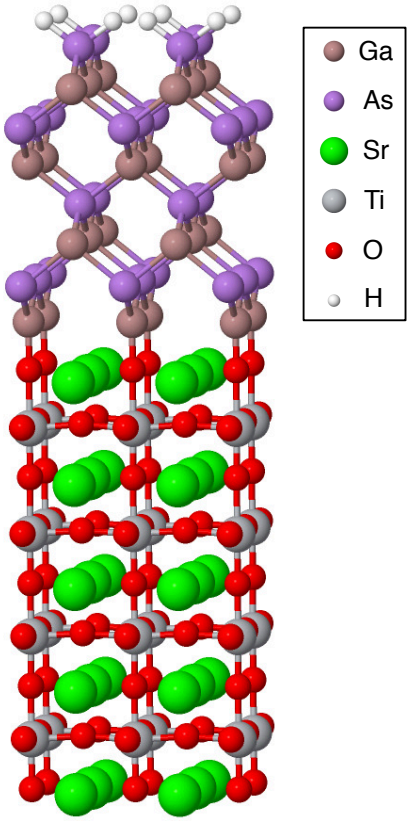

Figure 3.2.1. Ball-and-stick model of the (2×2) $SrTiO_3$/GaAs interfaces in three-dimensional view. The top surface of GaAs is passivated by pseudo-hydrogen atoms and the bottom surface of $SrTiO_3$ is in contact with vacuum.

The computed lattice parameters of bulk $SrTiO_3$ and GaAs are found to be 3.94 Å and 5.76 Å, respectively. To mimic GaAs growth on $SrTiO_3$ substrate, I use the in-plane lattice parameter of $a_{GaAs} = 5.57$ Å $(= \sqrt{2}a_{SrTiO_3})$ for GaAs, with a 45° in-plane rotation, to match the lattice parameter of $SrTiO_3$. The top surface of GaAs is As layer and is passivated with pseudo-hydrogens to saturate the As dangling bonds [53]. The bottom surface of $SrTiO_3$ is SrO layer in contact with an out-of-plane vacuum of 8 Å to separate the slabs. The electronic and structural properties of the slabs are well converged with respect to both the k-point sampling and the length of vacuum. Various interface structures, including SrO- or TiO_2-terminated $SrTiO_3$ and bare Sr- or Ti-terminated $SrTiO_3$ in contact with Ga- or As-terminated GaAs, are constructed to investigate the $SrTiO_3$/GaAs interfacial registry. I use the notation SrO/Ga (Sr/Ga) to denote the interface of fully oxygenated (O-deficient) SrO-terminated $SrTiO_3$ in contact with Ga-terminated GaAs. Considering all the terminations, I have 8 different interfacial configurations, which are SrO/Ga, TiO_2/Ga, SrO/As, TiO_2/As, Sr/Ga, Ti/Ga, Sr/As and Ti/As.

The formation energy for a given interfacial configuration is defined as [54]

$$E_{\text{interface}} = E_{\text{slab}} - n_{\text{Sr}}\mu_{\text{Sr}} - n_{\text{Ti}}\mu_{\text{Ti}} - n_{\text{O}}\mu_{\text{O}} - n_{\text{Ga}}\mu_{\text{Ga}} - n_{\text{As}}\mu_{\text{As}}, \tag{3.1}$$

where E_{slab} is the total energy of the corresponding slab, n_i (i = Sr, Ti, O, Ga and As) is the number of atoms or units of type i in the slab, and μ_i is the corresponding chemical potential.

The chemical potentials in the Equation 3.1 are constrained by those of bulk $SrTiO_3$ and GaAs, i.e.

$$\mu_{\mathrm{Sr}} + \mu_{\mathrm{Ti}} + 3\mu_{\mathrm{O}} = \mu^{\mathrm{bulk}}_{\mathrm{SrTiO_3}}, \tag{3.2}$$

$$\mu_{\mathrm{Ga}} + \mu_{\mathrm{As}} = \mu^{\mathrm{bulk}}_{\mathrm{GaAs}}. \tag{3.3}$$

According to these constraints, I can use three independent variables, which are μ_{Ti}, μ_{O} and μ_{As}, to calculate the formation energy in Equation 3.1. For simulation of GaAs grown on $SrTiO_3$, $\mu^{\mathrm{bulk}}_{\mathrm{GaAs}}$ is the DFT total energy of bulk GaAs strained in the x-y plane to the $SrTiO_3$ lattice constant and relaxed in the z direction, while $\mu^{\mathrm{bulk}}_{\mathrm{SrTiO_3}}$ is the DFT total energy of cubic bulk $SrTiO_3$.

There are additional constraints to prevent formation of other materials during growth. I use three bulk compounds, which are TiO_2, Ti_2O_3 and the Ruddlesden-Popper structure $Sr_6Ti_5O_{16}$, to set bounds on the allowed chemical potential ranges as described by Hellberg *et al.* who studied $SrTiO_3$/Si interfaces [55]. The chemical potentials of Sr, Ti, Ga, As and O are constrained by the DFT total energy of bulk Sr (fcc), Ti (hcp), Ga (orthorhombic), As (A7) and isolated O_2 molecule. These constraints yield the following inequalities:

$$\mu_{\mathrm{Sr}} < \mu^{\mathrm{bulk}}_{\mathrm{Sr}}, \tag{3.4}$$

$$\mu_{\mathrm{Ti}} < \mu^{\mathrm{bulk}}_{\mathrm{Ti}}, \tag{3.5}$$

$$\mu_{\mathrm{O}} < \frac{1}{2}\mu^{\mathrm{molecule}}_{\mathrm{O_2}}, \tag{3.6}$$

$$\mu_{\mathrm{Ga}} < \mu_{\mathrm{Ga}}^{\mathrm{bulk}}, \tag{3.7}$$

$$\mu_{\mathrm{As}} < \mu_{\mathrm{As}}^{\mathrm{bulk}}, \tag{3.8}$$

$$\mu_{\mathrm{Ti}} + 2\mu_{\mathrm{O}} < \mu_{\mathrm{TiO_2}}^{\mathrm{bulk}}, \tag{3.9}$$

$$2\mu_{\mathrm{Ti}} + 3\mu_{\mathrm{O}} < \mu_{\mathrm{Ti_2O_3}}^{\mathrm{bulk}}, \tag{3.10}$$

$$6\mu_{\mathrm{Sr}} + 5\mu_{\mathrm{Ti}} + 16\mu_{\mathrm{O}} < \mu_{\mathrm{Sr_6Ti_5O_{16}}}^{\mathrm{bulk}}. \tag{3.11}$$

In order to obtain atomically abrupt $SrTiO_3$/GaAs heterostructure, additional constraints are imposed which requires that neither Ga or As oxides [56] nor any Sr or Ti arsenides [42] are present at the interface. Among these constraints, Ga_2O_3 which yields the inequality of

$$2\mu_{\mathrm{Ga}} + 3\mu_{\mathrm{O}} < \mu_{\mathrm{Ga_2O_3}}^{\mathrm{bulk}}, \tag{3.12}$$

where $\mu_{\mathrm{Ga_2O_3}}^{\mathrm{bulk}}$ is approximated by the DFT total energy of β-Ga_2O_3, turns out to be the most important in this system [57; 43].

3.2.3 STEM-EELS Characterization of the Interface

The atomic-resolution HAADF images of my sample taken from cross-sections in two directions that are rotated 90° with respect to each other are displayed in Figure 3.2.2. Figure 3.2.2(a), with $SrTiO_3$ [010]||GaAs [110] epitaxy, shows full GaAs dumbbell structure at the interface, while Figure 3.2.2(c), with $SrTiO_3$ [100]||GaAs [1$\bar{1}$0] epitaxy, shows half GaAs dumbbell structure at the interface. Both images exhibit a sharp interface between $SrTiO_3$ and GaAs

in 1× periodicity without any surface reconstruction or amorphous interlayer. The elements can be characterized by the intensity contrast of each atomic column in the HAADF images since the HAADF intensity is directly correlated to the atomic number. From the intensity line profiles shown in Figure 3.2.2(b) and (d), I can clearly see that $SrTiO_3$ films are terminated by SrO layer while GaAs is terminated by As. The interfacial As atoms are located above the oxygen sites in the SrO, and the GaAs dumbbells are in excellent epitaxy with respect to SrO or TiO_2 columns in the out-of-plane direction.

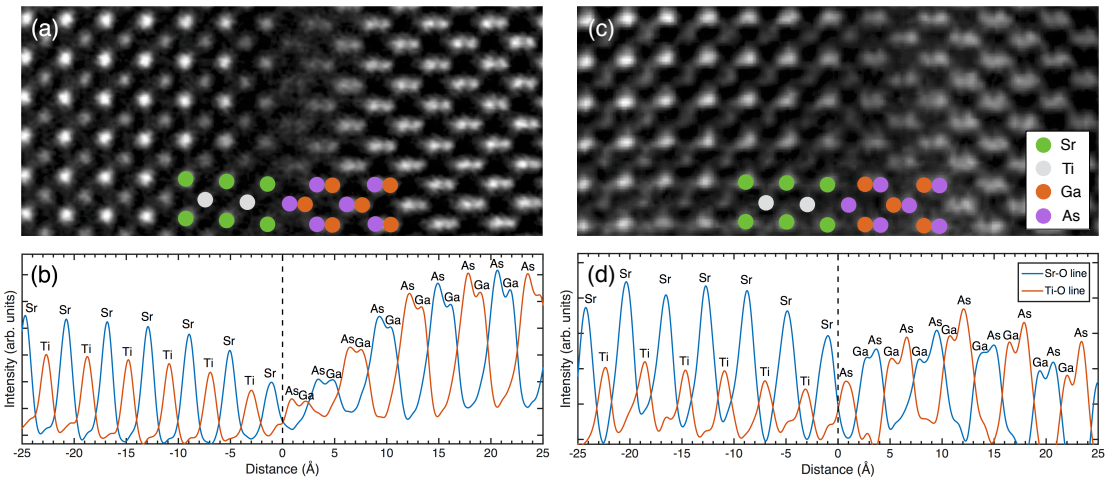

Figure 3.2.2. Atomic-resolution HAADF images of the $SrTiO_3$/GaAs interface from two different views which are 90° rotated: (a) the $SrTiO_3$ [010]||GaAs [110] epitaxy with full GaAs dumbbell structure at the interface and (c) the $SrTiO_3$ [100]||GaAs [1$\bar{1}$0] epitaxy with half GaAs dumbbell structure at the interface. The images are taken from dislocation-free areas and filtered using Average Background Subtraction filter within Gatan Digital Micrograph^{TM}. (b) and (d) show the intensity profiles of atomic lines centered on the Sr and Ti in $SrTiO_3$ averaged from (a) and (c), respectively.

For Ti oxides, it is known that the ELNES of Ti $L_{3,2}$-edge can reflect the valence state, coordination and site geometry of Ti [58], providing fundamental information on cation ordering and defect clustering such as O vacancies [59]. Therefore, atomic-resolution EEL spectra of Ti $L_{3,2}$-edge are taken from the first four TiO_2 layers at the $SrTiO_3$/GaAs interface and compared with that in bulk $SrTiO_3$ to examine the near-interface Ti valence and O concentration. As shown in Figure 3.2.3(a), the Ti $L_{3,2}$-edge of the second to fourth TiO_2 layers exhibit four prominent peaks originating from the splitting of $3d^0$ states into t_{2g} and e_g components, which corresponds to a Ti^{4+} valence. In the first TiO_2 layer, the intensity of the t_{2g} peaks significantly decreases and the positions of e_g peaks shift to lower energies, which indicates a decrease of Ti valence from 4+ to a mixture of 3+ and 4+ [59; 60]. The decrease of Ti valence near the interface can be attributed to the interfacial O vacancies. Moreover, the t_{2g}-e_g splitting in both the L_3- and L_2-edges reduces near the interface compared to the bulk spectrum, as a result of the increased TiO_6 octahedral distortion due to O vacancies and the ferroelectric polarization induced by the polar GaAs (001) surface.

To further confirm the interfacial O vacancies, atomic-resolution EEL spectra of O K-edge are taken from the first four SrO layers at the $SrTiO_3$/GaAs interface. In Figure 3.2.3(b), it is clearly noticeable that the ELNES of O K-edge fades in the first SrO layer, due to the destruction of long-range order in the O sublattice and the presence of interfacial O vacancies [61]. The three featured peaks (labeled as a, b and c) for $SrTiO_3$ bulk are all observed in the second to fourth SrO layers; however, the intensity of peak a, which is assigned to the

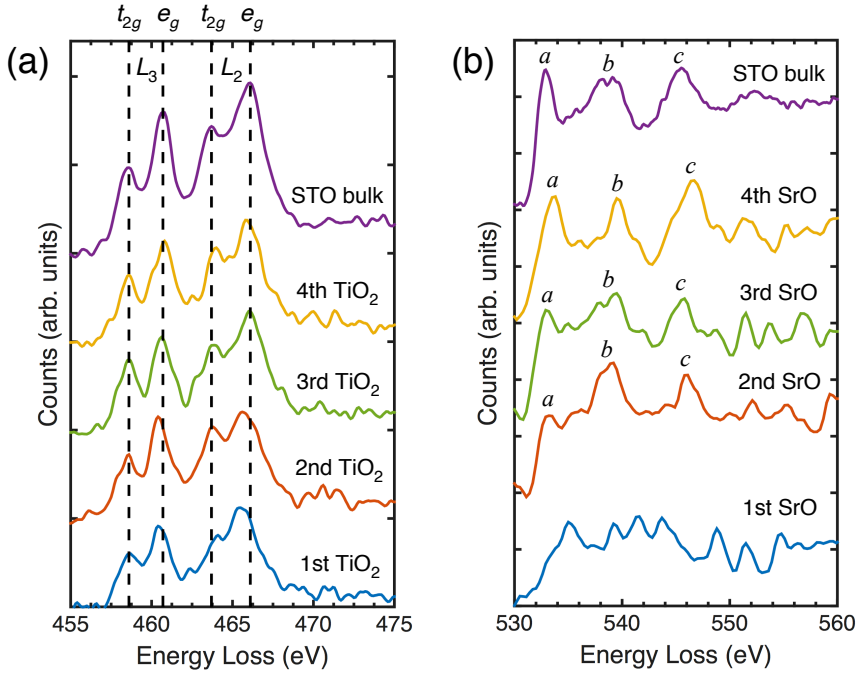

Figure 3.2.3. (a) ELNES of Ti $L_{3,2}$-edge taken from $SrTiO_3$ bulk and the first to fourth TiO_2 layer near the $SrTiO_3$/GaAs interface. The dashed lines denote the positions of the four peaks in the bulk spectrum. (b) ELNES of O K-edge taken from $SrTiO_3$ bulk and the first to fourth SrO layer near the $SrTiO_3$/GaAs interface. The spectrum data are smoothed using Gaussian function.

hybridization of O $2p$ with Ti $3d$-t_{2g}, decreases from fourth to second SrO layer, suggesting that Ti t_{2g} orbital is partially occupied near the interface.

In summary, when GaAs is deposited on $SrTiO_3$, As atoms are favored to be in contact with an O-deficient SrO surface to form an atomically abrupt $SrTiO_3$/GaAs interface without surface reconstruction. The observed interface structure is consistent with the HAADF images of $SrTiO_3$ thin film grown on GaAs substrate in the previous studies [36; 37; 50]. Therefore,

the experimentally favorable configuration of $SrTiO_3$/GaAs heterointerfaces is O-deficient SrO layer in contact with As layer and this configuration is independent of which one is the substrate material.

3.2.4 Stability of the Interface Structures

First-principles DFT calculations are carried out to further explore the structural and electronic properties of the $SrTiO_3$/GaAs interfaces observed in the experiment. All the proposed interface structures are fully relaxed in the geometry optimization. As a result, some of the initial structures with different interfacial configurations turn into the same structure. In the following discussion, I only focus on the most stable geometry for each interfacial composition.

The formation energies of interface structures with different compositions are compared by the ternary phase diagrams shown in Figure 3.2.4. The phase diagrams exhibit similar landscapes for Ga-rich and As-rich conditions. The SrO/Ga and Sr/As interfaces (the blue and red areas in the phase diagram) turn out to be the most stable structures under O-rich and O-poor conditions, respectively. The results show that SrO layer either with or without O vacancies is favored over TiO_2 layer at the $SrTiO_3$/GaAs interface, which is consistent with the previous experimental findings that no Ti is observed at the interface even though a Ti thin layer was pre-deposited between the GaAs and $SrTiO_3$ during the MBE growth in earlier studies [36; 37]. The phase diagram illustrates a critical value of the oxygen chemical potential, $\mu_O = -4.67$ eV (Ga-rich) and $\mu_O = -4.05$ eV (As-rich), for the switching of the preferred interfacial layer from As to Ga. I also examine the formation energies using the lattice parameter of bulk GaAs ($a_{GaAs} = 5.76$ Å) for the slabs to mimic the situation of $SrTiO_3$ grown on GaAs

substrate. The phase diagrams are found to be independent of the deposition sequence (i.e. GaAs on $SrTiO_3$ or $SrTiO_3$ on GaAs).

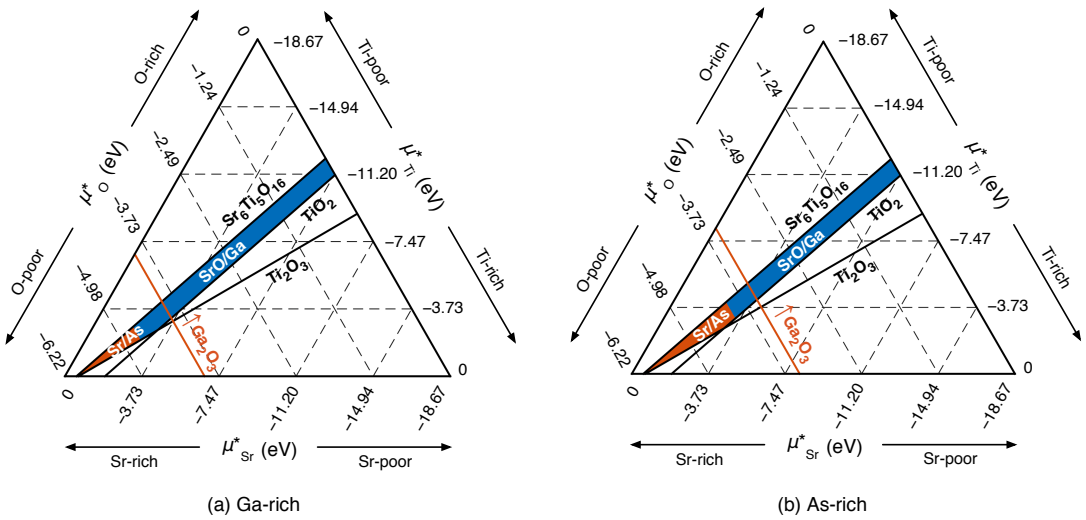

Figure 3.2.4. The computed ternary phase diagram of the formation energies of $SrTiO_3$/GaAs interfaces with different stoichiometries under (a) Ga-rich ($\mu_{Ga} = \mu^{bulk}_{Ga}$) and (b) As-rich ($\mu_{As} = \mu^{bulk}_{As}$) conditions. The three axes are calculated as $\mu^*_{Sr} = \mu_{Sr} - \mu^{bulk}_{Sr}$, $\mu^*_{Ti} = \mu_{Ti} - \mu^{bulk}_{Ti}$ and $\mu^*_O = \mu_O - \frac{1}{2}\mu^{molecule}_{O_2}$, where μ^{bulk}_{Sr}, μ^{bulk}_{Ti} and $\mu^{molecule}_{O_2}$ are approximated by their DFT total energies. The allowed chemical potential area of stable $SrTiO_3$ without formation of other bulk materials is bounded by the solid lines corresponding to the constraints of TiO_2, Ti_2O_3 and Ruddlesden-Popper structure $Sr_6Ti_5O_{16}$. The region to the right of the red line denotes the formation of Ga_2O_3.

Considering the oxygen flux used in the deposition of $SrTiO_3$, the GaAs (001) can be easily oxidized by formation of Ga_2O_3 on the surface [57; 43]. The maximal chemical potential of oxygen for an interface without forming Ga_2O_3 is calculated as $\mu^{max}_O = -3.94$ eV (Ga-rich) and

$\mu_O^{max} = -3.51$ eV (As-rich). Imposing the chemical potential constraint to avoid precipitation of Ga_2O_3, the allowed region where GaAs can be epitaxially deposited on $SrTiO_3$ is restricted into a small area in the O-poor and Sr-rich corner of the phase diagram, which is dominated by Sr/As interface. According to the calculated phase diagram, no thermodynamically stable and atomically abrupt $SrTiO_3$/GaAs heterointerface can be obtained in the O-rich condition. Considering the normal MBE growth condition for oxygen which is 300°C to 500°C at 10^{-8} mbar, the allowed O chemical potential is limited to the range of -1.20 eV to -1.78 eV (calculated using the method in Ref. [62]), which is within the range of Ga_2O_3 formation discussed above. Therefore, when $SrTiO_3$ is directly deposited on GaAs substrate with oxygen flux, there should, at equilibrium, always be a layer of Ga_2O_3 forming prior to the $SrTiO_3$. In order to obtain an abrupt interface, the oxygen flux should be turned off during the growth of the interface. This kinetic inhibition of Ga_2O_3 is similar to that of SiO_2 in the $SrTiO_3$/Si interfaces [63]. On the other hand, when depositing GaAs on $SrTiO_3$, oxygen is mainly provided by the $SrTiO_3$ substrate; thus, the first GaAs layer is determined by the O concentration at the $SrTiO_3$ surface.

3.2.5 Atomic and Electronic Structures of the Interfaces

In the following discussion, I mainly focus on the two energetically favorable interface structures, which are SrO/Ga and Sr/As. Figure 3.2.5 shows the relaxed structures of the two interfaces, which exhibit different patterns. In the SrO/Ga interface structure, I find a $c(2 \times 2)$ interface reconstruction of Ga atoms by forming Ga dimers and Ga-O bonds as shown in Figure 3.2.5(a) and (b). The stability of the $c(2 \times 2)$ reconstruction has been confirmed by testing larger unit cells such as (2×4) and (4×2), known as the favorable size of GaAs surface recon-

struction [64]. In the Sr/As interface structure, there is no surface reconstruction, where the (1×1) surface unit cell is preserved, and interfacial As atoms sit on the top of the Sr hollow sites (O vacancies) as shown in Figure 3.2.5(c) and (d).

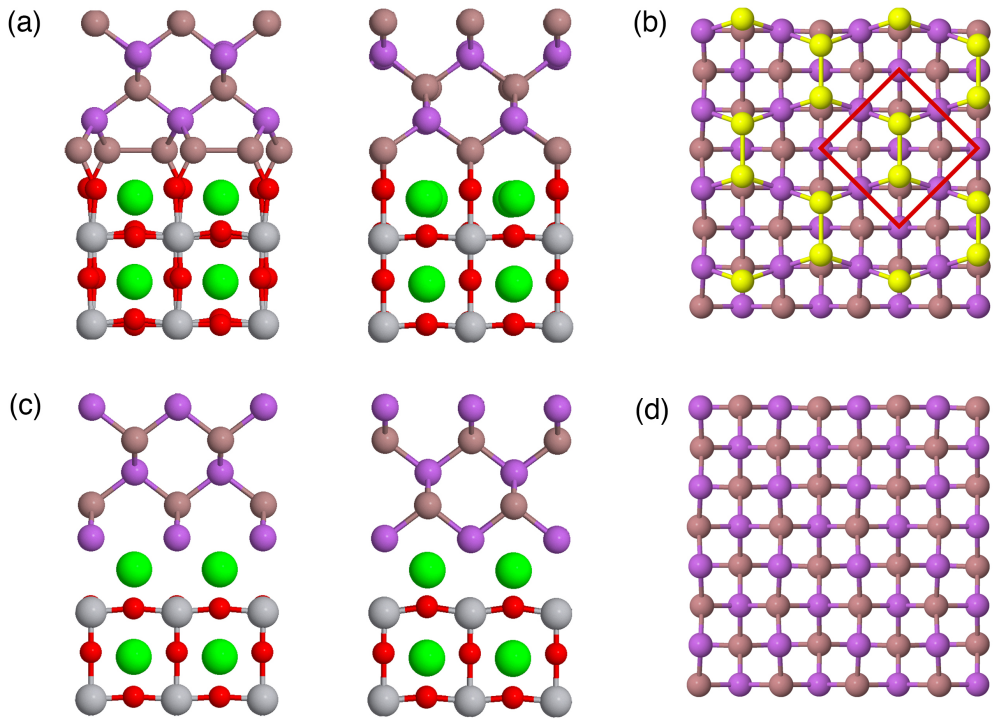

Figure 3.2.5. The DFT-optimized structures of SrO/Ga and Sr/As interfaces. (a) The (2×2) SrO/Ga interface viewed in $SrTiO_3$ [010]||GaAs [110] and $SrTiO_3$ [100]||GaAs [1$\bar{1}$0] directions. (b) A (4×4) view of the reconstructed GaAs (001) surface at the SrO/Ga interface with the top Ga atoms highlighted. The unit cell of $c(2 \times 2)$ reconstruction is marked by red square. (c) The (2×2) Sr/As interface viewed in $SrTiO_3$ [010]||GaAs [110] and $SrTiO_3$ [100]||GaAs [1$\bar{1}$0] directions. (d) A (4×4) view of the unreconstructed GaAs (001) surface at the Sr/As interface.

The $SrTiO_3$/GaAs heterostructure can be divided into alternating (001) planes of SrO, TiO_2, Ga and As. SrO and TiO_2 layers are charge neutral while Ga and As layers take on $+3$ and -3 charges, respectively. Therefore, the $SrTiO_3$/GaAs interface has a polar discontinuity, which has to be compensated. For Ga-termination, each Ga atom has $1.5e^-$ in its dangling bonds at the interface, while for SrO-termination, each Sr atom can provide $2e^-$ for each O to fill the O $2p$ orbital. Thus, in the reconstructed $c(2 \times 2)$ SrO/Ga interface cell (with 2 atoms of each species in the surface unit cell), the electropositive elements (Ga and Sr) can provide a total of $7e^-$ while the electronegative element (O) only needs $4e^-$. Since Sr is not able to change its valence state, the interface must reconstruct to accommodate the polar discontinuity. The GaAs surface is then reconstructed by forming a Ga-Ga dimer which consumes $2e^-$ and leaves $1e^-$ (i.e. $0.5e^-$ per (1×1) unit cell). For As-termination, each As atom needs $1.5e^-$ to saturate its dangling bonds, which can be provided by the Sr atom in the Sr layer. The remaining $0.5e^-$ of Sr atom transfers to Ti atom in the TiO_2 layer underneath, lowering the valence of Ti from 4+ to 3.5+. The polar discontinuity is then accommodated by the creation of electrical dipole in the first $SrTiO_3$ unit cell. Thus, the Sr/As interface structure is abrupt without GaAs reconstruction, which is in good agreement with the interface observed in my STEM images, and the microscopic explanation of interfacial charge distribution can be also confirmed by the EEL spectra. The reconstruction of GaAs is found in other interface structures which are not presented in the phase diagram, such as the Sr/Ga and SrO/As interfaces.

The projected DOS on each element in each $SrTiO_3$ and GaAs unit cell are plotted for the SrO/Ga and Sr/As interfaces as shown in Figure 3.2.6. Both interfaces are metallic with

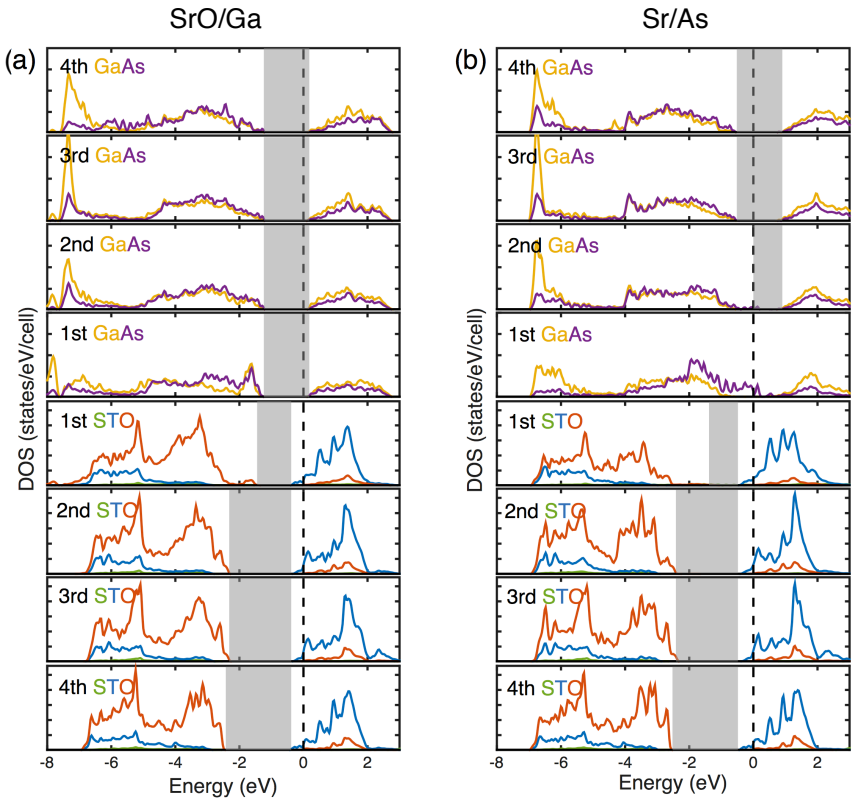

Figure 3.2.6. Projected DOS on each element from the first to fourth $SrTiO_3$ and GaAs unit cells for (a) SrO/Ga interface and (b) Sr/As interface. The yellow, purple, green, blue and red curves represent DOS on Ga, As, Sr, Ti and O, respectively. Fermi level is shifted to zero and the energy gaps near Fermi level are marked by the shaded areas.

the Fermi level pinned to the conduction band minimum (CBM) of $SrTiO_3$ and the states at Fermi level are mainly contributed by Ti $3d$ states. In order to verify that the observed Fermi level pinning is not an artifact of the DFT band-gap underestimation [65], I perform PBE+U method with the effective Hubbard correction ($U = 2.0,\ 4.0,\ 6.0$ and 8.0 eV) to Ti $3d$ states.

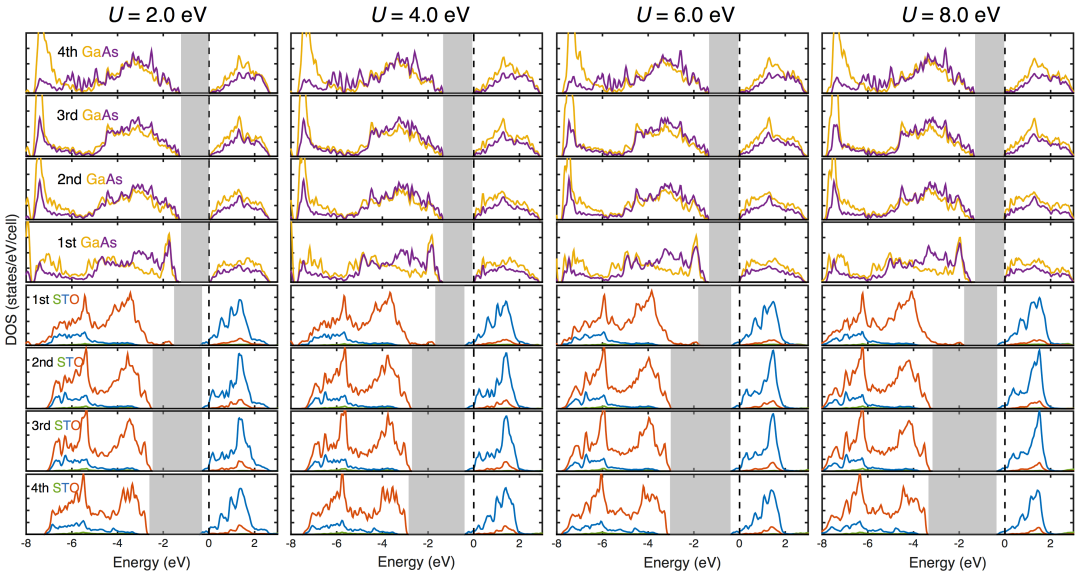

Figure 3.2.7. Projected DOS on each element from the first to fourth $SrTiO_3$ and GaAs unit cells for SrO/Ga interface calculated using PBE+U method with effective Hubbard correction ($U = 2.0,\ 4.0,\ 6.0$ and 8.0 eV) to Ti 3d states. Fermi level is shifted to zero and the energy gaps near Fermi level are marked by the shaded areas.

Figure 3.2.5 shows that even though the band gap of $SrTiO_3$ increases as U increases, the Fermi level remains pinned to the CBM of $SrTiO_3$ with occupied Ti $3d$ states. Therefore, the Fermi level pinning is physically meaningful in my calculations. The localized metallic Ti $3d$ states at the CBM of $SrTiO_3$ are also found in interfaces without O vacancies, indicating that O vacancies are not the main source of these electrons. They can be attributed to the formation of two-dimensional electron gas (2DEG), which has been extensively demonstrated in the $SrTiO_3$-based complex oxide hetero-interfaces and vacuum-cleaved $SrTiO_3$ surface [66; 67; 68; 69; 70; 71; 72; 73; 74]. To further explore the 2DEG at the $SrTiO_3$/GaAs interfaces, the charge density of the 2DEG is calculated by integrating the DOS of the Ti occupied states, and plotted as a function of TiO_2 layers as shown in Figure 3.2.8. I can see that the occupied states in the CBM of $SrTiO_3$ exhibit a strong 2D character consisting mostly of Ti d_{xy} states. As explained before, both the SrO/Ga and Sr/As interfaces have extra $0.5e^-$ per (1×1) unit cell which corresponds to a charge density of $\sim 3.0 \times 10^{14}$ cm^{-2}, donated from the electropositive elements and transfered to the unoccupied Ti $3d$ orbitals in the first TiO_2 layer; however, the computed charge density at the interface is much lower than that value since the 2DEG can spread over several layers into the bulk region [68]. It is noteworthy that Sr/As structure has a higher charge density than the SrO/Ga structure in the first TiO_2 layer, suggesting that O vacancies are able to enhance the 2DEG at the interface. Moreover, I find that the first and last TiO_2 layers have higher charge density than the middle layers, indicating the formation of 2DEG at both $SrTiO_3$/GaAs interface and vacuum/$SrTiO_3$ surface.

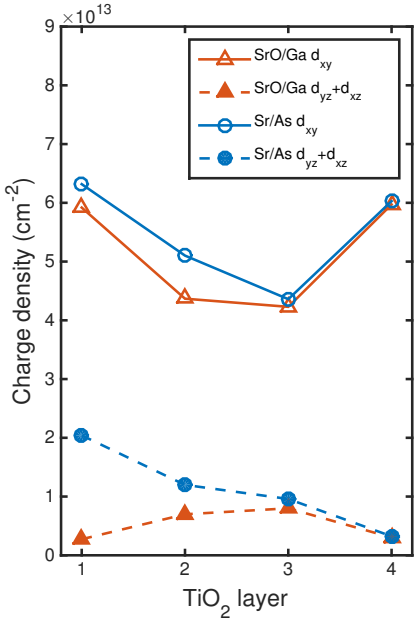

Figure 3.2.8. Charge density of Ti d_{xy} and $d_{yz} + d_{xz}$ occupied states at the CBM of $SrTiO_3$ as a function the distance of TiO_2 layers from the interface.

In addition, band alignment across the SrO/Ga and Sr/As interfaces is examined with results illustrated in Figure 3.2.9, in order to obtain the macroscopic electronic properties of the hetero-sturctures. For the SrO/Ga interface, the conduction and valence band offsets are calculated as $\Delta E_c = -0.15$ eV and $\Delta E_v = 1.68$ eV, corresponding to a type I heterostructure. For the Sr/As interface, the conduction and valence band offsets are obtained as $\Delta E_c = 0.57$ eV and $\Delta E_v = 2.40$ eV, corresponding to a type II heterostructure, which is in excellent agreement with the experimental values (0.6 ± 0.1 eV and 2.5 ± 0.1 eV) [35]. The difference of band offsets

between the two structures is due to the higher electrostatic potential of GaAs with respect to $SrTiO_3$ in Sr/As interface than that in SrO/Ga interface, as can be seen in Figure 3.2.9.

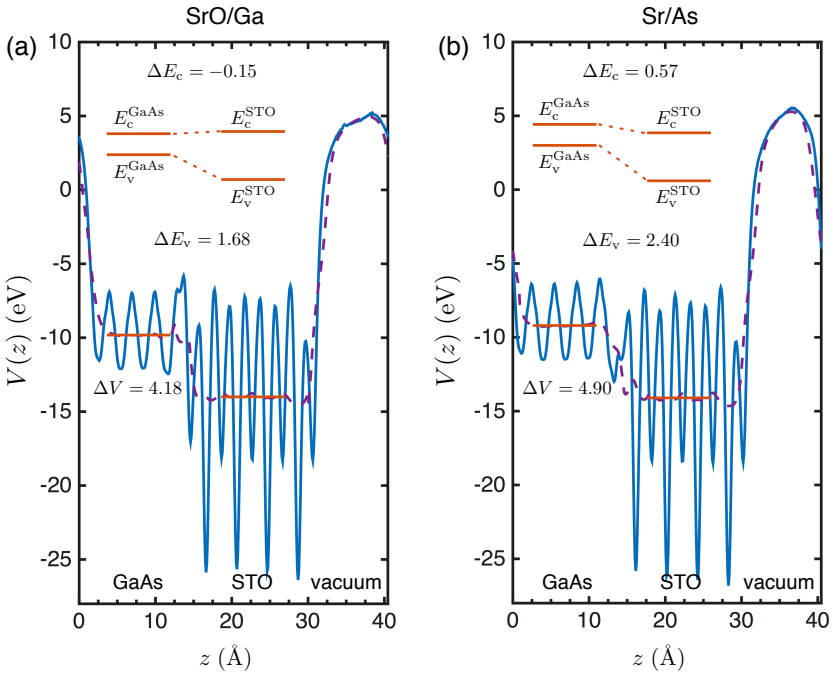

Figure 3.2.9. Band alignment diagrams of $SrTiO_3$/GaAs hetero-structures for (a) SrO/Ga interface and (b) Sr/As interface. The blue solid curve represents the profile of electrostatic potential of the hetero-structure along out-of-plane direction $V(z)$, and the purple dashed curve represents the macroscopic average of the electrostatic potential. The red lines indicate the averaged values of the potential in bulk-like regions and the band alignment results. The conduction and valence band offsets are determined as $\Delta E_c = E_c^{\mathrm{GaAs}} - E_c^{\mathrm{SrTiO_3}}$ and $\Delta E_v = E_v^{\mathrm{GaAs}} - E_v^{\mathrm{SrTiO_3}}$. ΔV stands for the difference of the averaged potential between GaAs and $SrTiO_3$ parts.

3.2.6 Vacancies at the Interfaces

From the previous discussion, I know that O vacancies play an important role in determining the structural properties of the $SrTiO_3$/GaAs interfaces. In this section, I consider two types of interfacial defects, which are O vacancies in the first SrO layer and Ga/As vacancies in the first Ga/As layer, to gain further insights into the influence of defects on structural and electronic properties. For both Ga- and As-terminated GaAs, O vacancies are considered in the interfacial $SrO_{1-\delta}$ layer with different vacancy concentrations $\delta = 0.25, 0.5$ and 0.75. For SrO-terminated $SrTiO_3$, Ga or As vacancies are created in the interfacial $Ga_{1-\theta}$ or $As_{1-\theta}$ layer with vacancy concentrations $\theta = 0.25, 0.5$ and 0.75. For Sr-terminated $SrTiO_3$, only As vacancies are considered in the interfacial $As_{1-\theta}$ layer with vacancy concentrations $\theta = 0.25, 0.5$ and 0.75. Other mixed O and Ga/As vacancies are not considered in this work due to the complexity of the possible interfacial configurations.

The proposed structures are fully relaxed and their electronic structures are calculated. All the structures with vacancies are found to be energetically less stable than the original SrO/Ga and Sr/As interfaces; nevertheless, studying the electronic behavior of these vacancies is important for understanding the interface structures and tailoring their properties. Since the metallicity of the $SrTiO_3$/GaAs heterostructure is determined by the valence and conduction states in the interfacial layers, the projected DOS on each element in the first $SrTiO_3$ and GaAs unit cells at the interface are plotted for the considered structures with vacancies in Figure 3.2.10. Only the $SrO/As_{0.5}$ interface exhibits semiconducting behavior with a sizable band gap, all the other interfaces are metallic. For $SrO_{1-\delta}$/Ga(As) ($\delta = 0.25, 0.5, 0.75$) interfaces,

the Fermi level is always pinned to the CBM of $SrTiO_3$. However, O vacancies induce extra dangling Ga or As states at valence band maximum (VBM) of GaAs, which reduces the band gap of GaAs at the interface. The similar pinning behavior is also reported in the $SrTiO_3$/Si hetero-interfaces [75; 76]. For $SrO/Ga(As)_{1-\theta}$ ($\theta = 0.25, 0.5, 0.75$) interfaces, the Fermi level can be unpinned from the CBM of $SrTiO_3$ and shifts towards the VBM as vacancy concentration increases. However, Ga and As vacancies result in extra dangling As and Ga states at Fermi level. In the case of $SrO/As_{0.5}$, the dangling states at GaAs surface can be eliminated and the Fermi level can be unpinned from $SrTiO_3$, making the interface semiconducting. For the experimentally observed Sr/As interface with As vacancies, the Fermi level is always pinned to the CBM of $SrTiO_3$ regardless of the vacancy concentration. From these observations, I can conclude that the 2DEG in $SrTiO_3$ is intrinsic to the $SrTiO_3$/GaAs interface and can be also contributed by O vacancies; however, it is possible for Ga or As vacancies to unpin the Fermi level from the localized 2DEG states. Both O and Ga/As vacancies will introduce more occupied Ga/As states near Fermi level, which reduces the band gap at the interface or makes the interface metallic.

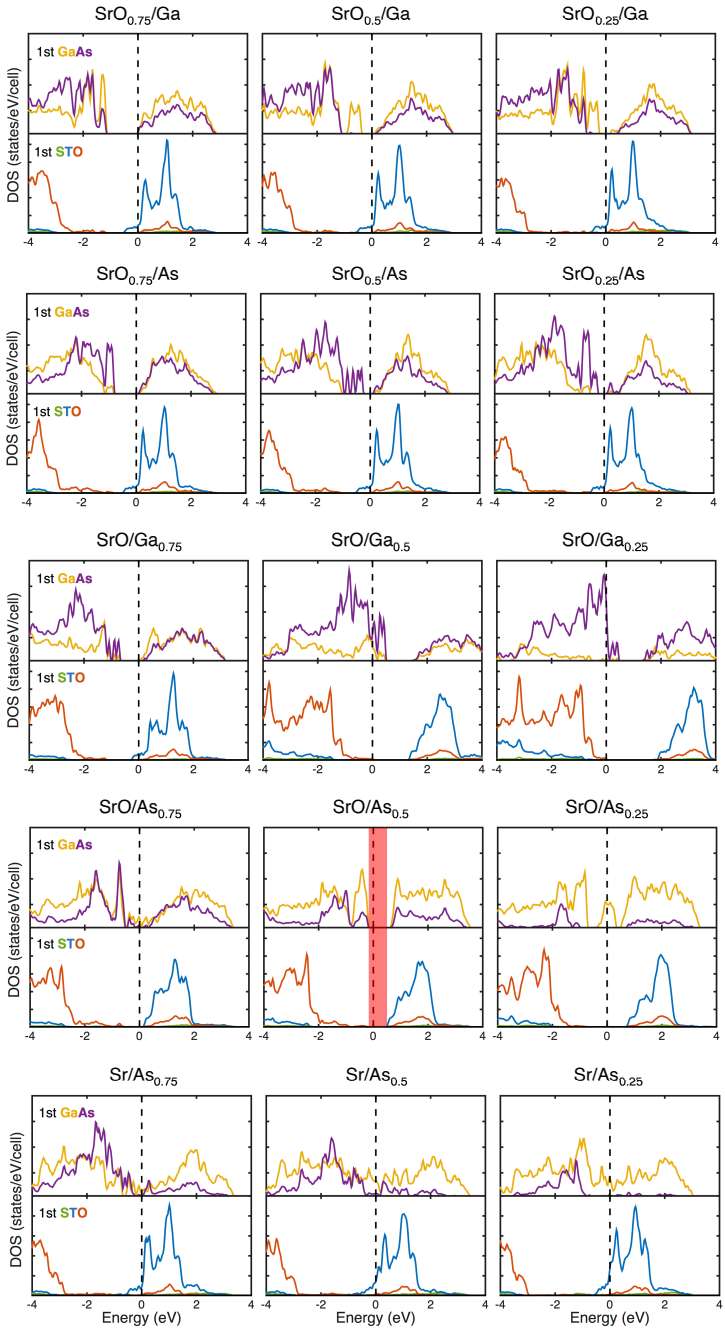

Figure 3.2.10. Projected DOS on each element in the first $SrTiO_3$ and GaAs unit cells for the defect-induced interfaces. Fermi level is shifted to zero. $SrO/As_{0.5}$ is semiconducting with band gap marked by the shaded red area.

3.3 Ferroelectric Switching in $BaTiO_3$ Thin Film

3.3.1 Experimental Setup

Single-crystalline $BaTiO_3$ was grown epitaxially on GaAs substrate using the MBE method with a 2-unit-cell $SrTiO_3$ nucleation layer [40]. The $BaTiO_3/SrTiO_3/GaAs$ cross-section TEM sample is prepared using focused ion beam (FIB) method. The thin flake prepared by FIB is then assembled into the ProtoChips E-chip which is designed for dedicated *in-situ* electrical experiments in TEM. The schematic of the experimental setup is shown in Figure 3.3.1. The sample is attached on the holey carbon film between two parallel Cu electrodes with a spacing of 3 μm. The top electrode is connected to the $BaTiO_3$ thin film through deposition of a platinum (Pt) layer on the top of $BaTiO_3$ thin film, while the bottom electrode is connected to the GaAs substrate. Electrical biases can be applied through the metal-oxide-semiconductor structure to create an external electrical field on the $BaTiO_3$ thin film.

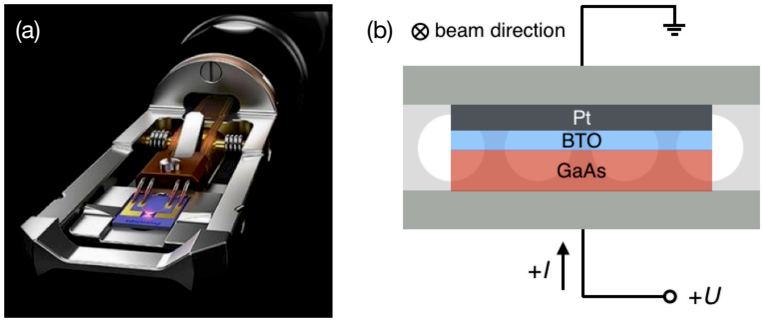

Figure 3.3.1. (a) ProtoChips Fusion^{TM} heating/electrical stage and E-chip. Adapted from http://www.protochips.com. (b) Schematic of the $BaTiO_3/SrTiO_3/GaAs$ sample attached on the E-chip used for the *in-situ* electrical experiment.

The STEM-HAADF images are acquired at 200 kV with a convergence semi-angle of 29 mrad and a collection angle from 90 to 170 mrad. The atomic-resolution HAADF images are recorded at magnification of 1.5×10^7 (pixel size of 0.027 nm) and pixel dwell time of 31 μs. For EELS at 200 kV, a convergence angle of 30 mrad and a collection angle with 35 mrad are used. Energy dispersions of 0.1 eV/channel and 0.3 eV/channel are used for the measurement of Ti $L_{3,2}$-edge and O K-edge ELNES. The exponential EEL spectrum background is subtracted from each spectrum and the resulting data are normalized with respect to the post edge intensity.

3.3.2 STEM Imaging and EELS Analysis

The HAADF image showing the sample attached on the E-chip at low magnification is illustrated in Figure 3.3.2. The sample is successfully connected with the electrodes and the $BaTiO_3$ thin film is located within the hole area in the vacuum.

The atomic-resolution HAADF image of the sample without electrical bias is shown in Figure 3.3.3(a). A 15-unit-cell thick $BaTiO_3$ film is observed to be epitaxially grown on 2-unit-cell $SrTiO_3$ buffer layer on As-terminated GaAs substrate with an abrupt $SrTiO_3$/GaAs interface. EEL spectra of Ti $L_{3,2}$-edge are taken from first four TiO_2 monolayers from the $SrTiO_3$/GaAs interface, as shown in Figure 3.3.3(b). The Ti L-edge in the $BaTiO_3$ interfacial layers exhibits four prominent peaks originating from the $3d^0$ states splitting into t_{2g} and e_g components, which corresponds to a Ti 4+ valence. However, the intensity of the third peak decreases in the $SrTiO_3$ layers, indicating a decrease of Ti valence from 4+ to a mixture of 3+ and 4+, due to interfacial O vacancies. Thus, the $SrTiO_3$/GaAs interface is polarized by the

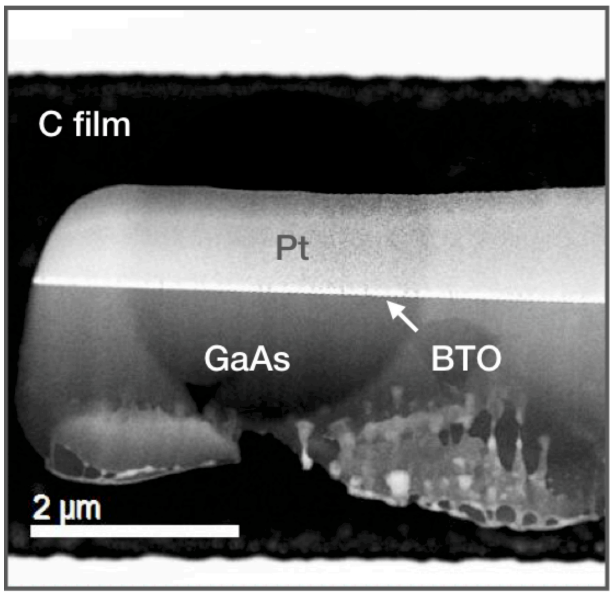

Figure 3.3.2. Low-magnification HAADF image showing the $BaTiO_3/SrTiO_3/GaAs$ sample attached on the holey C film between two Cu electrodes. Pt layer is deposited on the top of the $BaTiO_3$ thin film as electrode.

interfacial dipole in the [001] direction, creating a single-domain spontaneous polarization $\mathbf{P}_s$ in the $BaTiO_3$ film along [001] direction.

In-situ electrical biases of $U = \pm 3$ V are then applied to the sample to study the ferroelectric switching behavior in the $BaTiO_3$ film. The positions of the atomic columns in the HAADF images are determined using the 2D Gaussian fitting method as illustrated in the insets in Figure 3.3.4. The direction of polarization is then calculated by the displacement of Ti columns with respect to the center of four neighboring Ba columns in an averaged section from the HAADF image. From Figure 3.3.4(a), I can directly observe that, upon application of -3 V, Ti

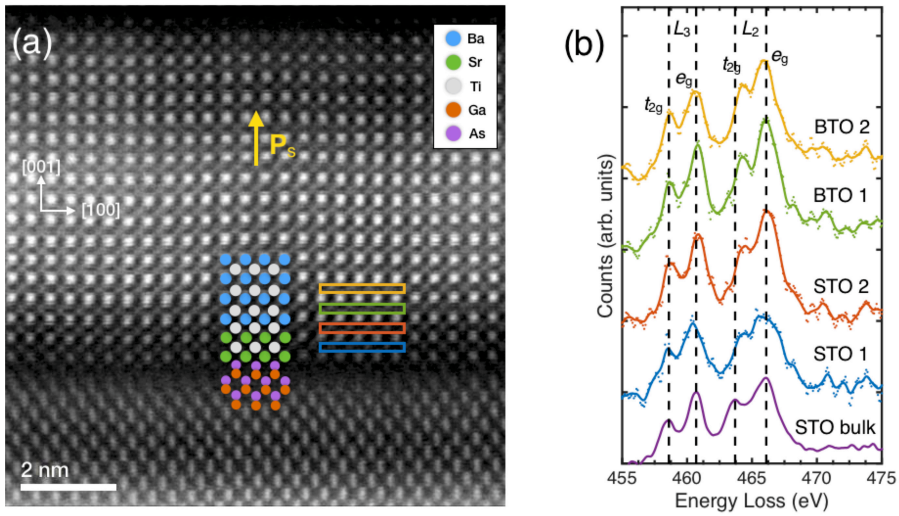

Figure 3.3.3. (a) Atomic-resolution HAADF image of the $BaTiO_3/SrTiO_3/GaAs$ sample without electrical bias. The proposed atomic columns are shown as inset. The spontaneous polarization $\mathbf{P}_s$ is in the [001] direction. (b) ELNES of Ti $L_{3,2}$-edge taken from the first four TiO_2 monolayers at the interface, corresponding to the colored rectangles in (a), along with that from $SrTiO_3$ bulk as reference. The spectra are aligned using L_3-t_{2g} peak and smoothed by Gaussian function with raw data shown as dots.

columns are displaced downwards with respect to the Ba columns, indicating the switching of polarization from [001] to [00$\bar{1}$] direction. The average displacement of Ti columns is measured as -0.16 Å. Upon application of +3 V, as shown in Figure 3.3.4(b), the polarization reverses with an average Ti displacement of +0.39 Å. The contrast of the $SrTiO_3/GaAs$ interface reduces significantly during the *in-situ* experiment as seen from the HAADF images. This damage might be caused by the accumulated electrical heat at the $SrTiO_3/GaAs$ interface under external biases. Spectra of O K-edge ELNES are measured within the $BaTiO_3$ film under different electrical biases as shown in Figure 3.3.4(c). It is observed that peak a, which is associated

with the Ti 3d-t_{2g} states, shifts towards higher energy by 0.4 eV after application of -3 V while shifts back to lower energy by 0.7 eV upon following application of $+3$ V. The energy shift confirms the structural change of TiO_6 octahedral under different external biases as I observed in the HAADF images.

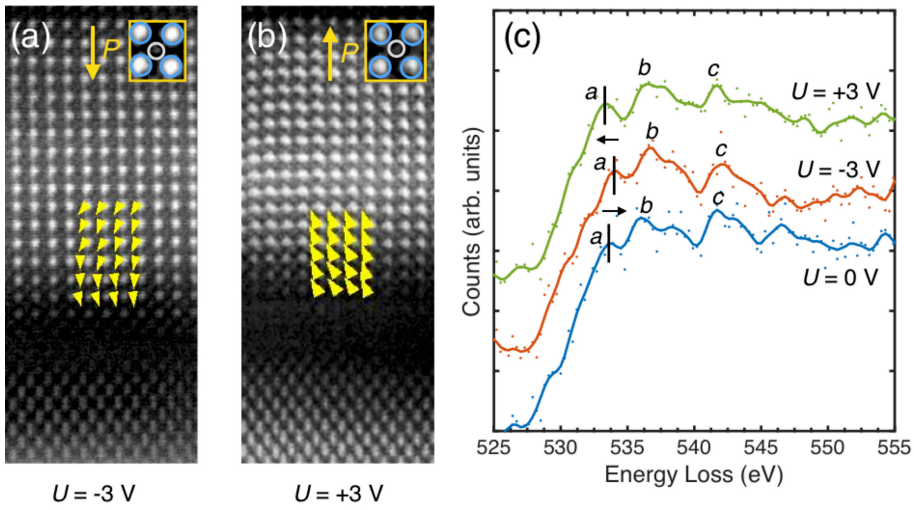

Figure 3.3.4. (a) and (b) Atomic-resolution HAADF images of the sample under -3 V and $+3$ V external biases, respectively. The direction of polarization in the calculated area is marked by the yellow triangles. (c) Spectra of O K-edge ELNES taken from the $BaTiO_3$ film under $U = 0, -3$ and $+3$ V. The spectra are aligned with respect to Ba $M_{5,4}$-edge (not shown) and smoothed by Gaussian function with raw data shown by dots. The three featured peaks are marked by a, b and c.

3.4 Summary

In this chapter, I study the structural and electronic properties of $SrTiO_3$/GaAs heterointerfaces using STEM-EELS combined first-principles calculations, and designed an *in-situ* STEM-EELS experiment to directly observe the ferroelectric switching behavior in $BaTiO_3$ thin film grown on $SrTiO_3$/GaAs. GaAs thick layer is grown on $SrTiO_3$ thin film on Si substrate by MBE method to find out the interfacial configuration to complement the previous studies of $SrTiO_3$ thin films grown on GaAs substrate. The interface is characterized using atomic-resolution HAADF imaging and EELS techniques. I observe an atomically abrupt interface between $SrTiO_3$ and GaAs with the interfacial configuration of O-deficient SrO layer in contact with As layer, which is identical with that of $SrTiO_3$ thin film deposited on GaAs substrate. (2×2) structural model of various interfacial compositions with regard to SrO, TiO_2, Sr, Ti, Ga and As terminations are constructed and fully relaxed using first-principle DFT calculations. Energetic stability of all the proposed interface structures are compared in formation energy phase diagrams. Two interfaces, with configurations SrO/Ga and Sr/As, are found to be energetically favorable under O-rich and O-poor conditions, respectively. The phase diagram also indicates that Ga-terminated GaAs surface is easily oxidized, resulting in a Ga_2O_3 interlayer. In the relaxed structure of SrO/Ga interface, GaAs surface is reconstructed via the formation of Ga-Ga dimers and Ga-O bonds, while the relaxed structure of Sr/As exhibits an abrupt interface without surface reconstruction, which is consistent with the experimentally observed structure. The driving force of interface reconstruction is the accommodation of interface polar discontinuity and the presence of interfacial O vacancies is crucial to obtain an abrupt interface.

Both of the two interfaces are metallic with a 2DEG of $0.5e^-$ per (1×1) unit cell localized at the bottom of Ti conduction band. Macroscopic band alignment analysis reveals that the SrO/Ga interface is a type I hetero-structure while Sr/As interface is a type II hetero-structure in agreement with the experiment. The electronic properties of the $SrTiO_3$/GaAs interfaces are further studied by examining the effects of O and Ga/As vacancies with different concentrations at the first SrO and Ga/As layers. The results show that the 2DEG in $SrTiO_3$ is intrinsic to the $SrTiO_3$/GaAs interface and can be enhanced by O vacancies; however, it is possible for Ga or As vacancies to unpin the Fermi level from the localized 2DEG states. The epitaxial $BaTiO_3$ thin film is grown on $SrTiO_3$/GaAs substrate by the MBE method. The TEM sample is prepared by FIB and assembled into a dedicated electrical chip for *in-situ* STEM-EELS characterization. Ferroelectric switching behavior in $BaTiO_3$ thin film under external biases of ± 3 V is directly observed through the displacement of Ti columns in the atomic-resolution HAADF images. The TiO_6 structural change is further confirmed by the energy shift in O K-edge ELNES. My results present a detailed understanding of the structural and electronic properties of the oxide-semiconductor heterostructures, which provides useful insights for future integration and designs of multifunctional MOS devices with smaller scale.

CHAPTER 4

OXYGEN-FUNCTIONALIZED MXENE NANORIBBONS

(The content in this chapter was previously published as Hong, L., Klie, R., Öğüt, S.: First-principles study of size- and edge-dependent properties of MXene nanoribbons. Physical Review B, 93:115412, 2016. Reuse license is shown in Appendix E.)

4.1 Introduction

Two-dimensional (2D) materials, also referred to single-layer materials, have been of significant interest owing to their unique properties and potential technological applications in nanoscale devices. Recently, a novel class of 2D materials, known as MXenes, has drawn significant attention stemming from their excellent properties such as high damage tolerance, oxidation resistance, and electrical and thermal conductivity [77; 78; 79; 80; 81; 82; 83; 84], and might be functionalized for other novel physical and chemical applications. Experimentally, MXenes have been synthesized by exfoliation from the bulk MAX phases [84; 82; 83; 81]. The MAX phases are a large family of layered, hexagonal carbides and nitrides with the general formula $M_{n+1}AX_n$, where $n = 1 - 3$, M is an early transition metal, A is an A-group (mostly IIIA and IVA) element and X is either carbon and/or nitrogen [85; 86; 87; 88]. MXenes can be achieved by etching the A layers in MAX solids using hydrofluoric acid solution. As a result, the surfaces of MXenes are always chemically functionalized/terminated with selective groups, such as O,

F or OH [82; 83]. Accordingly, bare MXenes have the formula $M_{n+1}X_n$ while functionalized MXenes have the formula $M_{n+1}X_nT_2$, where T represents functional terminations.

In the last few years, the mechanical and electronic properties of 2D MXenes have been intensively studied using first-principles calculations [89; 90; 91; 92; 93; 94; 95; 96; 97; 98; 99; 100; 101; 102; 103]. A previous study has shown that the thinnest and thicker MXenes exhibit different electronic properties, since the DOS at the Fermi level of thicker MXenes is much higher than that for the thinnest MXenes [90]. All of the bare MXenes are found to be metallic; however, after functionalization, some of the thinnest MXenes, such as Ti_2CO_2, Zr_2CO_2, Hf_2CO_2, Sc_2CO_2, Sc_2CF_2 and $Sc_2C(OH)_2$, become semiconducting with band gaps ranging from 0.24 to 1.8 eV [89].

By confinement of 2D materials, one-dimensional (1D) nanostructures, such as nanoribbons and nanotubes, can be created with considerably different physical properties from their 2D counterparts due to quantum confinement and surface effects [104; 105; 106]. For example, the widely studied 2D graphene is a semimetal, whereas the 1D graphene nanoribbons can be semiconductors with band gaps that can be tuned as a function of the ribbon width and edge configuration (armchair versus zigzag) [106; 107; 108; 105; 109; 110; 111; 112; 113; 114]. Studies on similar honeycomb-shaped nanoribbons obtained from 2D silicene [115; 116; 117; 118], boron nitride [119; 120; 121], transition-metal dichalcogenides [122; 123; 124; 125; 126], have also revealed interesting size and edge dependent properties in these 1D nanostructures. Some of the nanoribbons mentioned above have been fabricated using methods such as lithography, bottom-up synthesis and unzipping nanotubes [127; 128; 129]. However, only few first principles

studies have been reported on selected MXene nanoribbons: Zhao *et al.* examined the structural and electronic properties of bare and O-functionalized Ti_2C, Ti_3C_2, and V_2C nanoribbons at a few selected sizes [98], and Zhang *et al.* focused on the carrier mobility of Ti_2CO_2 nanoribbons [130].

In this chapter, I present results and analyses of my first-principles calculations on two prototypes of O-functionalized MXene nanoribbons: Ti_2CO_2 and Sc_2CO_2. I perform a systematic investigation of size and edge dependent properties by classifying all possible armchair and zigzag edge terminations. My results show that the semiconducting versus metallic character of MXene nanoribbons is largely dependent on their edge types, and can be understood in terms of an electron counting rule. For the semiconducting nanoribbons, the band gap evolution as a function of ribbon size is, in general, dependent on the lowest energy structural models of their 2D counterparts, and determined by a combination of factors such as quantum confinement, the energetic location of edge states, and the strength of the *d*-*d* hybridization imposed by geometrical factors.

4.2 Computational Setup

First-principles DFT calculations are carried out using the PAW method as implemented in the VASP, and the exchange-correlation functional of PBE. Plane wave energy cutoff is set as 450 eV. The structures are fully optimized with a maximum force criterion of 10^{-2} eV/Å. For 2D MXenes, $12 \times 12 \times 1$ and $42 \times 42 \times 1$ Monkhorst-Pack k point grids are used during structural optimization and DOS calculations, respectively. For 1D nanoribbons, the corresponding k point grids are $8 \times 1 \times 1$ and $24 \times 1 \times 1$. The 2D MXene sheets are separated from each

other in the non-periodic direction by a large vacuum of 20 Å. 1D nanoribbons are separated from each other by 20 Å and $10 - 20$ Å (depending on the size of the nanoribbon) in the non-periodic directions perpendicular to and along the plane of the nanoribbon, respectively. I perform convergence tests for all the parameters mentioned above to ensure the accuracy of the calculations. During my structural optimizations, I do not impose any symmetry, and I perform several calculations for the same structure starting with different initial magnetic moments for the transition metal element to ensure that the final optimized structures have the lowest energy.

4.3 Structural Models

As discussed in previous studies [90; 89; 131], three types of structural models for 2D M_2XT_2 are considered in this work (shown in Figure 4.3.1). In Model I, the top-layer T atoms are directly above the lower-layer M atoms while the bottom-layer T atoms are directly below the upper-layer M atoms (this is the so-called A-site for T atoms). In Model II, the top-layer (bottom-layer) T atoms are right above (below) the X atoms (this is the B-site for T atoms). Model III is a combination of Models I and II, in which the top-layer T atoms are right above the lower-layer M atoms (A-site), while the bottom-layer T atoms are right below the X atoms (B-site).

The 1D MXene nanoribbons are constructed by cutting a strip from the 2D sheet along either of the two (orthogonal) directions which result in armchair or zigzag type nanoribbons. This is shown for a Model I type nanoribbon in Figure 4.3.2. The corresponding armchair nanoribbons (ANRs) and zigzag nanoribbons (ZNRs) are characterized by size parameters n_a

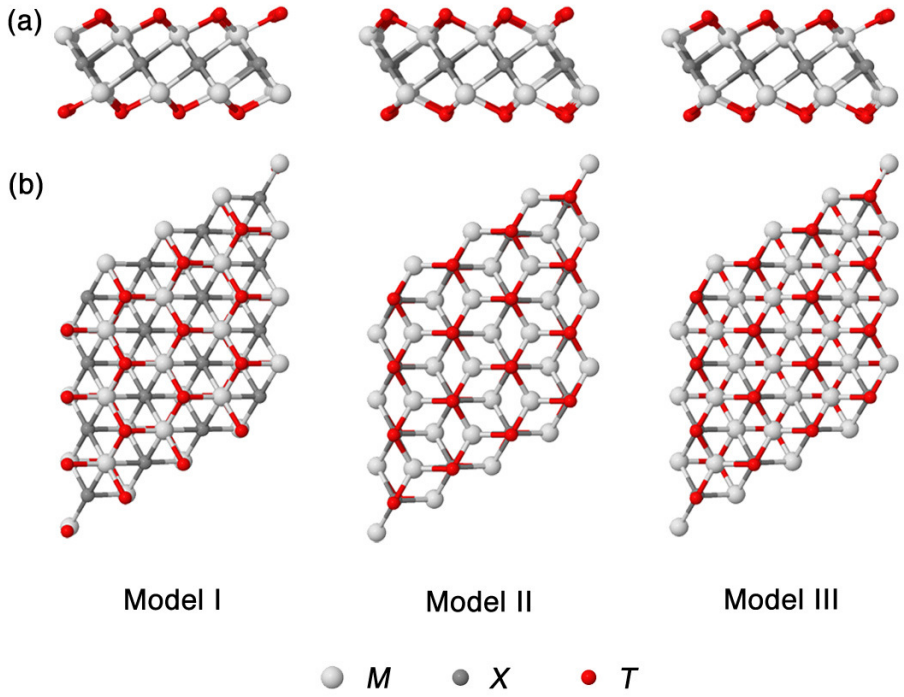

Figure 4.3.1. (a) Side views and (b) top views of three models of the functionalized M_2X systems (i.e., M_2XT_2) in $4 \times 4 \times 1$ unit cell. M, X and T elements are represented by white, dark gray and red balls, respectively.

and n_z, respectively, and denoted as n_a-ANR and n_z-ZNR. For ANRs, one can have only two types of structures: Those ANRs with an odd size parameter n_a have symmetric edges (with respect to a line passing through the middle of the ribbon and parallel to the periodic direction), while those with an even size parameter are asymmetric. The classification is more complicated for ZNRs due to two different kinds of atomic lines extending along the periodic direction. These atomic lines contain either rows of M/T atoms (with M atoms on top of T atoms or vice versa, which I denote as M for short) or rows of X atoms. The order of the

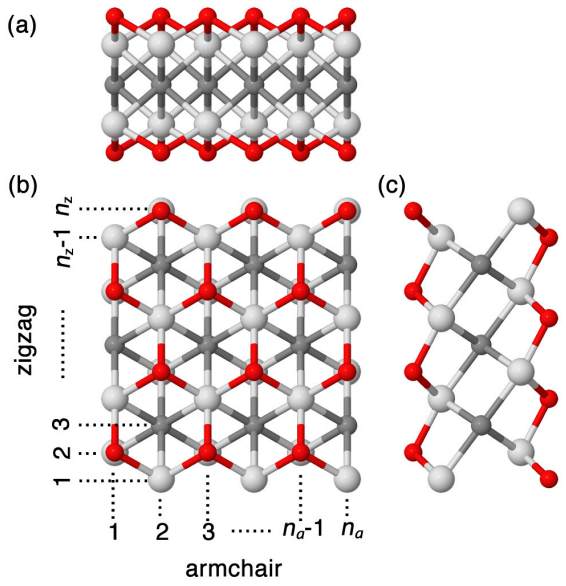

Figure 4.3.2. Schematic of 1D nanoribbon cut from a 2D MXene in Model I structure. (a)(c) are side views and (b) is top view of the nanoribbon. In (b), armchair (zigzag) nanoribbon is periodic in the vertical (horizontal) direction. The size parameter n_a (n_z) for armchair (zigzag) is defined according to the number of atomic lines in the vertical (horizontal) direction. M, X and T elements are represented by white, dark gray and red balls, respectively.

atomic lines in ZNRs can be represented as $...MMXMMX...$, resulting in three types of edges which are MMX, MXM and XMM, where the first letter denotes the outermost atomic line. Considering all combinations of starting and ending edges, six types of ZNR structures can, therefore, be achieved, as shown in Figure 4.3.3. (1) n_z-(MMX-MMX)-ZNR, where $n_z = 3p$ (p is a positive integer), representing ZNRs with the size of n_z and two edges of MMX and XMM; (2) n_z-(MXM-MXM)-ZNR, where $n_z = 3p$; (3) n_z-(MMX-MXM)-ZNR, where $n_z = 3p + 1$; (4) n_z-(XMM-MMX)-ZNR, where $n_z = 3p + 1$; (5) n_z-(MMX-XMM)-ZNR,

where $n_z = 3p + 2$; and (6) n_z-(MXM-MMX)-ZNR, where $n_z = 3p + 2$. According to these definitions, Figure 4.3.2 shows a 6-ANR or 11-(MMX-XMM)-ZNR (depending on whether the vertical or the horizontal direction is taken as the periodic direction of the nanoribbon). Similarly, Model II nanoribbons can be also classified into two types of ANRs and six types of ZNRs, while Model III nanoribbons can be classified into two types of ANRs and nine types of ZNRs due to three different kinds of atomic lines that they possess, as shown in Figure 4.3.4.

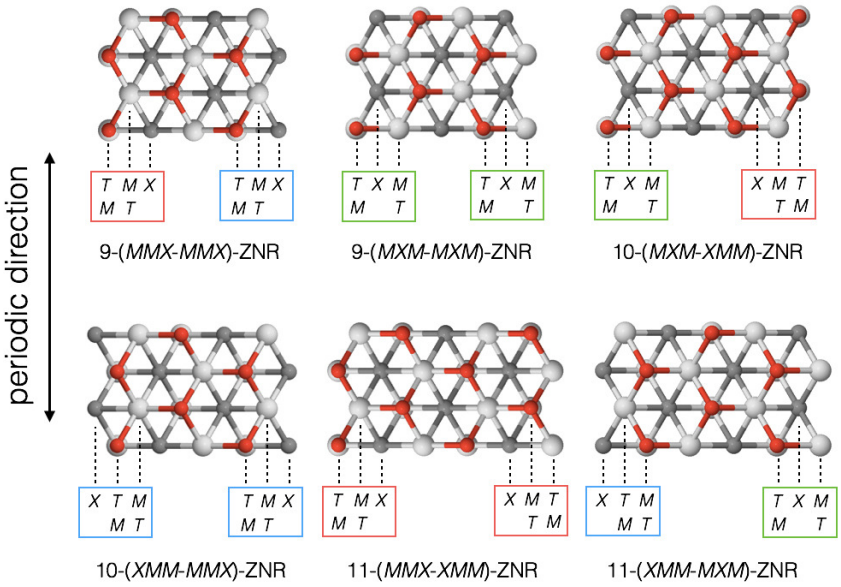

Figure 4.3.3. Top view of the unrelaxed structures for the six types of Model I ZNRs ($n_z = 9 - 11$) in $2 \times 1 \times 1$ unit cell. The same types of edges are boxed in the same color. M, X and T elements are represented by white, dark gray and red balls, respectively.

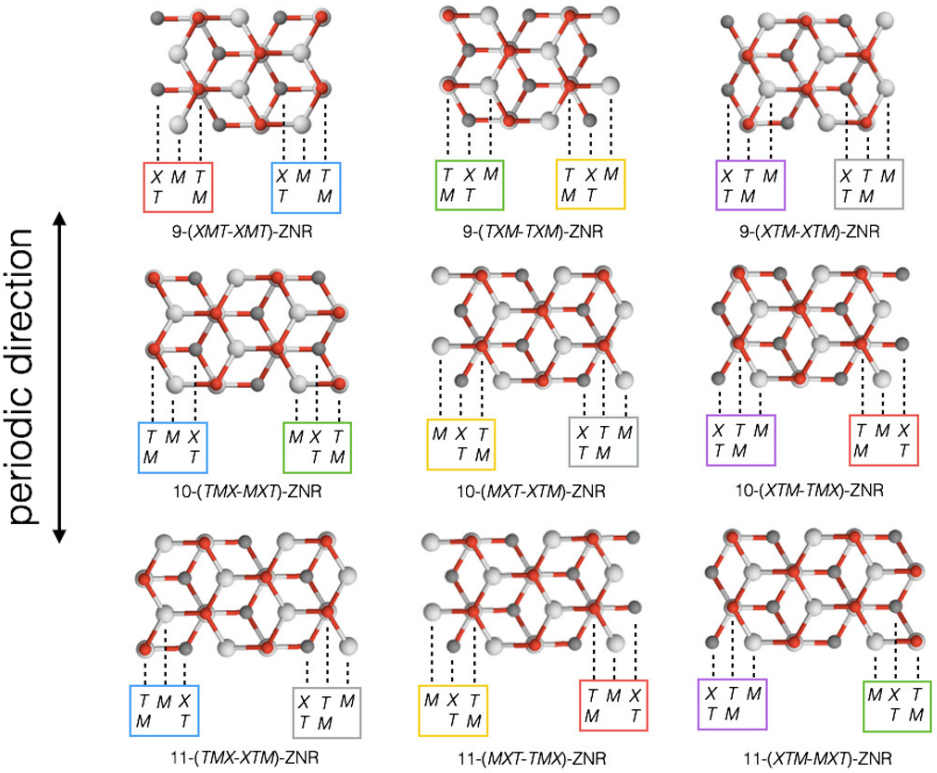

Figure 4.3.4. Top view of the unrelaxed structures for the nine types of Model III ZNRs ($n_z = 9 - 11$) in $2 \times 1 \times 1$ unit cell. The same types of edges are boxed in the same color. M, X and T elements are represented by white, dark gray and red balls, respectively.

4.4 Ti_2CO_2 Nanoribbons

Ti-MXenes have become the most intensively studied class of materials among all MXenes, mainly due to the fact that Ti_2C and Ti_3C_2 have been produced in experiments [82]. Among the functionalized Ti-MXenes, Ti_2CO_2 is the only one that has been found to be semiconducting, and here I use it as a prototype to study the size and edge effects in MXene nanoribbons.

4.4.1 Armchair Nanoribbons

Ti_2CO_2 ANRs of different widths (controlled by the size parameter n_a) are constructed from the 2D Ti_2CO_2 sheet with n_a ranging from 2 to 20, and are fully relaxed. My results show that all the Ti_2CO_2 nanoribbons with armchair edges inherit the semiconducting character of 2D Ti_2CO_2, and their band gaps are significantly dependent on the edge symmetry and width of the nanoribbon. The semiconducting character of ANRs have also been found in other 2D systems such as graphene, boron nitride and transition-metal dichalcogenides [105; 120; 125; 126].

Figure 4.4.1 shows the total DOS and projected DOS for Ti_2CO_2 2D sheet and two representative ANRs, 6-ANR (asymmetric) and 7-ANR (symmetric). The conduction band of the 2D sheet is primarily due to Ti $3d$ states, whereas the valence states between -6 and 0 eV can be divided into two sub-bands: Sub-band I between ~ -4 and 0 eV, which has almost equal contributions from Ti $3d$, C $2p$ and O $2p$, and Sub-band II between ~ -6 and -4 eV dominated primarily by O $2p$ orbitals with some Ti $3d$ character due to the strong hybridization between them. Sub-band I and II are separated by a small gap (~ 0.3 eV). As shown in Figure 4.4.1(b) and (c), while the size of the band gap is considerably different in the two types of ANRs, it is clear that both of them have gaps at the Fermi level rendering them as semiconductors. In the PDOS of 6-ANR and 7-ANR, sub-band II shifts upward and merges with Sub-band I. Apart from this small change and the increase in the band gap, the orbital characters of the bands for 6-ANR are very similar to those of the 2D sheet. However, for the 7-ANR there is an extra sharp peak, contributed mainly by Ti $3d$ states with small mixture of O $2p$ states, just above the VBM, forming the CBM which will be discussed later in this section.

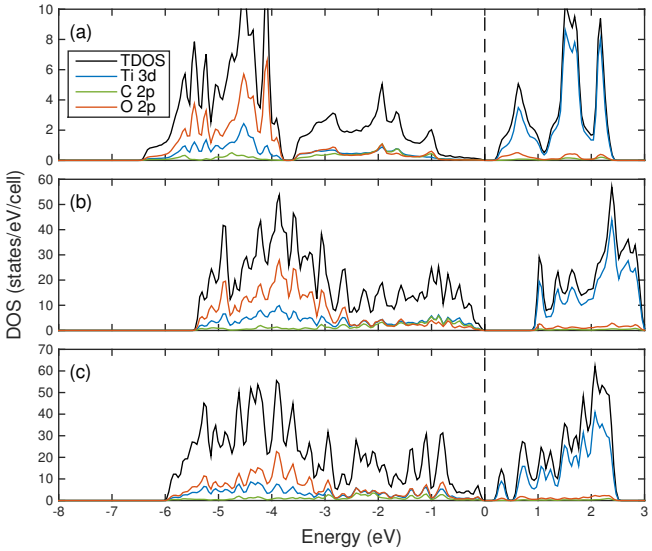

Figure 4.4.1. Total DOS and projected DOS on selected atomic orbitals of (a) 2D Ti_2CO_2, (b) Ti_2CO_2 6-ANR and (c) Ti_2CO_2 7-ANR. Fermi energy is shifted to zero at the top of valence bands.

The semiconducting character of Ti_2CO_2 ANRs can be explained by an electron counting (EC) rule: An ANR of width n_a has a stoichiometric unit cell with a composition of $(Ti_2CO_2)_{n_a}$. In the unit cell of 2D Ti_2CO_2 sheet, each Ti atom (with 4 valence electrons) can provide 2 electrons for C to form a Ti-C bond and 2 electrons for the neighboring O atom to form a Ti-O bond. This results in filling of p orbitals of both C and O, while leaving the Ti d states empty. As shown in Table I, when an ANR is cut from the 2D sheet, each of the two ANR edges ends up with 4 Ti dangling bonds, 2 C dangling bonds and 2 O dangling bonds in the unit cell. Accordingly, the Ti dangling bonds provide the required extra electrons (8 per edge per unit cell) to saturate the dangling bonds of both C and O. Thus, as in the 2D sheet, the

valence bands of ANRs originate primarily from the filled p orbitals of C and O atoms, while the conduction bands are formed from the (empty) Ti $3d$ orbitals. I note there is only one type of edge for ANRs. This is clearly evident for symmetric ANRs, while for asymmetric ones, one edge is a uniform shift with respect to the other by half the unit cell parameter along the periodic direction. Therefore, the EC rule is satisfied for both edges, which makes it possible for all ANRs to restore the semiconducting character of the 2D sheet. As I will see later for the case of ZNRs, when either edge fails to satisfy the electron counting rule, this makes the corresponding nanoribbon have a metallic character.

TABLE I

NUMBER OF DANGLING BONDS D FOR DIFFERENT TYPES OF EDGES IN THE UNIT CELL OF Ti_2CO_2 NANORIBBONS. THE SUBSCRIPT Ti-C REPRESENTS THE Ti DANGLING BOND WITH C REMOVED.

	$D_{\mathrm{Ti-C}}$	$D_{\mathrm{Ti-O}}$	$D_{\mathrm{C-Ti}}$	$D_{\mathrm{O-Ti}}$
ANR edge	2	2	2	2
ZNR-CTiTi edge	0	1	3	1
ZNR-TiTiC edge	3	1	1	0
ZNR-TiCTi edge	1	2	1	2

Next, I discuss the variation of the band gap of ANRs as a function of size, plotted in Figure 4.4.2. It can be seen that the evolution of the band gap for asymmetric (with even n_a)

and symmetric ANRs (with odd n_a) as a function of size is quite different at small sizes. As the width of the nanoribbons increases, this difference disappears, and the band gaps of both types of ANRs slowly converge to the band gap of the 2D Ti_2CO_2 which is 0.32 eV at the PBE level. The band gaps of small-sized asymmetric ANRs increase dramatically as the ribbon size decreases due to quantum confinement [132]. However, for small-sized symmetric ANRs (such as for $n_a = 3$ and 5), the band gaps are even smaller than that of the 2D sheet. This unusual band gap variation is due to the appearance of a sharp peak in the DOS, mentioned above, arising from a very flat band just above the VBM, as shown in Figure 4.4.3 for the case of 7-ANR. This flat band has predominantly Ti d_{xy} character with a very small O $2p$ admixture, and occurs in small-sized symmetric ANRs ($n_a < 10$). As shown in Figure 4.4.3, this band is associated with a particular row of Ti atoms spanning the width of the ANR. The presence (absence) of this flat band in the band structure of symmetric (asymmetric) ANRs is intimately related to the particular geometry and relaxation patterns of the two different types of ANRs, as I briefly explain below focusing on $n_a = 6$ and 7.

The relaxed structures of the unit cell of 6- and 7-ANR are shown in Figure 4.4.4. Before relaxation, an ANR of width n_a can be viewed as a layered structure with one Ti_2CO_2 in each layer per unit cell and equal spacings between two adjacent layers across the width of the ribbon. Upon relaxation, the two outermost layers are always observed to be tightly bound to each other and have weaker interactions with (farther away from) the third layer from the edge. For small sizes ($n_a \leq 10$), the asymmetric ANRs with an even number of layers are observed to form a series of separated bi-layers, while the symmetric ANRs with an odd number of layers

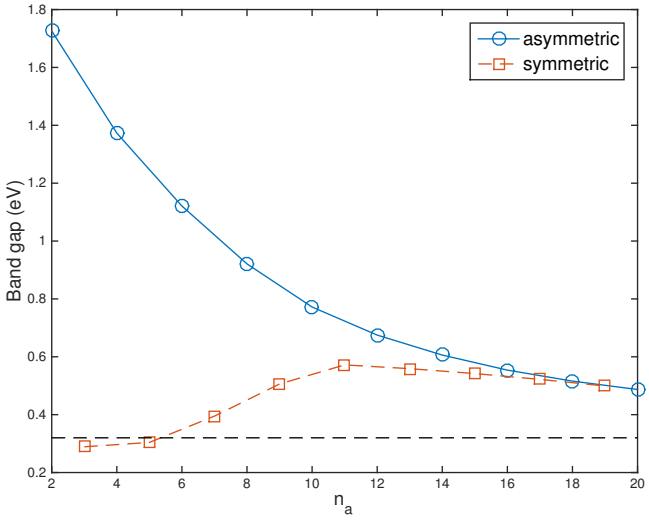

Figure 4.4.2. Band gap variation as a function of size n_a ($n_a = 2 - 20$) for Ti_2CO_2 ANRs. The blue curve with circles shows asymmetric ANRs with even n_a, the red curve with squares shows symmetric ANRs with odd n_a. The dashed line marks the band gap of 2D Ti_2CO_2.

have a symmetry plane at the center of the ribbon, which prevents the formation of separated bi-layers in the middle of the ribbon. As a result of these different relaxation patterns, the Ti-Ti distances across the width of the ribbon are different for the two types of ANRs. As shown in Figure 4.4.4, there are two rows of Ti atoms along the ribbon width in each unit cell. For asymmetric ANRs with an even n_a, there are $n_a/2$ Ti atoms in each row (3 atoms in each row for the 6-ANR as shown). For symmetric ANRs with an odd n_a, there are $(n_a + 1)/2$ Ti atoms in one row and $(n_a - 1)/2$ Ti atoms in the other (4 atoms in one row and 3 atoms in the other for the 7-ANR as shown). In the 6-ANR, the average relaxed Ti-Ti distance in each row is 3.03 Å, very close to the corresponding Ti-Ti distance in the 2D sheet, which is 3.04 Å.

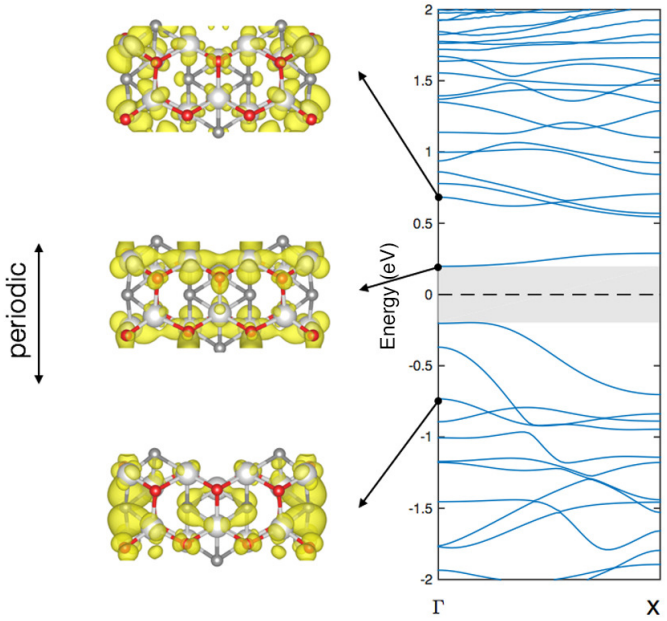

Figure 4.4.3. Top view of charge density isosurfaces (isovalue is set as 0.02 $e^{-}/\text{Å}^3$) for selected points in the band structure of Ti_2CO_2 7-ANR. Ti, C and O are represented by white, dark gray and red balls, respectively. The middle isosurface shows the state due to the significant Ti *d*-*d* hybridization which is discussed in detail in the text, while the other two isosurfaces show the edge states that appear at higher (lower) energies compared to CBM (VBM). The Fermi energy is shifted to zero at the center of the band gap.

In the 7-ANR, the average relaxed Ti-Ti distances in the 4-atom and 3-atom rows are 2.92 Å and 3.21 Å, respectively. Therefore, the 4-atom-row is significantly compressed by $\sim 4\%$ while the 3-atom-row is stretched by $\sim 5.6\%$ after relaxation. The flat band of predominantly Ti d_{xy} character mentioned above originates from Ti atoms in this 4-atom row due to the significant reduction in the Ti-Ti distance which allows for an appreciable *d*-*d* hybridization. In the 6-ANR, there is no such Ti *d*-*d* interaction, and the bands near the Fermi level look quite similar to the bands in the 2D sheet, other than a considerable increase in the band gap value due to

quantum confinement. After $n_a = 10$, the central part of the nanoribbon begins to converge to the geometry of the 2D sheet, reducing the tendency to form separated bi-layers in asymmetric ANRs and Ti *d*-*d* interaction in symmetric ANRs. Therefore, the band gaps of both asymmetric and symmetric ANRs converge (albeit slowly) to the value for the 2D sheet as n_a gets larger and larger. The similar even-odd oscillation behavior of band gaps has also been reported for rutile TiO_2 ultrathin films [133]. Finally, I note that ANRs also have states in the vicinity of the band gap that are mainly localized at the edges, however, these edge states appear higher up (lower down) in the conduction (valence) band manifold, as shown in Figure 4.4.3 for $n_a = 7$.

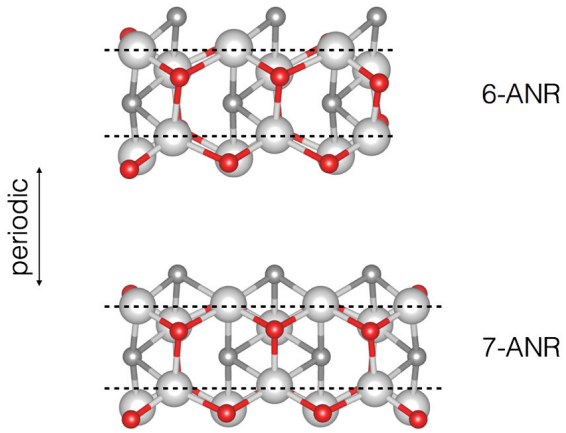

Figure 4.4.4. Top view of the relaxed structures of Ti_2CO_2 6-ANR and 7-ANR unit cells. Ti, C and O are represented by white, dark gray and red balls, respectively. The featured Ti rows are marked by black dashed lines.

4.4.2 Zigzag Nanoribbons

Since a ZNR edge is determined by the atomic composition and sequencing of the three outermost atomic lines, I considered ZNRs with n_z larger than 6 in order to study the edge effects on the nanoribbon. Furthermore, ZNRs with $n_z < 9$ are found to be undergo significant reconstructions after relaxation since their widths and thicknesses are comparable to each other (they are more like nanorods). Thus, in the following discussion, I focus on sizes from $n_z = 9$ to 23. Since there are two ZNRs with different edge structures for a given n_z, this means I focus on 30 different ZNRs. In other words, in terms of the 6 different ZNR types, I consider 5 different sizes for each ZNR type. Distinct from the ANRs, most of the Ti_2CO_2 ZNRs are found to be metallic. Similar observations have been reported for 2D MoS_2 and $NiSe_2$, whose ZNRs without hydrogen passivation are all metals whereas their 2D sheets are semiconductors [126; 125].

The spin-resolved total DOS of 6 types n_z-ZNR ($n_z = 9 - 11$) are plotted in Figure 4.4.5. Only the 9-(TiCTi-TiCTi)-ZNR is found to be a semiconductor whereas others are all metallic. Among these metallic ZNRs, 9-(TiTiC-TiTiC)-ZNR, 10-(TiTiC-CTiTi)-ZNR, 10-(CTiTi-TiTiC)-ZNR and 11-(TiCTi-TiTiC)-ZNR have net magnetic moments, while 11-(TiTiC-CTiTi) is non-magnetic. The electronic and magnetic properties of larger ($n_z > 11$) ZNRs follow the same trends.

Similar to the case discussed earlier for ANRs, the semiconducting/metallic nature of ZNRs can be understood using the EC rule. $n_z = 3p$-(TiCTi-TiCTi)-ZNRs have the stoichiometric unit cells and two TiCTi edges. As shown in Table I, TiCTi edge has 3 Ti dangling bonds, 1

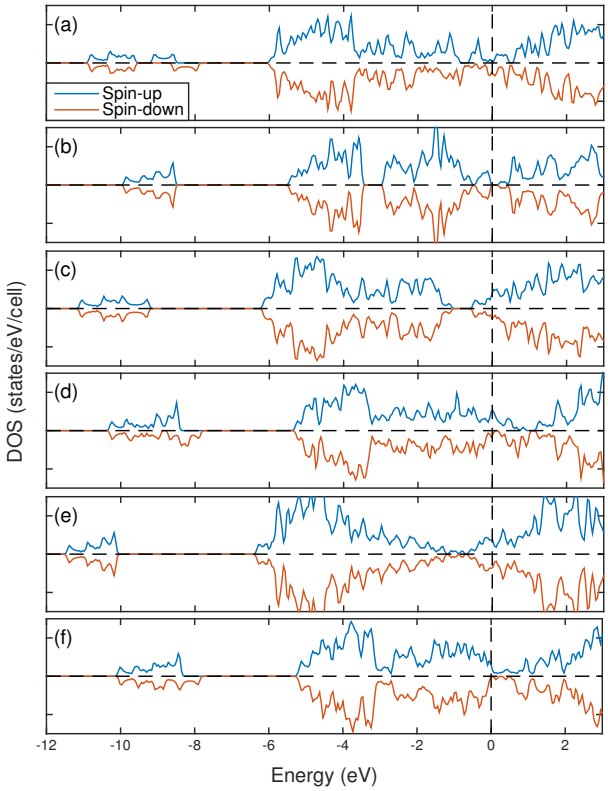

Figure 4.4.5. Spin-resolved TDOS of the 6 types of ZNRs: (a) 9-(TiTiC-TiTiC)-ZNR, (b) 9-(TiCTi-TiCTi)-ZNR, (c) 10-(TiTiC-TiCTi)-ZNR, (d) 10-(CTiTi-TiTiC)-ZNR, (e) 11-(TiTiC-CTiTi)-ZNR and (f) 11-(TiCTi-TiTiC)-ZNR. Fermi energy is shifted to zero and set at the top of valence bands for semiconductors.

C dangling bond, and 2 O dangling bonds in the unit cell. Hence, all of the dangling bonds on C and O atoms can be filled and those on Ti atoms are left empty in a TiCTi type edge. Since both of the edges are saturated and the unit cell is stoichiometric, (TiCTi-TiCTi)-ZNRs are able to restore the semiconducting character of the 2D sheet after edge reconstruction. For CTiTi

and TiTiC edges on the other hand, the excess electrons donated by the Ti dangling bonds cannot fully saturate the C and O dangling bonds (that is, $D_{\mathrm{Ti-C}} + D_{\mathrm{Ti-O}} \neq D_{\mathrm{C-Ti}} + D_{\mathrm{O-Ti}}$ for these edge types, using the notation in Table I). Since the other 5 types of ZNRs have at least one edge that is of the CTiTi or TiTiC type (as shown in Figure 4.3.3), they all turn out to be metallic.

To provide further support for the explanations above, the projected DOS (sum of spin up and down) of the three types of ZNR edges are plotted in Figure 4.4.6. In CTiTi edge, Ti dangling bonds cannot provide enough electrons to saturate the dangling bonds of the outermost C atom (i.e., $D_{\mathrm{Ti-C}} + D_{\mathrm{Ti-O}} < D_{\mathrm{C-Ti}} + D_{\mathrm{O-Ti}}$), thus there is a strong signal of C $2p$ orbital hybridized with Ti $3d$ orbital around Fermi level due to the dangling states in the C atom. In TiTiC edge, there are more Ti dangling bonds than the sum of C and O dangling bonds (i.e., $D_{\mathrm{Ti-C}} + D_{\mathrm{Ti-O}} > D_{\mathrm{C-Ti}} + D_{\mathrm{O-Ti}}$), which leads to Ti atoms not being fully ionized. Hence, the Fermi energy shifts upward and there is a significant contribution to the DOS at the Fermi level due to these Ti $3d$ states, rendering the system metallic. However, in the TiCTi edge, there is a gap between the valence and conduction bands because all the dangling bonds are either saturated or fully empty. Like the 2D Ti_2CO_2, the valence bands of TiCTi edge can also be divided into two Sub-bands I (-3 to 0 eV) and II (-6 to -3 eV) with a gap in the middle. Sub-band I shows strong hybridization of Ti $3d$-C $2p$ and Ti $3d$-O $2p$ orbitals corresponding to the Ti-C and Ti-O bonds. Therefore, the TiCTi edge retains the main characteristics of the 2D sheet in this type of nanoribbon. I note that a gap at the Fermi level in the PDOS of a TiCTi edge is present, even though the corresponding ZNR may have metallic character overall. For

example, for 10-(TiCTi-CTiTi)-ZNR and 11-(CTiTi-TiCTi)-ZNR both of which have metallic character overall (since at least one of the edges is not of the TiCTi type), when the PDOS is calculated by projecting onto atomic orbitals centered on atoms at the TiCTi edge, one can observe the opening of the gap at the Fermi level, as shown in Figure 4.4.6(c).

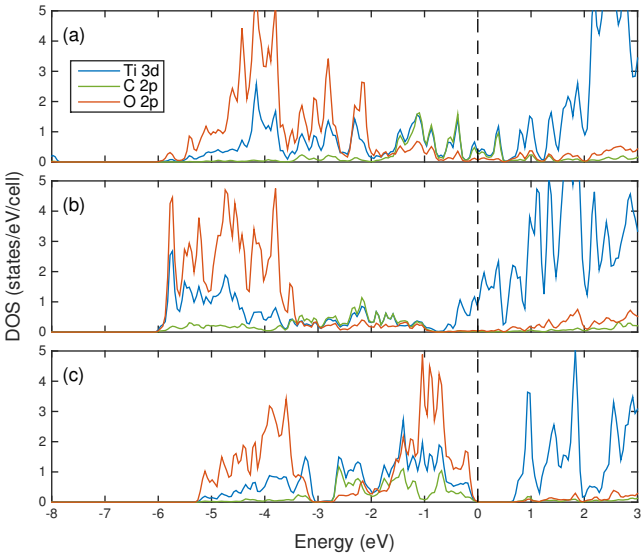

Figure 4.4.6. Projected DOS (sum of spin up and down) on selected atomic orbitals of (a) CTiTi edge, (b) TiTiC edge and (c) TiCTi edge for Ti_2CO_2 ZNRs. Two Ti, one C and one O atoms are considered for each edge. Fermi energy is shifted to zero and set at the top of valence bands for semiconductors.

The band gaps of the (TiCTi-TiCTi)-ZNR family are measured to study the size effect on semiconducting ZNRs, as shown in Fig. Figure 4.4.7. I find that the band gaps for $n_z \geq 12$ decrease and slowly converge to that of 2D sheet (0.32 eV). This band gap evolution pattern

is similar to that of ANRs and can be rationalized by quantum confinement effect. A small exception to this trend occurs for 9-(TiCTi-TiCTi)-ZNR, which has a small band gap of 0.32 eV due to a particularly dispersive conduction band. My analysis of the wavefunction characters for the valence and conduction bands near the band gap shows that edge states typically appear at the CBM (the 9-(TiCTi-TiCTi)-ZNR is an exception to this), but the VBM is bulk-like, with filled edge states appearing further down valence band.

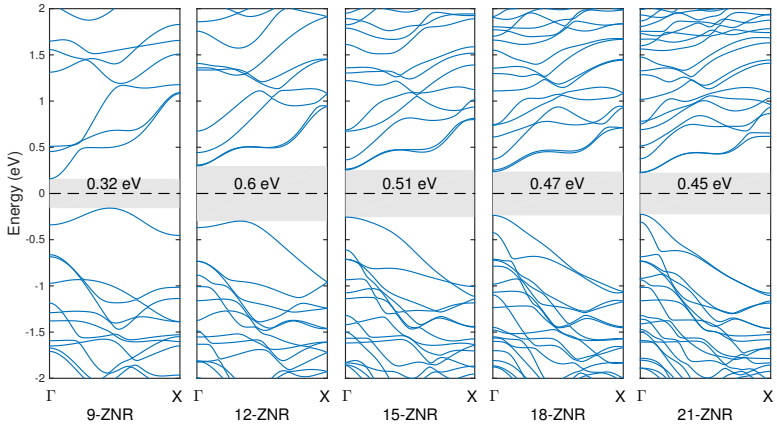

Figure 4.4.7. Band structures of semiconducting Ti_2CO_2 ZNRs ($n_z = 9 - 21$). Fermi energy is shifted to zero and set at the center of the band gap.

4.5 Sc_2CO_2 Nanoribbons

The lowest energy structure of Sc_2CO_2 2D sheet corresponds to model III in which the two surfaces (below and above the central C layer) are inequivalent since the functional groups are

located at different sites (A-site and B-site). Its nanoribbons can, therefore, be expected to exhibit different structural and electronic properties compared to those of Ti_2CO_2.

4.5.1 Armchair Nanoribbons

Sc_2CO_2 ANRs with $n_a = 2 - 10, 20$ are constructed from the 2D sheet and fully relaxed. The relaxed structures for Sc_2CO_2 2D sheet and ANRs at selected sizes ($n_a = 5, 10, 20$) are plotted in Figure 4.5.1. Unlike the symmetric location of the C layer with respect to the two surfaces in Model I structures, the C layer in Model III structures is closer to the B-site O layer than to the A-site O layer, resulting in a larger atomic concentration at the lower surface of the sheet as shown in Figure 4.5.1. When a nanoribbon is cut from the 2D sheet, since periodicity is no longer imposed across the ribbon width, this atomic concentration imbalance at the two surfaces can be relieved by stretching and compressing of the two surfaces. As a result, the lowest-energy structures of Model III nanoribbons are not flat, but rather bent as shown with some examples in Figure 4.5.1. I can quantify this bending by computing the curvature $\kappa = 1/R$, where R is the radius of the circle fitted to the positions of the the B-site O groups (the lower layer of O atoms shown in the insets). As I can see from Figure 4.5.1, κ decreases as the n_a increases, which means the curvature effect gets weaker as the nanoribbon grows, as expected. The curvature of MXene has already been observed in experiments [82], where some functionalized Ti_3C_2 nanosheets are bent to radius less than 20 nm (i.e., $\kappa \geq 0.5 \times 10^{-2}/\text{Å}$).

Similar to Ti_2CO_2 ANRs, Sc_2CO_2 ANRs are found to be semiconducting, which can also be explained by EC rule. However, the bonding mechanism in Sc_2CO_2 2D sheet is different from that in Ti_2CO_2 2D sheet due to their different structural models. In the unit cell of Sc_2CO_2 2D

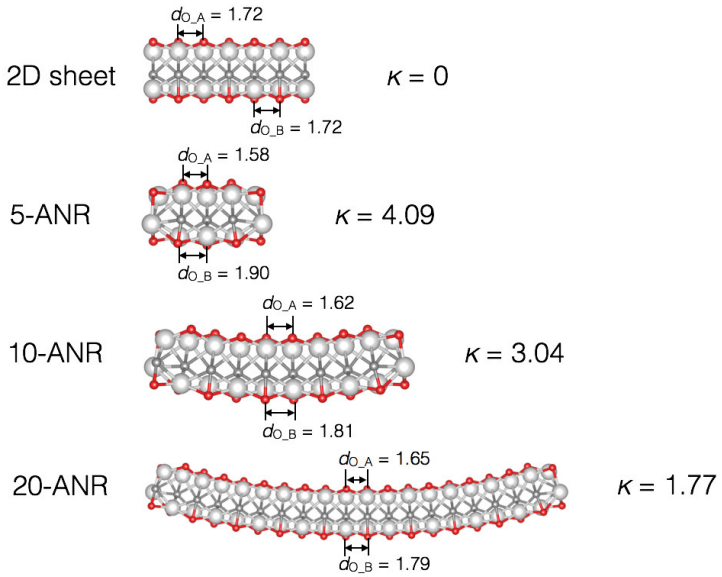

Figure 4.5.1. Side view of the relaxed structures of the 2D sheet, 5-ANR, 10-ANR and 20-ANR unit cells for Sc_2CO_2. The averaged distance for A-site (B-site) O atoms d_{O_A} (d_{O_B}) in Å is labeled for each structure, along with the curvature κ in units of 10^{-2}/Å. Sc, C and O are represented by white, dark gray and red balls, respectively.

sheet, A-site Sc (with 3 valence electrons) can provide 2 electrons for A-site O and 1 electron for C, while B-site Sc can provide 2 electrons for C and 1 electron for B-site O. As a result, both C and the B-site O have one of their $2p$ orbitals containing only 1 electron. These two orbitals hybridize with each other and can form C-O bonding and antibonding states [89]. The C-O bonds are shown in Figure 4.5.1. An ANR of width n_a has a stoichiometric unit cell with a composition of $(Sc_2CO_2)_{n_a}$. When an ANR is cut from the 2D sheet, the C-O bond is not broken and each of the two ANR edges ends up with 4 Sc dangling bonds, 2 C dangling bonds and 2 O dangling bonds in the unit cell as shown in Table II. Accordingly, the Sc dangling

TABLE II

NUMBER OF DANGLING BONDS D FOR DIFFERENT TYPES OF EDGES IN THE UNIT CELL OF Sc_2CO_2 NANORIBBONS. THE SUBSCRIPT Sc-C REPRESENTS THE Sc DANGLING BOND WITH C REMOVED.

	$D_{\mathrm{Sc-C}}$	$D_{\mathrm{Sc-O}}$	$D_{\mathrm{C-Sc}}$	$D_{\mathrm{O-Sc}}$
ANR edge	2	2	2	2
ZNR-CScO edge	0	1	3	2
ZNR-OScC edge	3	2	0	1
ZNR-OCSc edge	1	1	2	1
ZNR-ScCO edge	1	2	1	1
ZNR-COSc edge	0	0	3	2
ZNR-ScOC edge	3	2	0	0

bonds can provide the required extra electrons (6 per edge per unit cell) to saturate the dangling bonds of both C and O, restoring the system as semiconductor. It is noteworthy that due to the curvature of nanoribbon, the edge A-site Sc and B-site O atoms form a new Sc-O bond as shown in Figure 4.5.1. Therefore, the edge A-site Sc provides 1 electron to A-site O and 2 electron to C, while the B-site Sc provides each of the A-site O, B-site O and C with 1 electron, which results in the edge reconstruction. This can be seen in the PDOS of ANR edge shown in Figure 4.5.2(b), where a strong signal of Sc $3d$-O $2p$ hybridization appears at around -0.5 eV.

The band structure evolution for Sc_2CO_2 ANRs ($n_a = 6 - 10$) is plotted in Figure 4.5.3(a). Distinct from Ti_2CO_2, the band gaps of Sc_2CO_2 ANRs are nearly size-independent with band gap values around 1.27 eV, which is lower than that of the 2D sheet (1.86 eV). The reduction in the band gap compared to the 2D sheet is due to appearance of strong edge states that now

form the VBM and CBM as shown in Figure 4.5.3(b). This is unlike what is observed in the Ti_2CO_2 ANRs, where the edge states also appear in the band structure, but they are further up (down) in the conduction (valence) bands as shown in Figure 4.4.3. The edge states in Sc_2CO_2 ANRs can be attributed to the edge reconstruction as discussed before. Without these edge states, the band gaps would increase to values that are comparable to that of the 2D sheet. These results indicate the importance of the underlying structural model in determining the band gap of the ANRs.

4.5.2 Zigzag Nanoribbons

As mentioned earlier, Model III ZNRs have more complicated edge structures. As shown in Figure 4.3.4, the sequence of the atomic lines in Sc_2CO_2 ZNRs is ...O/Sc-Sc-C/O-O/Sc-Sc-C/O..., resulting in six types of edges which are O/Sc-Sc-C/O, C/O-Sc-O/Sc, Sc-C/O-O/Sc, O/Sc-C/O-Sc, C/O-O/Sc-Sc and Sc-O/Sc-C/O. Considering all combinations of starting and ending edges, nine types of ZNRs can, therefore, be achieved. Here I use O, C and Sc to represent O/Sc, C/O and Sc lines, respectively. For instance, 9-(OScC-OScC)-ZNR represents ZNR with nine atomic lines and two edges of O/Sc-Sc-C/O and C/O-Sc-O/Sc. The nine types of ZNRs with $n_z = 9 - 11$ are constructed and fully relaxed.

All types of Model III ZNRs are observed to be metallic. Again, the metallic nature of these ZNRs can be understood using the EC rule, which is similar to the case discussed for Ti_2CO_2 ZNRs. As shown in Table II, for each ZNR edge type, $D_{\mathrm{Sc-C}} + D_{\mathrm{Sc-O}} \neq D_{\mathrm{C-Sc}} + D_{\mathrm{O-Sc}}$. Therefore, none of the six types of ZNR edges can be saturated, rendering the ZNRs as metals.

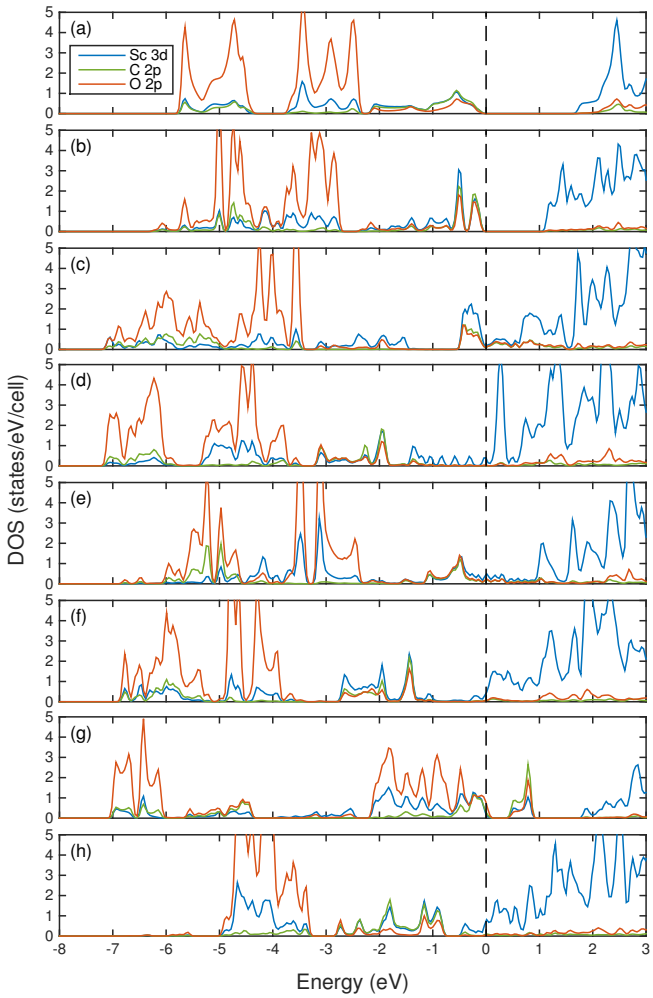

Figure 4.5.2. Projected DOS on selected atomic orbitals of (a) 2D Sc_2CO_2, (b) ANR edge, (c) ZNR-CScO edge, (d) ZNR-OScC edge and (e) ZNR-OCSc edge, (f) ZNR-ScCO edge, (g) ZNR-COSc edge, (h) ZNR-ScOC edge. Two Sc, one C and one O atoms are considered for each edge. Fermi energy is shifted to zero and set at the top of valence bands for semiconductors.

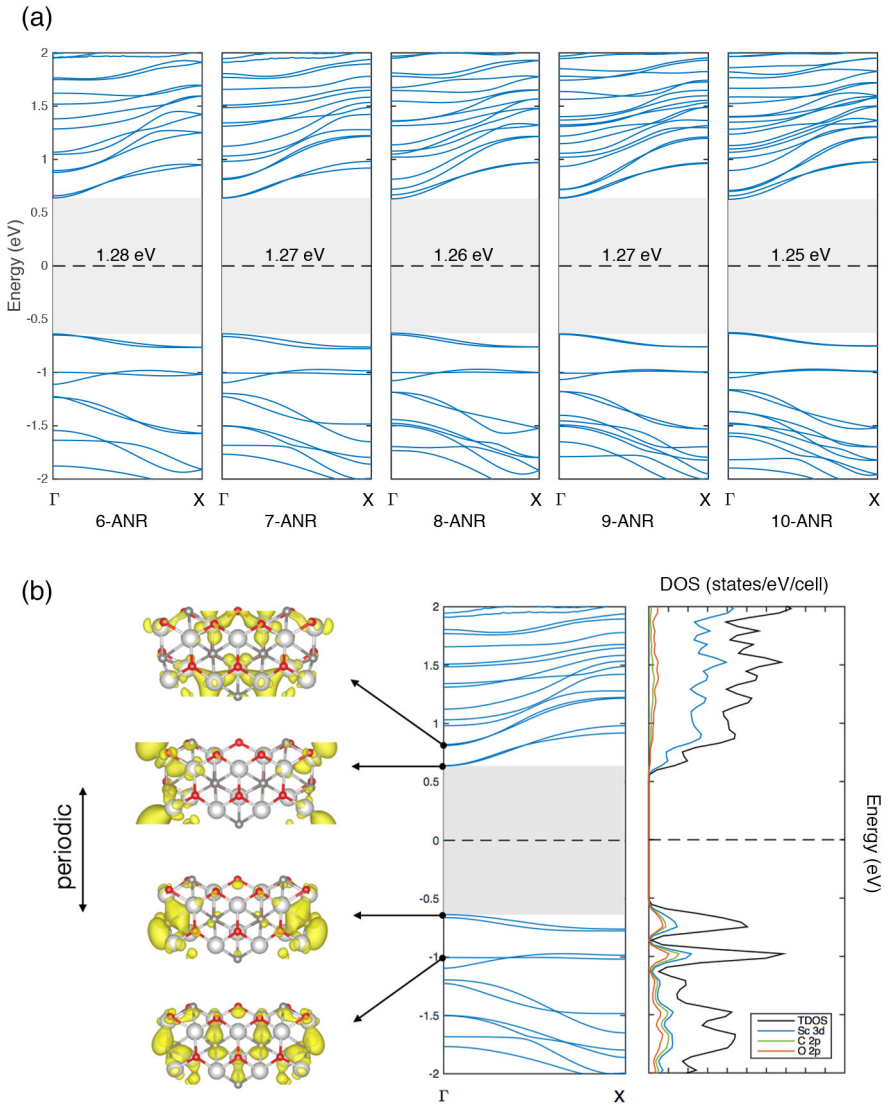

Figure 4.5.3. (a) Band structures of Sc_2CO_2 ANRs ($n_a = 6 - 10$). Fermi energy is shifted to zero and band gaps are highlighted by the shaded area with corresponding values. (b) Left panel: charge density isosurface (isovalue is set as 0.02 $e^-/\text{Å}^3$) for selected points in the band structure of Sc_2CO_2 7-ANR; Right panel: the corresponding total DOS and projected DOS on specific atomic orbitals.

The projected DOS of the six types of ZNR edges are plotted in Figure 4.5.2(c)–(h) to provide support for the EC rule explained above. In OScC, ScCO and ScOC edges, there are more Sc dangling bonds than the sum of C and O dangling bonds (i.e., $D_{\mathrm{Sc-C}} + D_{\mathrm{Sc-O}} > D_{\mathrm{C-Sc}} + D_{\mathrm{O-Sc}}$), which leads to Sc atoms not being fully ionized. Thus, the Fermi energy shifts upward compared to that in the 2D sheet, and there is a significant contribution to the DOS at the Fermi level due to these Sc $3d$ states as shown in Figure 4.5.2(d), (f) and (h). In CScO, OCSc and COSc edges, Sc dangling bonds cannot provide enough electrons to saturate the dangling bonds of the outermost C and O atoms (i.e., $D_{\mathrm{Sc-C}} + D_{\mathrm{Sc-O}} < D_{\mathrm{C-Sc}} + D_{\mathrm{O-Sc}}$). As shown in Figure 4.5.2(c), (e) and (g), there are strong signals of C $2p$-Sc $3d$ and O $2p$-Sc $3d$ hybridization around Fermi level due to the dangling states in the C and O atoms.

4.6 Summary

In this chapter, I study the size and edge dependent properties of Ti_2CO_2 and Sc_2CO_2 MXene nanoribbons using first-principles DFT calculations. Armchair and zigzag edge-shaped nanoribbons are constructed from the semiconducting MXenes without hydrogen passivation at the edges. All the ANRs are found to be semiconductors while most of the ZNRs are metals. The semiconducting/metallic nature of the nanoribbons is explained by an electron counting rule, where if all the dangling bonds in both edges can be saturated, then the system remains semiconducting as its 2D counterpart; otherwise, the system becomes metallic due to extra states generated at Fermi level. The lowest energy structural model plays an important role in determining the structural and electronic properties of the nanoribbons. In nanoribbons corresponding to Model I structure, e.g. Ti_2CO_2, two types of ANRs and six types of ZNRs are

defined according to their edge types. The band gap evolution as a function of the ribbon size of the ANRs exhibits significant even-odd oscillations at small sizes, but the gaps converge to that of the 2D sheet at large sizes. One of the six types of ZNRs which has two semiconducting edges, remains as a semiconductor, while other five types which have at least one metallic edge are metals. Appreciable transition metal *d*-*d* hybridization is observed in some Model I nanoribbons, which reduces the band gap by generating a flat band right above the VBM. In nanoribbons corresponding to Model III structure with two different surfaces, e.g. Sc_2CO_2, two types of ANRs and nine types of ZNRs are defined. The relaxed ANRs bend after relaxation to relieve the atomic concentration imbalance at the two surfaces, and the curvature decreases as ribbon size grows. The band gaps of Model III ANRs are nearly size-independent with values that are smaller than that of the 2D sheet, regardless of the ribbon size. The reduction in the band gap compared to the 2D sheet is due to appearance of strong edge states that form the new VBM and CBM. All of the nine types of ZNRs are metallic since none of the ZNR edges is semiconducting as predicted (and verified) by the electron counting rule. My results suggest that semiconducting versus metallic nature as well as the size of the band gap for semiconducting MXene nanoribbons can be tuned as a function of size, edge shape, and chemical composition, which can be useful for future designs of MXene nanostructures with interesting electronic and optical properties.

CHAPTER 5

LITHIUM COBALT OXIDE NANOPLATELETS

5.1 Introduction

Lithium cobalt oxide ($LiCoO_2$) is the most widely used cathode material for Li-ion batteries. In recent years, nanosized (< 50 nm) $LiCoO_2$ has attracted extensive investigations owing to its great improvement in charge/discharge-rate capacity [134; 135]. It has been demonstrated that the physical properties, e.g. lattice parameters and magnetic susceptibility, of the nanosized $LiCoO_2$ significantly differ from those of bulk $LiCoO_2$ due to surface effects [136]. The presence of large electrode-electrolyte interface areas might, on the other hand, increase the interfacial instability, which has been attributed to the electroactive transition metals present at the surface of the electrode [137]. Core-shell nanocrystal heterostructures offer opportunities for improving the stability and functionality of the electrode by introducing inactive ions to enable electrical insulation and provide passivation layer. This ability has been recently demonstrated with the compositional and structural tailoring of passivating layers based on Al_2O_3, grown conformally onto $LiCoO_2$ nanoplatelets, using thermal treatments by Hu *et al* [138]. Upon raising the annealing temperature, the interface is found to form $LiAl_xCo_{1-x}O_2$ gradient structure composed by an Al-rich outer layer on a Co-rich core, which presents significant improvement in electrochemical performance and dramatic electrode-electrolyte interface stabilization, compared to the bare $LiCoO_2$ nanoplatelets.

The surface energies of bare $LiCoO_2$ nanoplatelet were previously studied using first-principles density functional theory (DFT) calculations [139]. The nanoplatelet was predicted to consist of several low-index surfaces, including (001), (104), (012), and (110) surfaces. Furthermore, electronic spin state transition was found to occur on the $LiCoO_2$ nanoplatelet surfaces, where intermediate- and high-spin-state (IS and HS) Co^{3+} ions are present at (104) and (110) surfaces, respectively [140], in contrast to the low-spin-state (LS) Co^{3+} observed in bulk $LiCoO_2$. The DFT-predicted higher spin Co^{3+} at surfaces were then observed in magic-angle spinning nuclear magnetic resonance spectroscopy and electron energy-loss spectroscopy [140; 141]. However, a clear experimental demonstration of the $LiCoO_2$ surface fine structure is still absent due to the limitation of the energy resolution. Moreover, the atomic and electronic structures of the Al-doped $LiCoO_2$ surfaces, which are critical to achieve precise control of the physical and electrochemical properties of the nanoelectrode with desired functionality, have yet to be characterized and understood [142].

In this chapter, I perform a combined experimental and theoretical study to address the structural and electronic properties of the bare and Al-doped $LiCoO_2$ surfaces, using scanning transmission electron microscopy, X-ray diffraction, X-ray absorption spectroscopy, electron energy-loss spectroscopy and first-principles DFT modeling approaches. I show a prominent splitting of O K-edge prepeak resulting from the surface IS and/or HS Co^{3+}. The (104) surface with IS state Co^{3+}, which exhibits a strong in-plane feature of splitting in the hybridized Co $3d$-O $2p$ states, plays a predominant role in the electronic structure of $LiCoO_2$ nanoplatelets. Furthermore, Al doping on the $LiCoO_2$ nanoplatelets reduces the surface Co^{3+} IS/LS ratio,

resulting in the intensity change of O K-edge prepeaks. These results establish a fundamental understanding of the structure-property relationship in $LiCoO_2$ nanoplatelets and advance my ability to precisely tailor the surface properties to enhance the optimized stability and performance of the electrode material in Li-ion batteries.

5.2 Experimental Setup

The $LiCoO_2$ nanoplatelet samples are synthesized using a hydrothermal process introduced in Ref. [138]. Three samples are used for experiments in this work: 1) Bare $LiCoO_2$ nanoplatelets, marked as bare; 2) Al-doped $LiCoO_2$ nanoplatelets with surface Al/Co ratio of 2%, marked as 1Al; 3) Al-doped $LiCoO_2$ nanoplatelets with surface Al/Co ratio of 6%, marked as 3Al. The details of sample synthesis are presented in the Supplemental Materials.

The STEM images and EEL spectra are obtained using the aberration-corrected JEOL JEM-ARM200CF microscope operating at an acceleration voltage of 200 kV. The HAADF, LAADF and ABF images are acquired using a convergence semi-angle of 23 mrad, and a collection angle from 90 to 175 mrad for HAADF imaging, 40 to 90 mrad for LAADF imaging while 11 to 23 mrad for ABF imaging. EELS is collected using a convergence angle of 30 mrad and a collection angle with 35 mrad. Energy dispersions of 0.3 eV/channel is used for the measurement of the O K-edge spectrum.

Powder X-ray diffraction (XRD) patterns are collected on Bruker D8 Advanced X-ray Diffractometer. X-ray absorption spectroscopy (XAS) is conducted at the O K-edge and Co L-edge at beamline 4-ID-C at the Advanced Photon Source. Samples are loaded into the measurement chamber from an Ar-filled transfer stage, using an Ar-filled glove bag. To examine the

electronic properties at materials surface, the spectra are collected utilizing sample photocurrent for the total electron yield (TEY), which probes the surface of a material, at $\sim 10^{-9}$ Torr. Data are obtained at a spectral resolution of 0.2 eV with 2 sec dwell time. Three scans are performed on each sample, at each absorption edge, and scans are averaged in order to maximize the signal-to-noise ratio. An energy reference for Co and O is recorded simultaneously with the XAS for accurate energy alignment.

5.3 Computational Setup

First-principles DFT calculations are carried out using the GGA with the Hubbard U correction (GGA+U) method, as implemented in VASP. The effective U value for Co $3d$ electrons is chosen as $U - J = 3.3$ eV in accordance with the previous theoretical studies [139; 140]. All the calculations are performed using a plane wave cutoff of 550 eV. Slab models with two symmetric surfaces separated by a vacuum of 20 Å are used to simulate the $LiCoO_2$ surfaces. $8 \times 4 \times 1$ and $16 \times 8 \times 1$ Monkhorst-Pack k-point grids are used for geometry optimization and DOS calculations, respectively. Two polar surfaces, (001) and (012), and two nonpolar surfaces, (104), and (110), are considered in this work. For the polar (001) and (012) surfaces, 0.5 monolayer of Li and O are considered as the terminations, respectively, to compensate the dipoles in the slabs [139; 143]. All the slabs are therefore stoichiometric with the chemical formula of $(LiCoO_2)_n$. I find that $n = 12$, corresponding to the slab thickness of ~ 20 Å, is enough to simulate the surface properties. The surface models are shown in Figure 5.3.1.

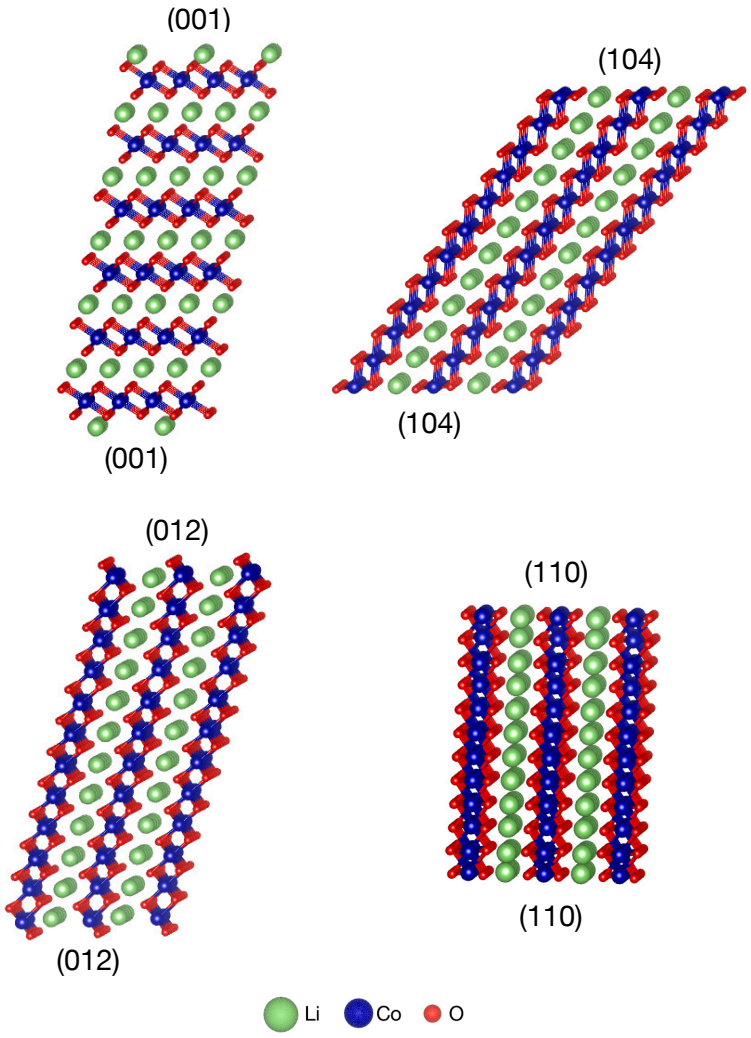

Figure 5.3.1. The slab models (shown in the extended unit cells) for simulating the (001), (104), (012) and (110) surfaces. (001) and (012) are polar surfaces, while (104) and (110) are nonpolar surfaces. The top and bottom surfaces in a slab are symmetric and separated by a vacuum of 20 Å (not shown in the figure).

The surface energy γ for the slab model with chemical formula of $(LiAl_xCo_{1-x}O_2)_n$ is calculated using the following equation:

$$\gamma = \frac{1}{2A}[E_{\text{slab}} - n(1-x)E_{LiCoO_2} - nxE_{LiAlO_2}], \tag{5.1}$$

where E_{slab} is the DFT total energy of the slab model, E_{LiCoO_2} is the energy of bulk $LiCoO_2$, E_{LiAlO_2} is the energy of bulk $LiAlO_2$, and A is the surface area in the unit cell.

5.4 Bare $LiCoO_2$ Nanoplatelets

The equilibrium shape of bare $LiCoO_2$ single particle observed from the STEM images, shown in Figure 5.4.1(a), consists of (001), (104) and (012) surfaces, among which (001) possesses the largest surface area. From the LAADF image at low magnification, shown in Figure 5.4.1(b), I can see that the nanoplatelets prefer to stack along the [001] direction, which largely reduces the exposed area of (001) surface in the nanoplatelets. The atomic structures of (001), (104) and (012) surfaces in the $LiCoO_2$ nanoplatelet can be directly observed through atomic-resolution HAADF imaging, which minimizes the thickness effect at the particle edges, along [010] and $[42\bar{1}]$ zone directions shown in Figure 5.4.1(c) and (d), respectively. The three surfaces are atomically sharp without significant structural changes compared with the bulk area. The atomic structure is further characterized from the near-edge area using atomic-resolution ABF imaging, which enables the observation of O columns, shown in Figure 5.4.1(e) and (f). It can be seen that the STEM-resolved $LiCoO_2$ structure is in good agreement with the DFT-optimized structure in terms of the lattice spacing, surface orientation and elemental arrangement, providing validation for the structural models used in the DFT simulation.

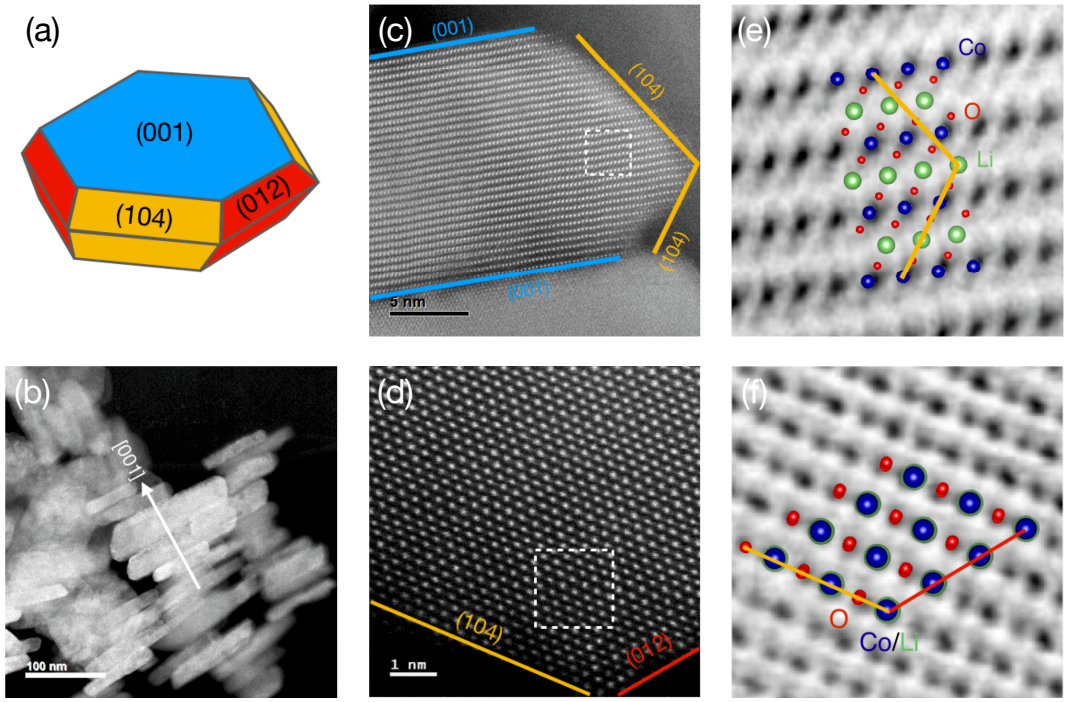

Figure 5.4.1. (a) The shape of $LiCoO_2$ nanoplatelet with (001), (104) and (012) surfaces represented by blue, yellow and red colors, respectively. (b) STEM-LAADF image at low magnification. (c) Atomic-resolution STEM-HAADF image along [010] with (001) and (104) surfaces marked. (d) Atomic-resolution STEM-HAADF image along $[42\bar{1}]$ with (104) and (012) surfaces marked. (e) Atomic-resolution STEM-ABF image taken from the dashed square area in (c). The DFT-optimized structure along [010] is illustrated as inset with (104) surface marked. (f) Atomic-resolution STEM-ABF image taken from the dashed square area in (d). The DFT-optimized structure along $[42\bar{1}]$ is illustrated as inset with (104) and (012) surfaces marked. The Li, Co and O atoms are represented by green, indigo and red balls, respectively.

The ELNES and X-ray absorption near-edge structure (XANES) at the O K-edge are measured using EELS in point mode and XAS in TEY mode, respectively, as shown in Figure 5.4.2. Except for peak B at 537 eV and peak C at 543 eV, which are associated with the hybridization of O $2p$ and Co $4sp$ states, the O K-edge prepeak at around 531 eV, originating from the hybridization of O $2p$ and Co $3d$ states, exhibits a significant difference between ELNES and XANES in terms of the peak splitting. The ELNES shows a single prepeak A at 531 eV while the XANES shows two split prepeaks A_1 and A_2 at 530.6 eV and 532 eV, respectively, with the energy spacing $\Delta = 1.4$ eV. The minor peak A_3 at 535.2 eV is usually contributed by Li_2CO_3 [144], and will not be discussed in detail in this work. The difference between the ELNES and XANES suggests that the electronic structures at $LiCoO_2$ bulk and surface are significantly different. In the following discussion, I will focus on the two split O K-edge prepeaks A_1 and A_2 in $LiCoO_2$ nanoplatelets, which have not been reported in previous literature to the best of my knowledge.

The DFT-calculated properties for the bare $LiCoO_2$ surfaces are summarized in Table III. The relative stability of each surface can be indicated by the calculated surface energy γ. Among all the investigated surfaces, the nonpolar (104) surface is found to be the lowest-energy surface. The experimentally observed dominant (001) surface is the second lowest-energy surface from DFT calculations, because the Li-terminated (001) surface energy is more sensitive to the chemical potential of surface Li^+. The surface energy of (001) can decrease significantly from about 1 J/m^2 to 0.4 J/m^2 as the Li chemical potential is lowered by increasing the

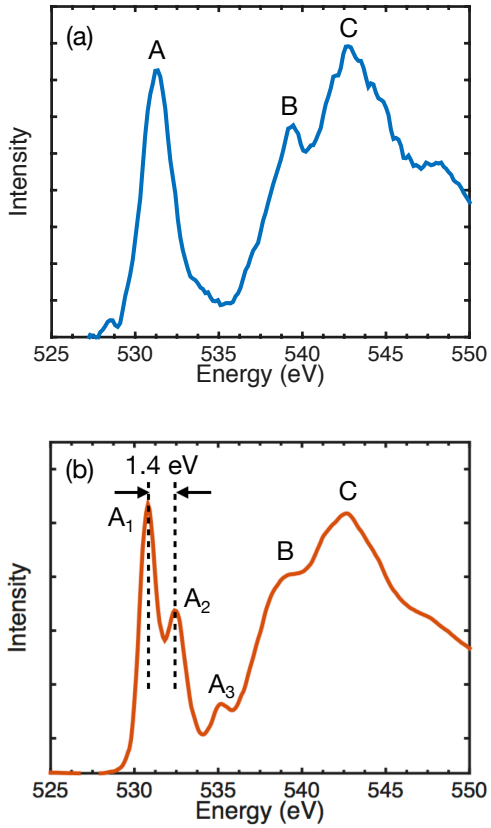

Figure 5.4.2. (a) ELNES at O K-edge for the bare $LiCoO_2$ nanoplatelets. Three characteristic peaks are labeled as A, B and C. (b) XANES at O K-edge for the bare $LiCoO_2$ nanoplatelets. The characteristic peaks are labeled as A_1, A_2, A_3, B and C.

voltage. Similarly, the polar O-terminated (012) surface energy can also be lowered to the value comparable to the (104) surface under O-rich condition [139].

According to the calculated projected DOS on Co 3d t_{2g} and e_g orbitals, the surface Co presents different spin state on different surfaces due to the altered Co coordination. The 6-fold coordinated Co^{3+} ions in the polar (001) surface are in the low spin state (LS, $t_{2g}^6 e_g^0$), the 5-fold

TABLE III

DFT CALCULATED $LiCoO_2$ SURFACE PROPERTIES: LATTICE CONSTANT a AND b, SURFACE Co COORDINATION, AND SURFACE ENERGY γ.

surface	polarity	a (Å)	b (Å)	$\angle(a,b)$ (deg)	Co coord.	γ (J/m^2)
(001)	polar	2.832	5.663	60.0	6	1.040
(012)	polar	2.832	4.987	90.0	5	1.652
(104)	nonpolar	2.832	6.396	63.7	5	0.791
(110)	nonpolar	4.987	4.904	70.9	4	1.532

Co^{3+} ions in the polar (012) and nonpolar (104) surfaces are in the intermediate spin state (IS, $t_{2g}^5 e_g^1$), while the 4-fold Co^{3+} ions in the nonpolar (110) surface is in the high spin state (HS, $t_{2g}^4 e_g^2$). The spin-resolved projected DOS on Co $3d$ (t_{2g} and e_g) and O $2p$ orbitals are plotted for bulk $LiCoO_2$, (001), (104) and (110) surfaces in Figure 5.4.3. The DOS profile for polar (001) surface is similar to that of bulk $LiCoO_2$, where the Co t_{2g} orbital is fully occupied while the e_g orbital is empty, lying 2 eV above the Fermi level. The characteristic O peak A at 2 eV above the Fermi level, originating from the hybridization with Co e_g orbital, corresponds to the O K-edge prepeak A in the ELNES. Compared with the DOS in the bulk, the unoccupied Co e_g orbital in the (104) surface splits into two components at 0.8 eV (spin up) and 2.3 eV (spin down) above the Fermi level due to the partial occupancy of the e_g orbital. The unoccupied O $2p$ states, A_1 at 0.8 eV and A_2 at 2.3 eV, can be, therefore, attributed to the hybridization with the Co unoccupied e_g split states. The DOS profile for the (012) surface with IS Co^{3+} exhibits similar features as that for the (104) surface. In the DOS of (110) surface with HS Co^{3+}, the

unoccupied O $2p$ states A_1 at 0.8 eV can be attributed to the hybridization with the unoccupied Co t_{2g} states at 0.8 eV above the Fermi level, while the A_2 peak at 2.3 eV stems from the anti-bonding states with Co underneath the surface. These two distinct O states, A_1 and A_2, found in the (104), (012) and (110) surfaces from the DFT modeling reproduce the experimentally observed prepeak splitting in the XANES at O K-edge. Furthermore, the splitting energies from the DFT modeling (ΔE = 1.5 eV) and the XAS (Δ = 1.4 eV) are in good agreement. Similar splitting behavior of O K-edge prepeak has been reported in $Ca_3Co_4O_9$ thin films with HS Co^{4+} [145].

To further explore the O K-edge prepeak splitting, the orbital-projected DOS for the O atoms at (104) surface, which has the lowest surface energy, is illustrated with the surface model in Figure 5.4.4. As mentioned above, the surface 5-fold Co^{3+} ion is in the IS, while the 6-fold Co^{3+} ions underneath the surface are in the LS. The splitting behavior is only observed in the O p_x and p_y states (peak A_1 and A_2 in Figure 5.4.4b) from the surface layer, stemming from the in-plane IS Co-O bonding, which has a strong two-dimensional character. On the other hand, the O p_z states, stemming from the out-of-plane LS Co-O bonding, only contribute to peak A_2. In addition to the (104) surface, the (012) surface with IS Co^{3+} and (110) surface with HS Co^{3+} also contribute to the splitting of O K-edge prepeak as discussed previously. Therefore, the experimentally observed O K-edge prepeak splitting can be attributed to the presence of surface IS and/or HS Co^{3+}, and the intensity of peak A_1 is able to directly reflect the amount of surface IS and/or HS Co^{3+}. This explains the reason for the observation of O K-edge prepeak splitting in $LiCoO_2$ nanoplatelets, which possess large surface areas.

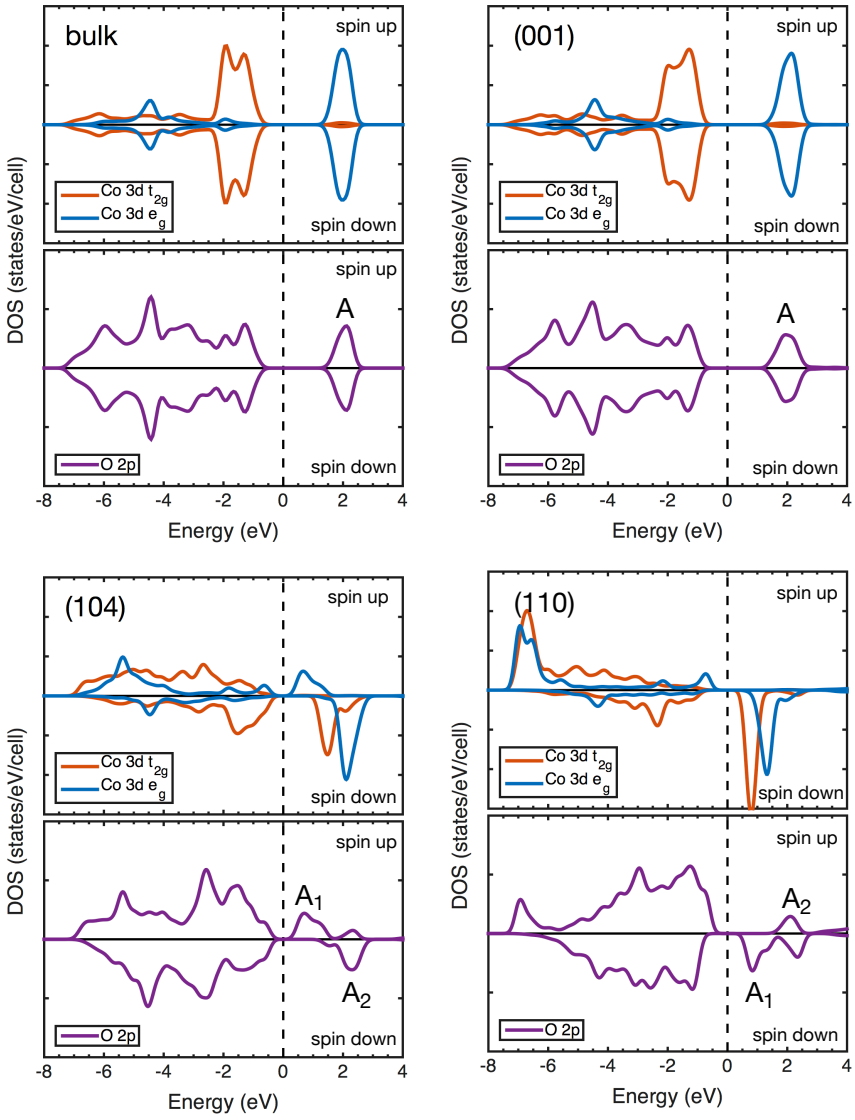

Figure 5.4.3. The spin-resolved projected DOS on Co $3d$ and O $2p$ orbitals for the $LiCoO_2$ bulk, (001), (104), and (110) surfaces. The characteristic peaks are marked by A, A_1 and A_2.

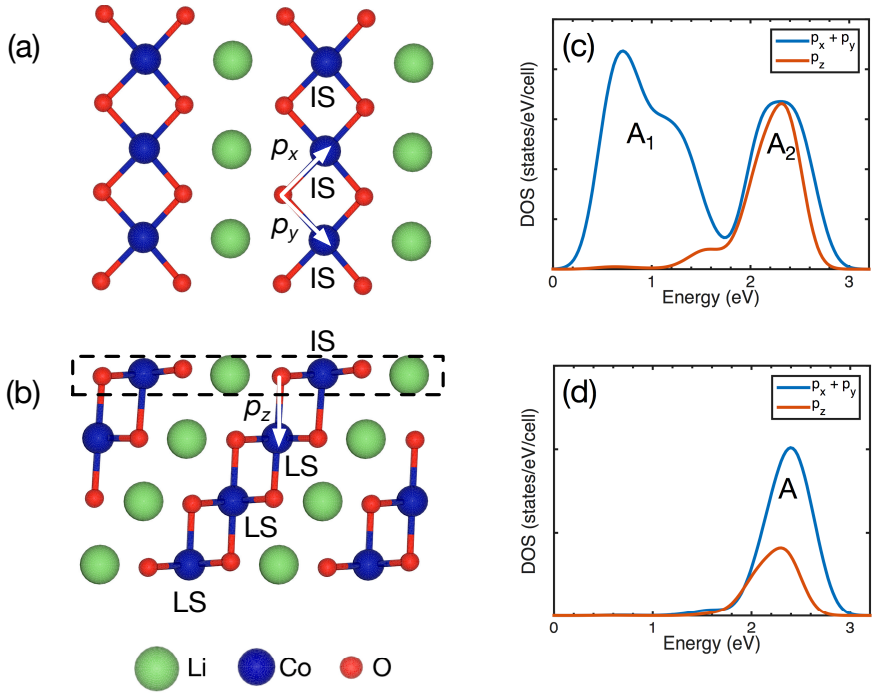

Figure 5.4.4. (a) Top view of the $LiCoO_2$ (104) surface structure with IS Co^{3+}. The directions of O p_x and p_y states are marked by white arrows. (b) Side view of the $LiCoO_2$ (104) surface structure with IS and LS Co^{3+} in different layers. The direction of O p_z state is marked by white arrow and the surface layer is marked by the dashed rectangles. (c) The DOS (summed spin-up and spin-down states) of in-plane ($p_x + p_y$) and out-of-plane (p_z) O unoccupied states from the surface layer. The split peaks from in-plane states are marked by A_1 and A_2. (d) The DOS (summed spin-up and spin-down states) of in-plane ($p_x + p_y$) and out-of-plane (p_z) O unoccupied states from the layer underneath the surface. The peak from in-plane states is marked by A.

5.5 Al-Doped $LiCoO_2$ Nanoplatelets

The effects of Al doping on the $LiCoO_2$ surface properties are studied using bare $LiCoO_2$ nanoplatelets coated with Al_2O_3 amorphous films at annealing temperatures of 400°C, 500°C, and 600°C. Figure 5.5.1 shows the XRD patterns for the two Al-doped $LiCoO_2$ samples (1Al and 3Al) and the bare $LiCoO_2$ sample at different temperatures. The peaks shown in the bare sample correspond to the layered structure of the high temperature form of $LiCoO_2$, as demonstrated by the splitting of the (006)/(012) and (108)/(110) peaks [134; 146], without any visible impurities. This layered structure is preserved, in all cases, after introduction of Al into the sample. The zoom of the (003) reflection reveals the gradually shift to lower angles for 3Al sample as the temperature increasing from 500°C to 600°C; however, no shift can be observed at 400°C for both 1Al and 3Al samples. This indicates that the introduction of Al does not influence the structure of $LiCoO_2$ as amorphous films at 400°C, but Al may react with $LiCoO_2$, forming $LiAl_xCo_{1-x}O_2$ and resultant Co_3O_4, as indicated by the distinct (220) and (311) peaks in the case of 3Al sample at 600°C [138]. However, such transformation cannot be detected in the 1Al sample at 600°C from XRD due to not enough Al contents in the sample.

Figure 5.5.2 shows the O K-edge XANES for the 1Al and 3Al samples at annealing temperatures of 400°C, 500°C, and 600°C. Both 1Al and 3Al samples at 400°C show the peaks with similar intensity profile compared with the bare $LiCoO_2$, suggesting that the local chemical environment of Co does not change with the increase of Al concentration at 400°C. Therefore, in the $Al_2O_3/LiCoO_2$ core-shell structure, the O K-edge XANES is not affected by the amorphous Al_2O_3 films, consistent with the XRD results. As the annealing temperature increases

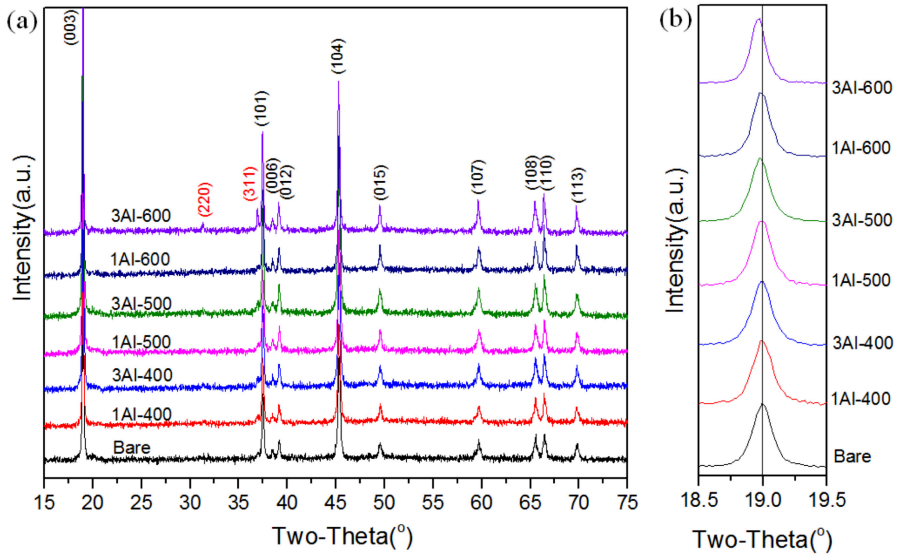

Figure 5.5.1. (a) XRD patterns of the samples. The bare sample is calcined at 500°C for 3 hours. Other samples are fabricated by the coating of bare $LiCoO_2$ nanoplatelets with different Al concentration (1Al, 3Al) and thermal treatment with different temperatures (400°C, 500°C, and 600°C) for 3 hours. Peaks (003), (101), (006), (012), (104), (015), (107), (108), (110), and (113) are indexed as $LiCoO_2$ for all samples, and peaks (220), (311) are indexed as Co_3O_4 in the 3Al sample at 600°C. (b) Zoom in plots of the $18.5° - 19.5°$.

from 400°C to 500°C and 600°C, the $LiAl_xCo_{1-x}O_2$ gradient structure starts to form with the Al diffusion from surface to the bulk. For the 1Al sample, the intensity of peak A_1 slightly decreases while that of peak A_2 slightly increases. However, for the 3Al sample, the intensity of peak A significantly decreases at higher temperature while that of peak A_2 increases, resulting in the reverse of A_1/A_2 intensity contrast. This change of O K-edge prepeaks suggests that the Al concentration has a significant effect on the electronic structure of the $LiAl_xCo_{1-x}O_2$ surface. In addition to the O K-edge fine structure, Co L_3- and L_2-edge XANES is measured

for the 1Al and 3Al samples at 400°C, 500°C and 600°C to detect the change of Co valence state during the annealing process, as shown in Figure 5.5.3. However, no visible peak shift or intensity change can be observed compared with the bare $LiCoO_2$. Therefore, the surface Co valence remains +3, as indicated by the L_3/L_2 intensity ratio, during the Al-doping process.

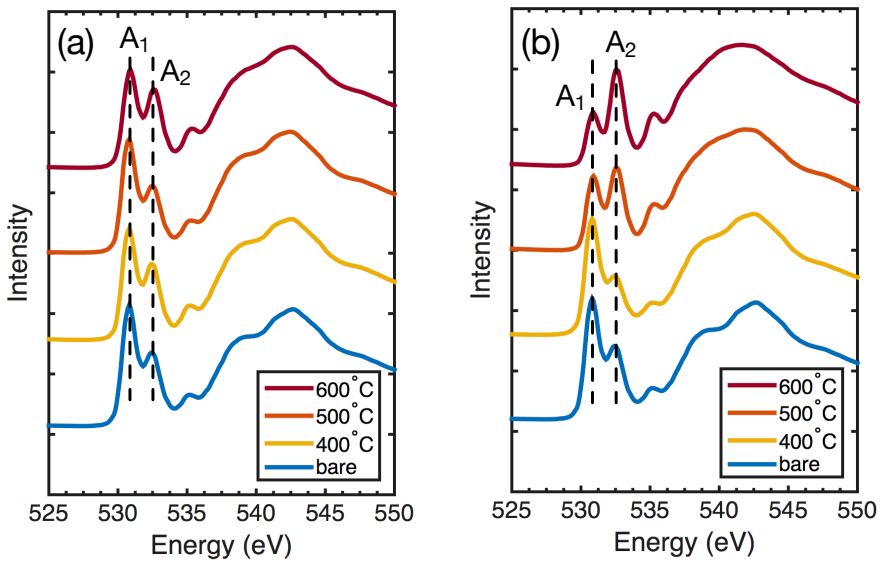

Figure 5.5.2. XANES at O K-edge for the two Al-doped $LiCoO_2$ samples, (a) 1Al and (b) 3Al, at temperatures of 400°C, 500°C and 600°C. XANES at O K-edge for the bare $LiCoO_2$ is shown for comparison. The split prepeaks are marked as A_1 and A_2.

The $LiAl_xCo_{1-x}O_2$ surfaces are simulated by replacing the surface Co with Al atoms in the extended 2×2 surface cell with Al concentration $x = 0.5$ and 0.25. In the optimized surface

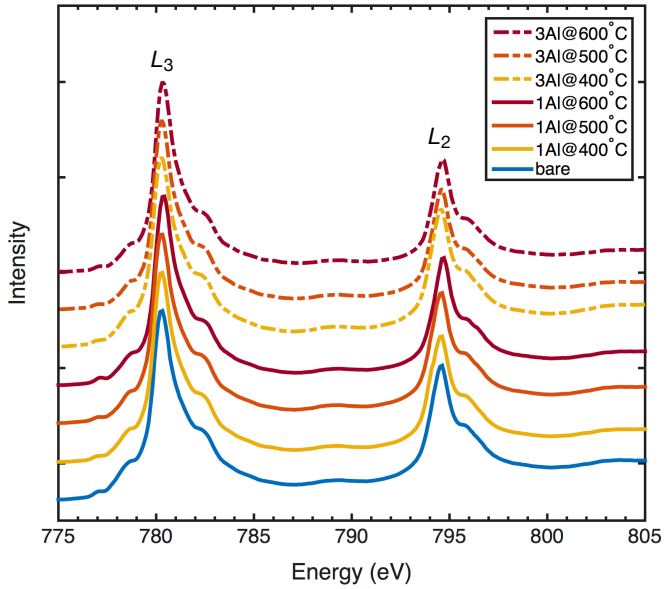

Figure 5.5.3. XANES at Co L_3 and L_2 edges for bare and Al-doped $LiCoO_2$ samples, 1Al and 3Al, at annealing temperatures of 400°C, 500°C and 600°C.

structures, shown in the Figure 5.5.4, the difference between Al-O and Co-O bond length is found to be less than 0.05 Å, and no significant surface reconstruction is observed. As shown in Table IV, the surface energy of the Al-doped (001) surface barely changes while that of the Al-doped (104) surface slightly lowers. The surface energy of (012) and (110) increases after Al doping at $x = 0.5$, suggesting that the (012) and (110) surfaces might be less favorable for Al doping than the (001) and (104) surfaces.

The effect of Al doping on the surface electronic structure is further explored through the projected DOS on O unoccupied $2p$ orbitals for the (104) surface, as shown in Figure 5.5.5. In both Al-doped cases, compared with the bare $LiCoO_2$ (104) surface, the in-plane O $2p$ states

TABLE IV

DFT CALCULATED $LiAl_xCo_{1-x}O_2$ ($x = 0.5, 0.25$) SURFACE ENERGY γ AND SURFACE ENERGY DIFFERENCE $\Delta\gamma$ BETWEEN Al-DOPED AND BARE $LiCoO_2$.

surface	x	γ (J/m^2)	$\Delta\gamma$ (J/m^2)
(001)	0.5	1.049	0.010
(001)	0.25	1.035	-0.005
(104)	0.5	0.760	-0.032
(104)	0.25	0.764	-0.027
(012)	0.5	1.805	0.153
(110)	0.5	1.702	0.169

($p_x + p_y$) remain split into two peaks A_1 and A_2 above the Fermi level, while the out-of-plane O $2p$ states (p_z) slightly shift to lower energy due to the tilting of the out-of-plane Co-O bonds. As the Al concentration x increases from 0.25 to 0.5, the intensities of both A_1 and A_2 peaks reduces compared to that of the out-of-plane states, since the number of the in-plane IS Co-O bonds reduces as more surface IS Co is substituted by Al, while the number of the out-of-plane LS Co-O remains the same. Furthermore, the effect of Al substitution of LS Co is also examined in the layers underneath the (104) surface as well as in the (001) surface. No significant change is found in the DOS of O $2p$ orbitals after Al doping except the decreased intensity of the single peak A, as shown in Figure 5.5.6. Therefore, the experimentally observed decrease in the A_1/A_2 intensity ratio as Al concentration increases at higher temperature can be attributed to the decreased surface Co^{3+} IS/LS ratio. In the case of 3Al sample at 600°C, the intensity of

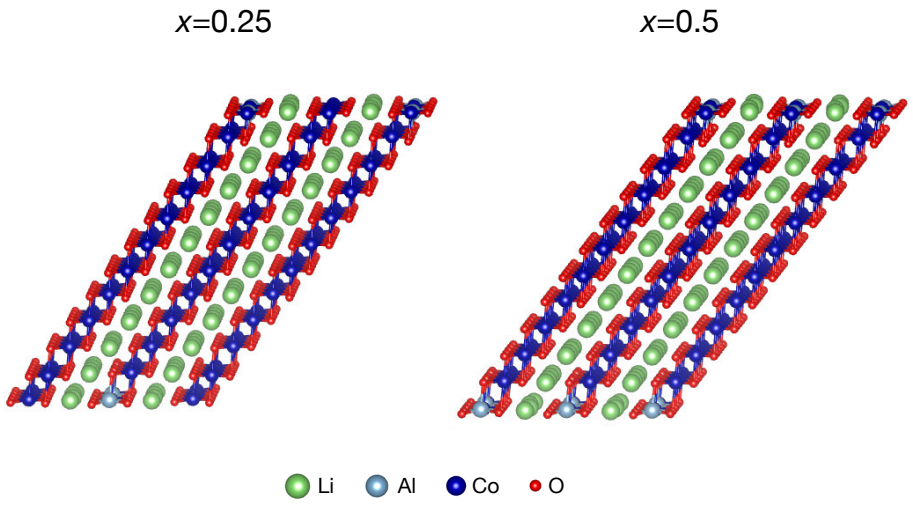

Figure 5.5.4. The DFT-optimized structures (show in the extended unit cells) for the Al-doped (104) surfaces with Al concentration $x = 0.25$ and 0.5.

peak A_1 is significantly suppressed while the intensity of peak A_2 increases accordingly as more LS Co^{3+} exposed to the surface.

5.6 Summary

Combining the experimental and theoretical results, I observe that the $LiCoO_2$ nanoplatelet mainly consists of atomically sharp (001), (104) and (012) surfaces, and the surface electronic properties of the $LiCoO_2$ nanoplatelet are significantly different from bulk $LiCoO_2$. From the comparison of EELS and XAS measurement of O K-edge fine structure, I find that the O K-edge prepeak splits into two prominent subpeaks A_1 and A_2 with energy spacing of 1.4 eV due to surface effects. The DFT simulation results indicate that the splitting behavior of O K-edge prepeak originates from the IS and/or HS Co^{3+} at different surfaces due to altered

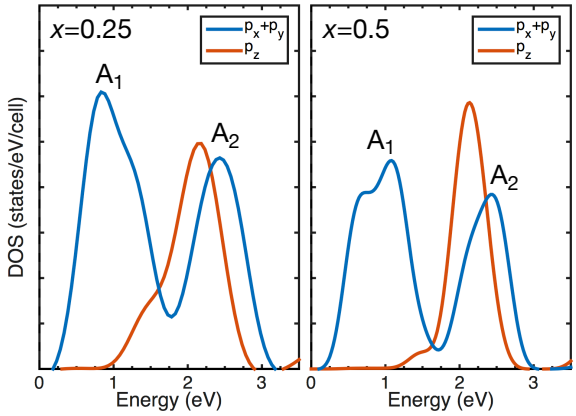

Figure 5.5.5. The DOS (summed spin-up and spin-down states) of in-plane ($p_x + p_y$) and out-of-plane (p_z) O unoccupied states at $LiAl_xCo_{1-x}O_2$ (104) surfaces, where $x = 0.25$ and 0.5. The split peaks from in-plane states are marked by A_1 and A_2.

Co coordinations. From the projected DOS of Co and O at (104) surface, which is predicted as the lowest-energy surface, I find that the splitting of the Co 3*d*-O 2*p* hybridized states is only contributed by the in-plane IS Co-O bonding that has a strong two-dimensional character. Therefore, the splitting behavior of O *K*-edge prepeak can be observed in $LiCoO_2$ nanoplatelets that have large surface areas. Furthermore, the intensity of peak A_1 can directly reflect the amount of surface IS and/or HS Co^{3+}, while the intensity of peak A_2 is associated with the amount of surface LS Co^{3+}.

The introduction of Al into $LiCoO_2$ nanoplatelets leads to the growth of Al_2O_3 films on the $LiCoO_2$ surface, forming $LiCoO_2/Al_2O_3$ core-shell structure. As the annealing temperature raises from 400°C to 600°C, Al_2O_3 shell crystallized and Al diffuses into the core, forming $LiAl_xCo_{1-x}O_2$ gradient structure with higher x at the surface than the bulk. The XAS mea-

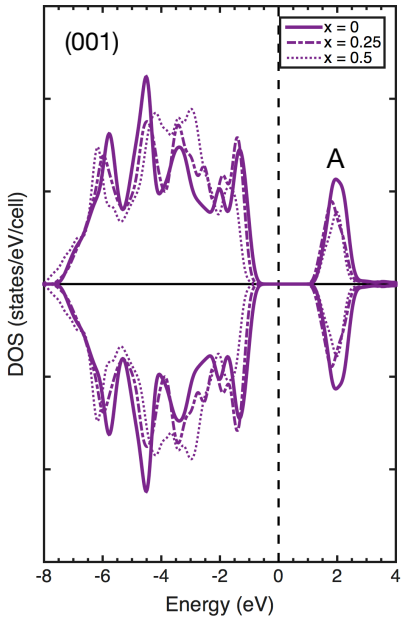

Figure 5.5.6. The spin-resolved projected DOS on O $2p$ orbitals for the bare (Al concentration $x = 0$) and Al-doped $LiCoO_2$ (001) surfaces with Al concentration $x = 0.25$ and 0.5. The characteristic peak is marked by A.

surement indicates that, during the annealing process, the Co valence remains 3+, while the intensity ratio of O K-edge prepeaks A_1/A_2 decreases as the surface Al concentration increases. As suggested by the DFT modeling results, the effect of Al doping is to reduce the surface Co^{3+} IS/LS ratio, resulting in the decrease of the A_1/A_2 intensity ratio at O K-edge. My work illustrates that the magnetic properties of $LiCoO_2$ nanoplatelets can be tailored by controlling the surface structures and compositions at the atomic level, providing the opportunities for designing and developing novel Li-ion battery materials with higher stability and better performance.

CHAPTER 6

BARIUM TITANATE NANOCUBES

6.1 Introduction

Nanoscale perovskite ferroelectrics continue to be of great scientific interest due to their potential applications in nanoscale memory devices with ultrahigh storage density. Earlier studies have demonstrated the size dependence of the Curie temperature, i.e. the temperature at which the ferroelectric-paraelectric transition occurs, in lead titanate ($PbTiO_3$) and barium titanate ($BaTiO_3$) nanoparticles [147; 148]. Recent studies suggested that small $BaTiO_3$ particles are metrically more cubic, as a consequence of reduced dipole-dipole correlations, while retaining tetragonal distortion locally [149; 150; 151]. More recently, first-principles simulation work predicted unusual toroidal polarization patterns that can be stable in lead zirconate titanate ($Pb[Zr_xTi_{1-x}]O_3$) nanoparticles with sizes down to 3.2 nm [152]. However, understanding of the physical mechanisms and driving force responsible for the size-dependent ferroelectric behavior at finite dimensions is still unsettled, with possible mechanisms such as internal strains and depolarization fields existing in the nanostructures [153; 154]. In order to make progress in understanding the nature of polar ordering in nanoscale ferroelectrics, it is critical to use high-quality single-crystalline nanomaterials with well-defined sizes, shapes and surfaces, as well as advanced measurement techniques with ultrahigh precision.

$BaTiO_3$ is considered as a prototype of ferroelectric pervoskite oxides with Curie temperature very close to room temperature. Recently, aggregate-free cube-like single-crystalline $BaTiO_3$ colloidal nanoparticles (also known as nanocubes) with well-defined sizes and shapes were synthesized using a simple phase transfer process at temperatures as low as 135°C [155]. Aberration-corrected TEM was then employed to directly map the ferroelectric structural distortion of these $BaTiO_3$ nanocubes at atomic scale. A nearly linear ferroelectric domain accompanied by local structural distortion was demonstrated in non-interacting nanocubes with size down to ~ 5 nm at room temperature [156]. In this chapter, I present results and analysis of studying the polar distortion patterns in single-crystalline $BaTiO_3$ nanocubes, with various sizes from 8 nm to 40 nm, using aberration-corrected STEM imaging with picometer precision. Quantitative analysis of the STEM images is performed using statistical and machine learning approaches for the purpose of mapping and calculating the ferroelectric structural distortion in each $BaTiO_3$ unit cell for the entire nanocube.

6.2 Experimental Setup

The single-crystalline $BaTiO_3$ nanocubes with controlled morphology and surface composition are synthesized under solvothermal conditions at temperatures as low as 180°C, as introduced in Ref. [157]. The shape of the nanocrystals can be tuned from spheroidal to cubic by changing the polarity of the solvent, while their size is varied from 16 to 30 nm for spheres and 5 to 78 nm for cubes upon changing the concentration of the precursors and the reaction time, respectively. TEM samples for $BaTiO_3$ nanocubes with sizes of 8 nm, 10 nm, 12 nm and 40 nm are prepared using copper grids with ultrathin (~ 5 nm) carbon film.

The STEM images are obtained using the aberration-corrected JEOL JEM-ARM200CF microscope operating at an acceleration voltage of 200 kV. The HAADF images are acquired using a convergence semi-angle of 23 mrad, and a collection angle from 68 to 175 mrad. In order to accurately map the polar distortion over the entire nanocube, the HAADF image should be able to resolve each atomic column (i.e. Ba or Ti column) with a reasonable pixel size. For 8-, 10- and 15-nm nanocubes, the atomic-resolution HAADF images are recorded at size of 512×512 with pixel size of 0.027 nm and pixel dwell time of 31 μs. For 40-nm nanocubes, the atomic-resolution HAADF images are integrated using 5 consecutively recorded images at size of 2048×2048 with pixel size of 0.02 nm and pixel dwell time of 5 μs. Cross correlation method is used to minimize sample drifting.

6.3 Polarization Mapping

The polarization $\mathbf{P}$ in a $BaTiO_3$ unit cell is calculated as

$$\mathbf{P} = \frac{e}{\Omega} \sum_s Z_s^{\text{ion}} \mathbf{R}_s, \tag{6.1}$$

where e is the elementary charge, Ω is the volume of the unit cell, Z_s and $\mathbf{R}_s$ are the ion charge and ion position for species s (s = Ba, Ti, and O), respectively. The direction of the polarization coincides with that of the displacement of the central Ti^{4+} ion in the unit cell, and the strength of the polarization is proportional to the magnitude of the displacement. In HAADF images, therefore, the polarization can be mapped by mapping the displacement of the Ti column (here I use Ti column to represent Ti+O mixed column since O cannot be resolved by HAADF imaging) with regard to the center of the unit cell.

The critical step for mapping the Ti displacement in the $BaTiO_3$ nanocubes is finding the position of each atomic column in the STEM-HAADF images. However, accurately mapping the position of each atomic column in particles with a large number of unit cells and complex shape is not straightforward. Here, I developed a numerical method based on statistics and machine learning to automatically and precisely map the polarization from HAADF images for $BaTiO_3$ nanocubes with various sizes.

The process of mapping the Ti displacement in $BaTiO_3$ (100) HAADF image is summarized in Figure 6.3.1. Firstly, the local intensity maxima in a HAADF image are found by comparing the intensity of neighboring pixels for each pixel in the image. Only one pixel maximum is reported for each atomic column, as shown in Figure 6.3.1(a). Secondly, the intensity profile of each atomic column is fitted to a 2D Gaussian function

$$I(x,y) = I_0 + A \cdot \exp\left\{-\left[\frac{(x-x_0)^2}{2\sigma_x^2} + \frac{(y-y_0)^2}{2\sigma_y^2}\right]\right\}, \tag{6.2}$$

where I_0 is the background intensity, A is the amplitude, x_0 and y_0 are the atomic positions, σ_x and σ_y are the x and y spreads of the peak, respectively. The position for each atomic column is optimized using the nonlinear least-squares method with the position of the local intensity maximum as initial input. All atomic columns in the TEM image, marked by circles in Figure 6.3.1(b), are then described by a 2D Gaussian function with four parameters $G(x_0, y_0, A, \sigma)$, where σ is the average of σ_x and σ_y. The third step is to classify the Ba and Ti columns using the agglomerative clustering method with A and σ as features. The classification result is shown in Figure 6.3.1(c) by blue and red circles for Ba and Ti columns, respectively. Finally, the Ti

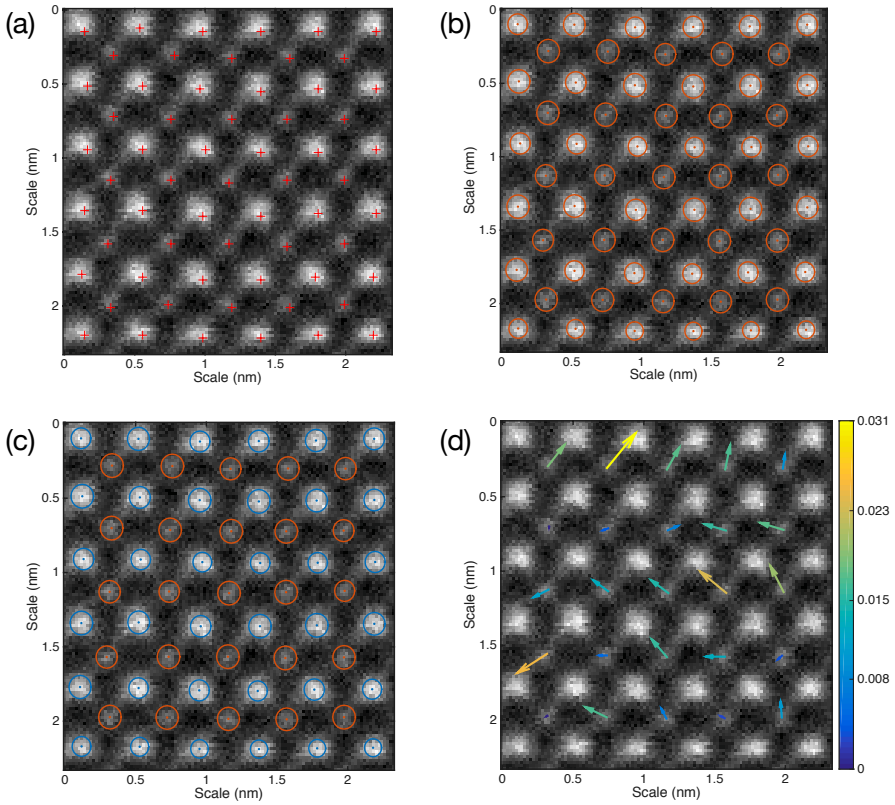

Figure 6.3.1. The process of mapping the Ti displacement in $BaTiO_3$ (100) HAADF image: (a) Find local maxima (marked by red +); (b) 2D Gaussian fitting (atomic columns are marked by red circles); (c) Classify Ba (blue circles) and Ti columns (red circles); (d) Map Ti displacement (marked by colored arrows).

displacement is calculated with regard to the center of the four-nearest-neighboring Ba columns, and mapped over the entire nanocube. The direction and magnitude of the displacement are indicated by arrows and color scale, respectively, as shown in Figure 6.3.1(d).

The statistically linear correlation r of the overall Ti displacement in a nanocube can be calculated as

$$r = \frac{||\langle \mathbf{d} \rangle||}{\langle ||\mathbf{d}|| \rangle}, \tag{6.3}$$

where $\langle ||\mathbf{d}|| \rangle$ is the average magnitude of local displacement $\mathbf{d}$, computed as

$$\langle ||\mathbf{d}|| \rangle = \frac{1}{N} \sum_{i}^{N} ||\mathbf{d}_i||_2, \tag{6.4}$$

and $||\langle \mathbf{d} \rangle||$ is the magnitude of the average displacement, computed as

$$||\langle \mathbf{d} \rangle|| = \left|\left| \frac{1}{N} \sum_{i}^{N} \mathbf{d}_i \right|\right|_2 . \tag{6.5}$$

$r = 0$ indicates no linear correlation, while $r = 1$ implies perfect linear correlation. The linear correlation in Figure 6.3.1 is calculated as $r = 0.604$.

6.4 Spontaneous Polarization in $BaTiO_3$ Nanocubes

The atomic-resolution HAADF images of $BaTiO_3$ nanocubes with sizes of 8 nm, 10 nm, 15 nm and 40 nm are shown in Figure 6.4.1. All the HAADF images are taken from freestanding single particles along the [100]-type direction. The smaller particles (8 nm and 10 nm) are more spherical with larger ratio of high-index surfaces (truncated cubes). As the particle size increases, the particle becomes more cubic with large areas of atomically sharp low-index surfaces. The polarization mapping for these nanocubes are then calculated using the HAADF images, as shown in Figure 6.4.2. The 8-nm, 15-nm and 40-nm nanocubes exhibit no clear polar distortion pattern as seen from the polarization mapping, whereas the Ti displacement is well ordered along the diagonal direction in the 10-nm nanocube. In addition, it is notable that

the polar distortion is significantly weaker at the surface than the central area in the 10-nm nanocube, suggesting the presence of a surface depolarization effect that passivates the surface polarization, which has been reported in Ref. [156]. However, this surface-induced effect is not prominent in the 15-nm and 40-nm nanocubes with lower ratio of high-index surfaces.

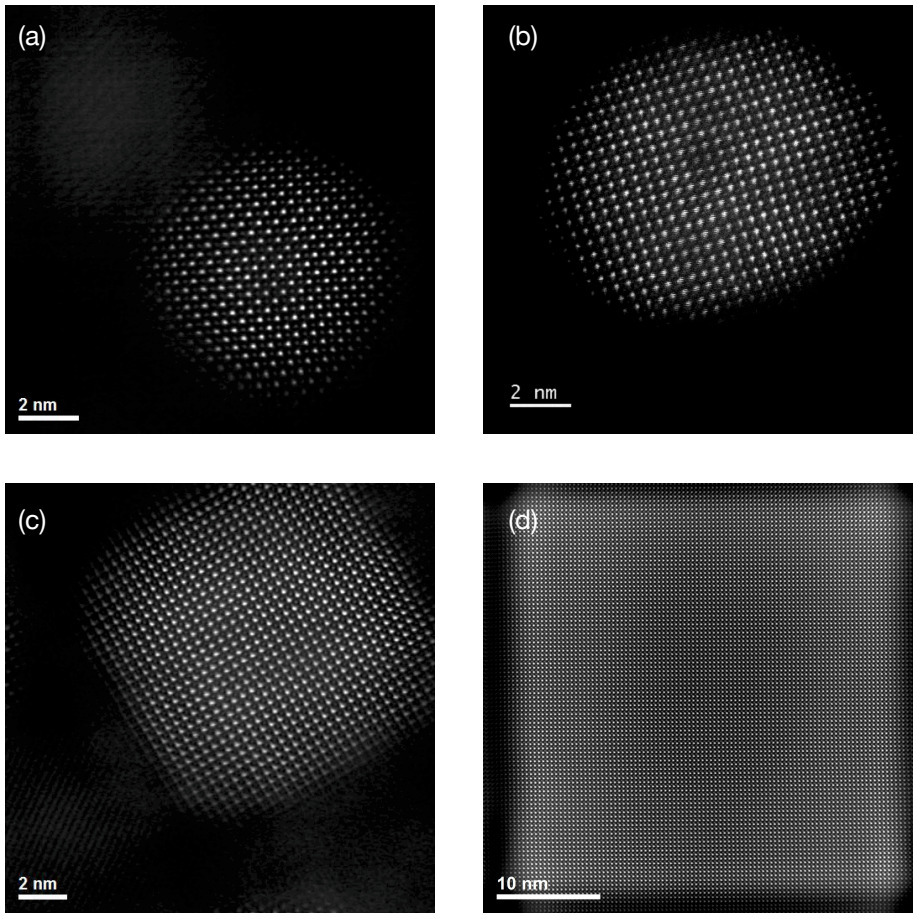

Figure 6.4.1. Atomic-resolution HAADF images of $BaTiO_3$ nanocubes with sizes of (a) 8 nm, (b) 10 nm, (c) 15 nm, and (d) 40 nm. The HAADF images are taken along the [100]-type direction and filtered using a fast Fourier transform filter.

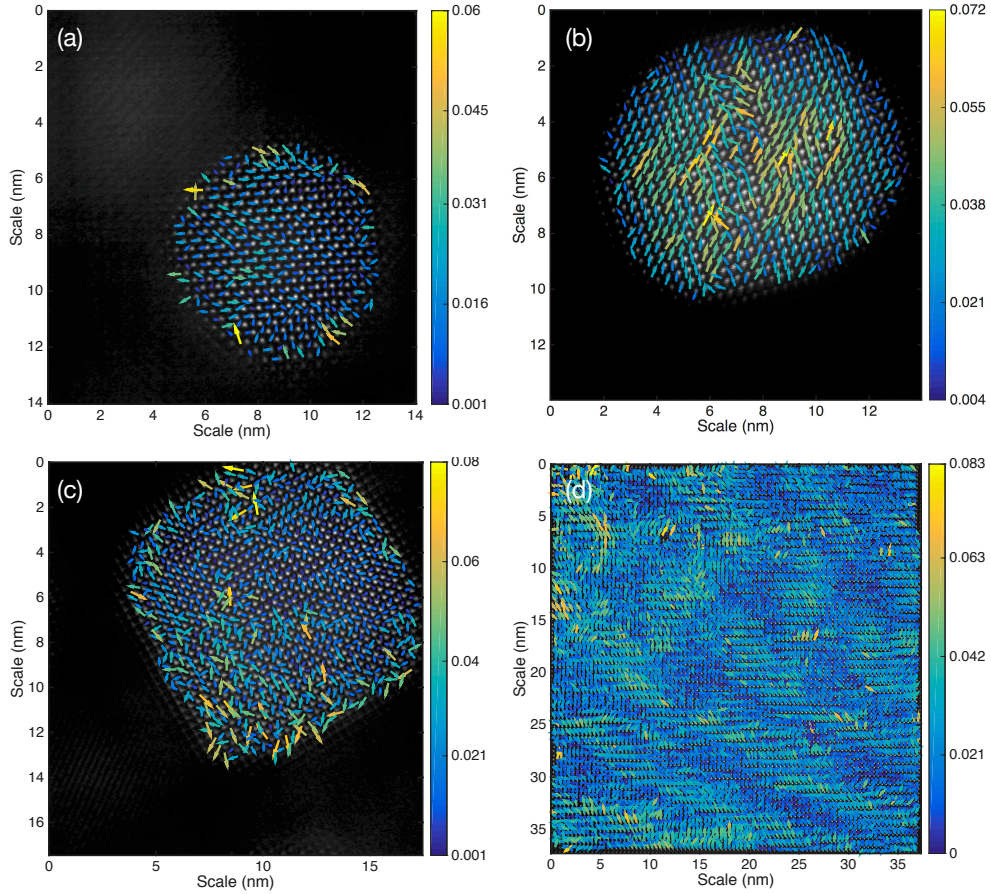

Figure 6.4.2. Polarization mapping of the $BaTiO_3$ nanocubes with sizes of (a) 8 nm, (b) 10 nm, (c) 15 nm, and (d) 40 nm.

The quantitative analysis results for the polarization patterns in these nanocubes are summarized in Table V. The average magnitude of local Ti displacement and the linear correlation generally tend to increase as the nanocube size increases; however, the polarization in the 10-nm nanocube exhibit a strong linear character ($r = 0.8957$). This indicates that the spontaneous

polarization pattern in $BaTiO_3$ nanocubes is not simply dependent on the particle size, but rather affected by a more complex effect of surface energetics and/or arrangement. Additionally, it is noteworthy that the average magnitude of the total Ti displacement in these nanocubes is smaller than the theoretical value in the bulk $BaTiO_3$, which is 0.35 Å [158], suggesting that the overall polar distortion is suppressed in the nanosized particles.

TABLE V

THE AVERAGE MAGNITUDE OF LOCAL Ti DISPLACEMENT $\langle||\mathbf{d}||\rangle$, MAGNITUDE OF THE AVERAGE DISPLACEMENT $||\langle\mathbf{d}\rangle||$, STANDARD DEVIATION OF LOCAL Ti DISPLACEMENT s AND LINEAR CORRELATION r MEASURED IN THE $BaTiO_3$ NANOCUBES.

size (nm)	$\langle\|\|\mathbf{d}\|\|\rangle$ (Å)	$\|\|\langle\mathbf{d}\rangle\|\|$ (Å)	s (Å)	r
8	0.150	0.059	0.095	0.3967
10	0.289	0.259	0.116	0.8957
15	0.198	0.084	0.129	0.4255
40	0.221	0.124	0.115	0.5597

6.5 Summary

In this chapter, the polarization patterns in $BaTiO_3$ nanocubes with various sizes are investigated to establish a fundamental understanding of the ferroelectric ordering in perovskite oxides down to their ultimate size limit, using atomic-resolution STEM-HAADF imaging and quantitative analysis. High-quality single-crystalline $BaTiO_3$ nanoparticles can be synthesized

with desired size and shape. Atomic-resolution HAADF imaging enables direct and picometer precise analysis of the displacement of Ti/O column in each $BaTiO_3$ unit cell. In addition, quantitative analysis based on statistics and machine learning provides a powerful means of mapping and analyzing the polarization pattern over the entire particle. Based on the analyses of the $BaTiO_3$ nanocubes with four sizes ranging from 8 nm to 40 nm along the [100]-type projection, it is found that, as the particle size increases, the shape of the nanocubes tends to be more cubic-like with large areas of atomically sharp low-index surfaces, and the polar distortion generally becomes more linearly ordered. In the 10-nm truncated nanocube with large ratio of high-index surfaces, the polar distortion reduces near the surface due to the surface depolarization effect. It is suggested that the spontaneous polarization patterns in these nanocubes are not simply dependent on their sizes, but rather significantly affected by a more complex effect rising from the surface energetics and/or arrangement. More experimental and theoretical studies, such as *in-situ* electrical STEM imaging, EELS mapping and first-principles DFT modeling, will be performed to further explore the surface and size effects on the ferroelectric ordering in perovskite oxide nanoparticles. These results provide useful insights into the fundamental nature of the ferroelectric properties in nanoscale oxides which have potential applications in designing and developing memory and storage devices at nanoscale.

CHAPTER 7

CONCLUSIONS AND OUTLOOK

7.1 Conclusions

In this Ph.D. dissertation, I investigated the atomic structures and electronic properties of several types of nanostructured transition-metal oxides with regard to their functionalities, using combined experimental and theoretical approaches. Aberration-corrected STEM imaging and EELS analysis were applied to directly probe the crystal structures, chemical compositions, and bonding states in thin films, nanoparticles, 1D and 2D materials. The heterointerfaces, surfaces, and defects in these nanostructures can be characterized and analyzed with sub-Angstrom (picometer) precision. First-principles DFT calculations were performed to further explore the atomic behavior in these materials by examining their ground-state structures and density of states.

Heterostructures of epitaxial $SrTiO_3$ and $BaTiO_3$ thin films with GaAs were studied with the focus on the heterointerface structures and the ferroelectric properties in oxide thin films. A thick layer of GaAs was deposited epitaxially on $SrTiO_3$ thin film using Si substrate. An atomically abrupt $SrTiO_3$/GaAs heterointerface with the interfacial configuration of O-deficient SrO layer in contact with As layer was observed using atomic-resolution STEM-EELS imaging. DFT modeling of various interfacial configurations confirmed the experimentally observed Sr/As interface structure and predicted another possible structure which is the SrO/Ga with interfacial

reconstruction of Ga-Ga dimers and Ga-O bonds. However, the oxidation of GaAs surface could happen prior to the epitaxial growth of $SrTiO_3$ thin film. O vacancies were found to be crucial to accommodate the interface polar discontinuity and form an abrupt interface. 2DEG was predicted to present at the $SrTiO_3$/GaAs interface, originating from the localized Ti $3d$ conduction band states pinned at the Fermi level. It is also predicted that the 2DEG can be enhanced by interfacial O vacancies, and relieved from the Fermi level through creating Ga or As vacancies at the interface. An example of the application of the $SrTiO_3$/GaAs platform is the epitaxial integration of $BaTiO_3$ thin film on the GaAs substrate with an ultrathin $SrTiO_3$ nucleation layer, which is capable of coupling the ferroelectricity in oxide thin films with the properties of semiconductor. Single-domain polarization along the out-of-plane direction in $BaTiO_3$ thin film is found to be induced by the $SrTiO_3$/GaAs interface. Ferroelectric switching in the $BaTiO_3$ thin film under external biases was directly observed through the *in-situ* atomic-resolution STEM-EELS imaging with a dedicated electrical chip.

O-functionalized MXene nanoribbons were studied using Ti_2CO_2 and Sc_2CO_2 nanoribbons as prototypes. The 1D nanoribbons were well classified by their edge types (armchair versus zigzag), the composition and sequencing of the terminating atomic lines, and the lowest-energy structural models of their 2D counterparts. DFT calculations were performed to find the edge- and size-dependent properties of the MXene nanoribbons. The semiconducting versus metallic nature of the nanoribbons was successfully explained using a simple electron counting rule for the edge dangling bonds. For semiconducting nanoribbons, the band-gap evolution as a function of ribbon size exhibited strong dependence on the lowest-energy structural model, and a

combination of factors such as quantum confinement, the energetic location of the edge states, and the strength of the transition-metal *d*-*d* hybridization. MXene nanoribbons with asymmetric O functional surfaces were found to have bent ground-state structures with curvatures increasing as the size of the ribbon decreases.

Surface properties of bare and Al-doped $LiCoO_2$ nanoplatelets were studied using combined experimental and theoretical approaches. The surface electronic properties of $LiCoO_2$ nanoplatelets were found to be significantly different from those of bulk $LiCoO_2$ due to altered spin states of surface Co^{3+} atoms. A prominent splitting of O K-edge prepeak was observed from X-ray absorption spectra and was attributed to the presence of intermediate- and/or high-spin-state Co^{3+} at the surface. The nonpolar (104) surface with intermediate spin state Co^{3+} was found to exhibit a strong 2D character of splitting in the hybridized Co $3d$-O $2p$ states, while the polar (001) surface with low- spin-state Co^{3+} was observed to possess a similar electronic structure as bulk $LiCoO_2$. Al doping on the $LiCoO_2$ nanoplatelets was achieved through thermal annealing with Al_2O_3 thin films. It was found that, as Al concentration increases, the ratio of low-spin-state Co^{3+} increases accordingly, resulting in a distinct change in the intensity ratio of the O K-edge split prepeaks.

Single-crystalline $BaTiO_3$ nanocubes were synthesized to study the polarization patterns in ferroelectric oxides down to the ultimate size limit. Atomic-resolution STEM imaging combined with quantitative image analysis was applied to directly map and analyze the local polar distortion over the entire nanocube. It was found that, as the particle size increases, the shape of the nanocubes tends to have larger areas of atomically sharp low-index surfaces, and the polar

distortion generally becomes more linearly ordered. In nanocubes with size down to 10 nm, the high-index surfaces become energetically more stable and a surface depolarization effect was observed. It was suggested that the spontaneous polarization patterns in the nanocubes are not simply dependent on their sizes, but rather significantly affected by a more complex effect rising from the surface energetics and/or arrangement.

In summary, my studies on the atomic-scale structural and electronic properties of $SrTiO_3$, $BaTiO_3$, Ti_2CO_2, Sc_2CO_2 and $LiCoO_2$ nanosturctures revealed the importance of the structural confinement, atomic arrangement and bonding states between transition-metal and oxygen atoms to the physical properties of oxide materials. The complexity of the transition-metal *d*-orbitals increases the difficulty in studying these materials, on the other hand, it offers great opportunities to discover novel functionalities through structural tailoring of the materials. A fundamental understanding of the structure-property relationship in these oxide nanomaterials greatly advances our ability to design and develop novel devices at nanoscale.

7.2 Outlook

The main goal of future work is to complete the research started in this dissertation and to further study the structure-property relationship of oxide nanomaterials using advanced atomic-scale analysis.

For $SrTiO_3$/GaAs heterointerfaces, the DFT-predicted SrO/Ga interface structure has not been directly observed in experiments. Although the surface of GaAs can be easily oxidized under O-rich condition, it is possible to integrate an abrupt SrO/Ga interface via carefully controlling the O content during the growth process. Interfacial defects, such as terrace struc-

ture at $SrTiO_3$ surface and antiphase boundaries in $SrTiO_3$ and GaAs, were observed from STEM imaging but were not discussed in detail in this dissertation. The distorted interface structures due to these defects will be of interest in future work. Furthermore, it is essential to validate the theoretically predicted 2DEG and Fermi-level unpinning in dedicated experiments. In my *in-situ* electrical experiment of the $BaTiO_3$ thin film, the contrast of the $SrTiO_3$/GaAs interface significantly reduced, which might be attributed to the damage from electrical heat accumulated at the interface. Therefore, it is critical to carefully connect the thin film to the electrode without short circuit and limit the time of applying biases. After preparing a more stable sample, the charge accumulation and depletion at the $SrTiO_3$/GaAs interface under external biases, which is important to understand the microscopic ferroelectric behavior, will be emphasized in a future study.

2D MXenes can be easily synthesized in experiments, however, the methods for cutting MXene nanoribbons from 2D MXenes have not been reported in previous literature to the best of my knowledge. Nevertheless, it might be possible to produce MXene nanoribbons using approaches similar to produce graphene nanoribbons, such as lithography, bottom-up synthesis from polycyclic molecules, and unzipping nanotubes. In future work, it is essential to find a practical means to fabricate the MXene nanoribbons with desired edge types, which can then be characterized using STEM imaging and EELS analysis at low acceleration voltage.

In future work, the surface-dependent splitting of O K-edge prepeak in $LiCoO_2$ nanoplatelets can be confirmed by atomic-resolution EELS mapping of O K-ELNES at different surfaces. Furthermore, quantitative analysis of the intensity ratio of the split O K-edge prepeaks is

important to further understand the magnetic properties intrinsic to the nanoplatelet surfaces. This requires more accurate calculations of electron density of states, which can be achieved by using the hybrid functional in DFT modeling. In addition, the diffusion pattern of Al during the thermal annealing process can also be studied to further understand the gradient surface structure.

Future study of $BaTiO_3$ nanocubes can focus on mapping the polarization from different directions, such as [110] and [111], to determine the polarization pattern in the three-dimensional models. This can be achieved by using a tomography TEM holder with larger tilting angles ($\pm 90°$). Moreover, the effect of surface energetics and arrangement on the ferroelectric ordering in these nanocubes needs to be further studied and understood. Additionally, *in-situ* STEM imaging of the ferroelectric switching under external biases will be performed to explore the effects of surface, size and external electrical field on the polarization patterns in these nanocubes.

CITED LITERATURE

1. Cox, P. A.: Transition metal oxides: An introduction to their electronic structure and properties, volume 27. Oxford University Press, 2010.

2. Von Ardenne, M.: Das elektronen-rastermikroskop. Zeitschrift für Physik, 109(9-10):553–572, 1938.

3. Crewe, A. V., Isaacson, M., and Johnson, D.: A simple scanning electron microscope. Review of Scientific Instruments, 40(2):241–246, 1969.

4. Crewe, A., Eggenberger, D., Wall, J., and Welter, L.: Electron gun using a field emission source. Review of Scientific Instruments, 39(4):576–583, 1968.

5. Pennycook, S., Lupini, A., Varela, M., Borisevich, A., Peng, Y., Oxley, M., Van Benthem, K., and Chisholm, M.: Scanning transmission electron microscopy for nanostructure characterization. In Scanning Microscopy for Nanotechnology, pages 152–191. Springer, 2006.

6. Nellist, P. D. and Pennycook, S. J.: Scanning Transmission Electron Microscopy: Imaging and Analysis. Springer, 2011.

7. Krivanek, O., Nellist, P., Dellby, N., Murfitt, M., and Szilagyi, Z.: Towards sub-0.5 å electron beams. Ultramicroscopy, 96(3-4):229–237, 2003.

8. Pennycook, S.: Z-contrast transmission electron microscopy: direct atomic imaging of materials. Annual Review of Materials Science, 22(1):171–195, 1992.

9. Okunishi, E., Ishikawa, I., Sawada, H., Hosokawa, F., Hori, M., and Kondo, Y.: Visualization of light elements at ultrahigh resolution by stem annular bright field microscopy. Microscopy and Microanalysis, 15(S2):164, 2009.

10. Batson, P. E.: Electron microscopy: Hydrogen brightens up. Nature Materials, 10(4):270, 2011.

11. Williams, D. B. and Carter, C. B.: High energy-loss spectra and images. In Transmission Electron Microscopy, pages 715–739. Springer, 2009.

12. Klie, R., Gulec, A., Guo, Z., Paulauskas, T., Qiao, Q., Tao, R., Wang, C., Low, K., Nicholls, A., and Phillips, P.: The new jeol jem-arm200cf at the university of illinois at chicago. Crystal Research and Technology, 49(9):653–662, 2014.

13. Sholl, D. and Steckel, J. A.: Density functional theory: A practical introduction. John Wiley & Sons, 2011.

14. Grimme, S.: Semiempirical hybrid density functional with perturbative second-order correlation. The Journal of Chemical Physics, 124(3):034108, 2006.

15. Zimmerli, U., Parrinello, M., and Koumoutsakos, P.: Dispersion corrections to density functionals for water aromatic interactions. The Journal of Chemical Physics, 120(6):2693–2699, 2004.

16. Grimme, S.: Accurate description of van der waals complexes by density functional theory including empirical corrections. Journal of Computational Chemistry, 25(12):1463–1473, 2004.

17. Von Lilienfeld, O. A., Tavernelli, I., Rothlisberger, U., and Sebastiani, D.: Optimization of effective atom centered potentials for london dispersion forces in density functional theory. Physical Review Letters, 93(15):153004, 2004.

18. Tkatchenko, A. and Scheffler, M.: Accurate molecular van der waals interactions from ground-state electron density and free-atom reference data. Physical Review Letters, 102(7):073005, 2009.

19. Hohenberg, P. and Kohn, W.: Inhomogeneous electron gas. Physical Review, 136(3B):B864, 1964.

20. Kohn, W. and Sham, L. J.: Self-consistent equations including exchange and correlation effects. Physical Review, 140(4A):A1133, 1965.

21. Becke, A. D.: Perspective: Fifty years of density-functional theory in chemical physics. The Journal of Chemical Physics, 140(18):18A301, 2014.

22. Perdew, J. P., Chevary, J. A., Vosko, S. H., Jackson, K. A., Pederson, M. R., Singh, D. J., and Fiolhais, C.: Atoms, molecules, solids, and surfaces: Applications of the generalized gradient approximation for exchange and correlation. Physical Review B, 46(11):6671, 1992.

23. Perdew, J. P., Burke, K., and Ernzerhof, M.: Generalized gradient approximation made simple. Physical Review Letters, 77(18):3865, 1996.

24. Terakura, K., Oguchi, T., Williams, A., and Kübler, J.: Band theory of insulating transition-metal monoxides: Band-structure calculations. Physical Review B, 30(8):4734, 1984.

25. Sawatzky, G. and Allen, J.: Magnitude and origin of the band gap in nio. Physical Review Letters, 53(24):2339, 1984.

26. Anisimov, V. I., Zaanen, J., and Andersen, O. K.: Band theory and mott insulators: Hubbard u instead of stoner i. Physical Review B, 44(3):943, 1991.

27. Cococcioni, M. and De Gironcoli, S.: Linear response approach to the calculation of the effective interaction parameters in the lda+ u method. Physical Review B, 71(3):035105, 2005.

28. Liechtenstein, A., Anisimov, V., and Zaanen, J.: Density-functional theory and strong interactions: Orbital ordering in mott-hubbard insulators. Physical Review B, 52(8):R5467, 1995.

29. Dudarev, S., Botton, G., Savrasov, S., Humphreys, C., and Sutton, A.: Electron-energy-loss spectra and the structural stability of nickel oxide: An lsda+u study. Physical Review B, 57(3):1505, 1998.

30. Kresse, G. and Furthmüller, J.: Efficient iterative schemes for ab initio total-energy calculations using a plane-wave basis set. Physical Review B, 54(16):11169, 1996.

31. Adapted from vasp website. http://www.vasp.at.

32. McKee, R., Walker, F., and Chisholm, M.: Crystalline oxides on silicon: the first five monolayers. Physical Review Letter, 81(14):3014, 1998.

33. Smith, D. J., Wu, H., Lu, S., Aoki, T., Ponath, P., Fredrickson, K., McDaniel, M. D., Lin, E., Posadas, A. B., Demkov, A. A., Ekerdt, J., and McCartney, M. R.: Recent studies of oxide-semiconductor heterostructures using aberration-corrected scanning transmission electron microscopy. Journal of Materials Research and Technology, 32(5):912–920, 2017.

34. Liang, Y., Kulik, J., Eschrich, T., Droopad, R., Yu, Z., and Maniar, P.: Hetero-epitaxy of perovskite oxides on gaas (001) by molecular beam epitaxy. Applied Physics Letter, 85(7), 2004.

35. Liang, Y., Curless, J. A., and McCready, D. E.: Band alignment at epitaxial $srtio_3$-gaas (001) heterojunction. Applied Physics Letter, 86(44078), 2005.

36. Klie, R., Zhu, Y., Altman, E., and Liang, Y.: Atomic structure of epitaxial $srtio_3$-gaas (001) heterojunctions. Applied Physics Letter, 87(14):3106, 2005.

37. Qiao, Q., Klie, R. F., Öğüt, S., and Idrobo, J.: Atomic and electronic structures of $srtio_3$/gaas heterointerfaces: An 80-kv atomic-resolution electron energy-loss spectroscopy study. Physical Review B, 85(16):165406, 2012.

38. Wu, Z., Huang, W., Wong, K.-h., and Hao, J.: Structural and dielectric properties of epitaxial $srtio_3$ films grown directly on gaas substrates by laser molecular beam epitaxy. Journal of Applied Physics, 104(5):1–3, 2008.

39. Wei, X., Huang, W., Yang, Z., and Hao, J.: Interfacial and rectifying characteristic of epitaxial $srtio_3$-δ/gaas p-n junctions. Scripta Materialia, 65(4):323–326, 2011.

40. Contreras-Guerrero, R., Veazey, J., Levy, J., and Droopad, R.: Properties of epitaxial $batio_3$ deposited on gaas. Applied Physics Letter, 102(1):012907, 2013.

41. Louahadj, L., Bachelet, R., Regreny, P., Largeau, L., Dubourdieu, C., and Saint-Girons, G.: Molecular beam epitaxy of $srtio_3$ on gaas (001): Gaas surface treatment and structural characterization of the oxide layer. Thin Solid Films, 563:2–5, 2014.

42. Meunier, B., Bachelet, R., Grenet, G., Botella, C., Regreny, P., Largeau, L., Penuelas, J., and Saint-Girons, G.: The role of titanium at the $srtio_3$/gaas epitaxial interface. Journal of Crystal Growth, 433:139–142, 2016.

43. Bottin, F. and Finocchi, F.: $Srtio_3$ substrates capped with a gaas monolayer: An ab initio study. Physical Review B, 76(16):165427, 2007.

44. Wang, J., Wu, X., and Bai, D.: Stable structure and effects of the substrate ti pretreatment on the epitaxial growth of $srtio_3$ on gaas. EPL-Europhysics Letter, 86(4):46008, 2009.

45. Hong, L., Öğüt, S., and Klie, R.: Transmission electron microscopic and first-principles study of srtio$_3$/gaas hetero-interfaces. Microscopy & Microanalysis, 21(S3):1647–1648, 2015.

46. Gatabi, J., Lyon, K., Rahman, S., Caro, M., Rojas-Ramirez, J., Cott-Garcia, J., Droopad, R., and Lee, B.: Functional materials integrated on iii-v semiconductors. Microelectronic Engineering, 147:117–121, 2015.

47. Droopad, R.: Growth of compound semiconductor structures on patterned oxide films and process for fabricating same, January 6 2004. US Patent 6,673,646.

48. Eisenbeiser, K., Emrick, R., Droopad, R., Yu, Z., Finder, J., Rockwell, S., Holmes, J., Overgaard, C., and Ooms, W.: Gaas mesfets fabricated on si substrates using a srtio$_3$ buffer layer. IEEE Xplore: IEEE Electron Device Letters, 23(6):300–302, 2002.

49. Rahman, M. S., Ghose, S., Hong, L., Dhungana, P., Fahami, A., Gatabi, J. R., Rojas-Ramirez, J. S., Zakhidov, A., Klie, R. F., Pandey, R., et al.: Integration of bifeo$_3$/la$_{0.7}$sr$_{0.3}$mno$_3$ heterostructures with iii-v semiconductors for low-power non-volatile memory and multiferroic field effect transistors. Journal of Materials Chemistry C, 4(43):10386–10394, 2016.

50. Qiao, Q., Zhang, Y., Contreras-Guerrero, R., Droopad, R., Pantelides, S. T., Pennycook, S. J., Öğüt, S., and Klie, R. F.: Direct observation of oxygen-vacancy-enhanced polarization in a srtio$_3$-buffered ferroelectric batio$_3$ film on gaas. Applied Physics Letter, 107(20):201604, 2015.

51. Droopad, R., Yu, Z., Li, H., Liang, Y., Overgaard, C., Demkov, A., Zhang, X., Moore, K., Eisenbeiser, K., Hu, M., et al.: Development of integrated heterostructures on silicon by mbe. Journal of Crystal Growth, 251(1):638–644, 2003.

52. Kresse, G. and Joubert, D.: From ultrasoft pseudopotentials to the projector augmented-wave method. Physical Review B, 59(3):1758, 1999.

53. Zhang, S. and Wei, S.-H.: Surface energy and the common dangling bond rule for semiconductors. Physical Review Letter, 92(8):086102, 2004.

54. Qian, G.-X., Martin, R. M., and Chadi, D.: First-principles study of the atomic reconstructions and energies of ga-and as-stabilized gaas (100) surfaces. Physical Review B, 38(11):7649, 1988.

55. Hellberg, C. S., Andersen, K. E., Li, H., Ryan, P., and Woicik, J.: Structure of $srtio_3$ films on si. Physical Review Letter, 108(16):166101, 2012.

56. Sands, T., Washburn, J., and Gronsky, R.: Crystallographic relationships between gaas, as and ga_2o_3 at the gaas-thermal oxide interface. Materials Letters, 3(5-6):247–250, 1985.

57. Wieder, H.: Perspectives on iii-v compound mis structures. Journal of Vacuum Science and Technology, 15(4):1498–1506, 1978.

58. De Groot, F., Figueiredo, M., Basto, M., Abbate, M., Petersen, H., and Fuggle, J.: 2p x-ray absorption of titanium in minerals. Physics and Chemistry of Minerals, 19(3):140–147, 1992.

59. Stoyanov, E., Langenhorst, F., and Steinle-Neumann, G.: The effect of valence state and site geometry on ti $l_{3,2}$ and o k electron energy-loss spectra of ti_xo_y phases. American Mineralogist, 92(4):577–586, 2007.

60. Muller, D. A., Nakagawa, N., Ohtomo, A., Grazul, J. L., and Hwang, H. Y.: Atomic-scale imaging of nanoengineered oxygen vacancy profiles in $srtio_3$. Nature, 430(7000):657–661, 2004.

61. Browning, N., Buban, J., Moltaji, H., Pennycook, S., Duscher, G., Johnson, K., Rodrigues, R., and Dravid, V.: The influence of atomic structure on the formation of electrical barriers at grain boundaries in $srtio_3$. Applied Physical Letter, 74(18):2638–2640, 1999.

62. Reuter, K. and Scheffler, M.: Composition, structure, and stability of ruo_2 (110) as a function of oxygen pressure. Physical Review B, 65(3):035406, 2001.

63. Kolpak, A. and Ismail-Beigi, S.: Thermodynamic stability and growth kinetics of epitaxial $srtio_3$ on silicon. Physical Review B, 83(16):165318, 2011.

64. Pashley, M.: Electron counting model and its application to island structures on molecular-beam epitaxy grown gaas (001) and znse (001). Physical Review B, 40(15):10481, 1989.

65. Wang, C. and Pickett, W.: Density-functional theory of excitation spectra of semiconductors: Application to si. Physical Review Letter, 51(7):597, 1983.

66. Ohtomo, A. and Hwang, H.: A high-mobility electron gas at the $laalo_3/srtio_3$ heterointerface. Nature, 427(6973):423–426, 2004.

67. Eckstein, J. N.: Oxide interfaces: Watch out for the lack of oxygen. Nature Materials, 6(7):473–474, 2007.

68. Popović, Z. S., Satpathy, S., and Martin, R. M.: Origin of the two-dimensional electron gas carrier density at the $laalo_3$ on $srtio_3$ interface. Physical Review Letter, 101(25):256801, 2008.

69. Nakagawa, N., Hwang, H. Y., and Muller, D. A.: Why some interfaces cannot be sharp. Nature Materials, 5(3):204–209, 2006.

70. Thiel, S., Hammerl, G., Schmehl, A., Schneider, C., and Mannhart, J.: Tunable quasi-two-dimensional electron gases in oxide heterostructures. Science, 313(5795):1942–1945, 2006.

71. Brinkman, A., Huijben, M., Van Zalk, M., Huijben, J., Zeitler, U., Maan, J., Van der Wiel, W., Rijnders, G., Blank, D., and Hilgenkamp, H.: Magnetic effects at the interface between non-magnetic oxides. Nature Materials, 6(7):493–496, 2007.

72. Siemons, W., Koster, G., Yamamoto, H., Harrison, W. A., Lucovsky, G., Geballe, T. H., Blank, D. H., and Beasley, M. R.: Origin of charge density at $laalo_3$ on $srtio_3$ heterointerfaces: Possibility of intrinsic doping. Physical Review Letter, 98(19):196802, 2007.

73. Kalabukhov, A., Gunnarsson, R., Börjesson, J., Olsson, E., Claeson, T., and Winkler, D.: Effect of oxygen vacancies in the $srtio_3$ substrate on the electrical properties of the $laalo_3/srtio_3$ interface. Physical Review B, 75(12):121404, 2007.

74. Santander-Syro, A., Copie, O., Kondo, T., Fortuna, F., Pailhes, S., Weht, R., Qiu, X., Bertran, F., Nicolaou, A., Taleb-Ibrahimi, A., et al.: Two-dimensional electron gas with universal subbands at the surface of $srtio_3$. Nature, 469(7329):189–193, 2011.

75. Yakovkin, I. N. and Gutowski, M.: $Srtio_3$/si (001) epitaxial interface: A density functional theory study. Physical Review B, 70(16):165319, 2004.

76. Kolpak, A. and Ismail-Beigi, S.: Interface structure and film polarization in epitaxial $srtio_3$/si (001). Physical Review B, 85(19):195318, 2012.

77. Wang, X. and Zhou, Y.: Layered machinable and electrically conductive ti_2alc and ti_3alc_2 ceramics: A review. Journal of Materials Science & Technology, 26(5):385–416, 2010.

78. Sun, Z.: Progress in research and development on max phases: A family of layered ternary compounds. International Materials Reviews, 56(3):143–166, 2011.

79. Barsoum, M. W. and Radovic, M.: Elastic and mechanical properties of the max phases. Annual Review of Materials Research, 41:195–227, 2011.

80. Naguib, M., Mochalin, V. N., Barsoum, M. W., and Gogotsi, Y.: 25th anniversary article: Mxenes: A new family of two-dimensional materials. Advanced Materials, 26(7):992–1005, 2014.

81. Eklund, P., Beckers, M., Jansson, U., Högberg, H., and Hultman, L.: The $m_{n+1}ax_n$ phases: Materials science and thin-film processing. Thin Solid Films, 518(8):1851–1878, 2010.

82. Naguib, M., Kurtoglu, M., Presser, V., Lu, J., Niu, J., Heon, M., Hultman, L., Gogotsi, Y., and Barsoum, M. W.: Two-dimensional nanocrystals produced by exfoliation of ti_3alc_2. Advanced Materials, 23(37):4248–4253, 2011.

83. Naguib, M., Mashtalir, O., Carle, J., Presser, V., Lu, J., Hultman, L., Gogotsi, Y., and Barsoum, M. W.: Two-dimensional transition metal carbides. ACS Nano, 6(2):1322–1331, 2012.

84. Ghidiu, M., Lukatskaya, M. R., Zhao, M.-Q., Gogotsi, Y., and Barsoum, M. W.: Conductive two-dimensional titanium carbide ćlayẃith high volumetric capacitance. Nature, 516(7529):78–81, 2014.

85. Barsoum, M. W.: The $m_{n+1}ax_n$ phases: A new class of solids: thermodynamically stable nanolaminates. Progress in Solid State Chemistry, 28(1):201–281, 2000.

86. Music, D., Sun, Z., Ahuja, R., and Schneider, J. M.: Coupling in nanolaminated ternary carbides studied by theoretical means: The influence of electronic potential approximations. Physical Review B, 73:134117, Apr 2006.

87. Sun, Z., Music, D., Ahuja, R., Li, S., and Schneider, J. M.: Bonding and classification of nanolayered ternary carbides. Physical Review B, 70:092102, Sep 2004.

88. Emmerlich, J., Music, D., Houben, A., Dronskowski, R., and Schneider, J. M.: Systematic study on the pressure dependence of M_2AlC phases (m = Ti, V, Cr, Zr, Nb, Mo, Hf, Ta, W). Physical Review B, 76:224111, Dec 2007.

89. Khazaei, M., Arai, M., Sasaki, T., Chung, C.-Y., Venkataramanan, N. S., Estili, M., Sakka, Y., and Kawazoe, Y.: Novel electronic and magnetic properties of two-dimensional transition metal carbides and nitrides. Advanced Functional Materials, 23(17):2185–2192, 2013.

90. Xie, Y. and Kent, P.: Hybrid density functional study of structural and electronic properties of functionalized $ti_{n+1}x_n$ (x=c, n) monolayers. Physical Review B, 87(23):235441, 2013.

91. Hu, Q., Wang, H., Wu, Q., Ye, X., Zhou, A., Sun, D., Wang, L., Liu, B., and He, J.: Two-dimensional sc_2c: A reversible and high-capacity hydrogen storage material predicted by first-principles calculations. International Journal of Hydrogen Energy, 39(20):10606–10612, 2014.

92. Lee, Y., Cho, S. B., and Chung, Y.-C.: Tunable indirect to direct band gap transition of monolayer sc_2co_2 by the strain effect. ACS Applied Materials & Interfaces, 6(16):14724–14728, 2014.

93. Zhao, S., Kang, W., and Xue, J.: Manipulation of electronic and magnetic properties of m_2c (m=hf, nb, sc, ta, ti, v, zr) monolayer by applying mechanical strains. Applied Physics Letter, 104(13):133106, 2014.

94. Wang, S., Li, J.-X., Du, Y.-L., and Cui, C.: First-principles study on structural, electronic and elastic properties of graphene-like hexagonal ti_2c monolayer. Computational Materials Science, 83:290–293, 2014.

95. Lee, Y., Hwang, Y., Cho, S. B., and Chung, Y.-C.: Achieving a direct band gap in oxygen functionalized-monolayer scandium carbide by applying an electric field. Physical Chemistry Chemical Physics, 16(47):26273–26278, 2014.

96. Anasori, B., Xie, Y., Beidaghi, M., Lu, J., Hosler, B. C., Hultman, L., Kent, P. R., Gogotsi, Y., and Barsoum, M. W.: Two-dimensional, ordered, double transition metals carbides (mxenes). ACS Nano, 9(10):9507–9516, 2015.

97. Yu, X.-F., Cheng, J.-B., Liu, Z.-B., Li, Q.-Z., Li, W.-Z., Yang, X., and Xiao, B.: The band gap modulation of monolayer ti_2co_2 by strain. RSC Advances, 5(39):30438–30444, 2015.

98. Zhao, S., Kang, W., and Xue, J.: Mxene nanoribbons. Journal of Materials Chemistry C, 3(4):879–888, 2015.

99. Lee, Y., Hwang, Y., and Chung, Y.-C.: Achieving type i, ii, and iii heterojunctions using functionalized mxene. ACS Applied Materials & Interfaces, 7(13):7163–7169, 2015.

100. Guo, Z., Zhou, J., Si, C., and Sun, Z.: Flexible two-dimensional $ti_{n+1}c_n$ ($n = 1$, 2 and 3) and their functionalized mxenes predicted by density functional theories. Physical Chemistry Chemical Physics, 17:15348–15354, 2015.

101. Zhang, X., Ma, Z., Zhao, X., Tang, Q., and Zhou, Z.: Computational studies on structural and electronic properties of functionalized mxene monolayers and nanotubes. Journal of Materials Chemistry, 3(9):4960–4966, 2015.

102. Li, X., Dai, Y., Ma, Y., Liu, Q., and Huang, B.: Intriguing electronic properties of two-dimensional mos_2/tm_2co_2 (tm=ti, zr, or hf) hetero-bilayers: type-ii semiconductors with tunable band gaps. Nanotechnology, 26(13):135703, 2015.

103. Khazaei, M., Arai, M., Sasaki, T., Ranjbar, A., Liang, Y., and Yunoki, S.: Oh-terminated two-dimensional transition metal carbides and nitrides as ultralow work function materials. Physical Review B, 92(7):075411, 2015.

104. Xia, Y., Yang, P., Sun, Y., Wu, Y., Mayers, B., Gates, B., Yin, Y., Kim, F., and Yan, H.: One-dimensional nanostructures: Synthesis, characterization, and applications. Advanced Materials, 15(5):353–389, 2003.

105. Son, Y.-W., Cohen, M. L., and Louie, S. G.: Energy gaps in graphene nanoribbons. Physical Review Letter, 97(21):216803, 2006.

106. Nakada, K., Fujita, M., Dresselhaus, G., and Dresselhaus, M. S.: Edge state in graphene ribbons: Nanometer size effect and edge shape dependence. Physical Review B, 54(24):17954, 1996.

107. Fujita, M., Wakabayashi, K., Nakada, K., and Kusakabe, K.: Peculiar localized state at zigzag graphite edge. Journal of the Physical Society of Japan, 65(7):1920–1923, 1996.

108. Wakabayashi, K., Fujita, M., Ajiki, H., and Sigrist, M.: Electronic and magnetic properties of nanographite ribbons. Physical Review B, 59(12):8271, 1999.

109. Yang, L., Park, C.-H., Son, Y.-W., Cohen, M. L., and Louie, S. G.: Quasiparticle energies and band gaps in graphene nanoribbons. Physical Review Letter, 99(18):186801, 2007.

110. Han, M. Y., Özyilmaz, B., Zhang, Y., and Kim, P.: Energy band-gap engineering of graphene nanoribbons. Physical Review Letter, 98(20):206805, 2007.

111. Barone, V., Hod, O., and Scuseria, G. E.: Electronic structure and stability of semiconducting graphene nanoribbons. Nano Letters, 6(12):2748–2754, 2006.

112. Ezawa, M.: Peculiar width dependence of the electronic properties of carbon nanoribbons. Physical Review B, 73(4):045432, 2006.

113. Mohanty, N., Moore, D., Xu, Z., Sreeprasad, T., Nagaraja, A., Rodriguez, A. A., and Berry, V.: Nanotomy-based production of transferable and dispersible graphene nanostructures of controlled shape and size. Nature Communications, 3:844, 2012.

114. Cai, J., Pignedoli, C. A., Talirz, L., Ruffieux, P., Söde, H., Liang, L., Meunier, V., Berger, R., Li, R., Feng, X., et al.: Graphene nanoribbon heterojunctions. Nature Nanotechnology, 9(11):896–900, 2014.

115. Song, Y.-L., Zhang, Y., Zhang, J.-M., and Lu, D.-B.: Effects of the edge shape and the width on the structural and electronic properties of silicene nanoribbons. Applied Surface Science, 256(21):6313–6317, 2010.

116. De Padova, P., Kubo, O., Olivieri, B., Quaresima, C., Nakayama, T., Aono, M., and Le Lay, G.: Multilayer silicene nanoribbons. Nano Letters, 12(11):5500–5503, 2012.

117. Pan, L., Liu, H., Tan, X., Lv, H., Shi, J., Tang, X., and Zheng, G.: Thermoelectric properties of armchair and zigzag silicene nanoribbons. Physical Chemistry Chemical Physics, 14(39):13588–13593, 2012.

118. Osborn, T. H. and Farajian, A. A.: Silicene nanoribbons as carbon monoxide nanosensors with molecular resolution. Nano Research, 7(7):945–952, 2014.

119. Lopez-Bezanilla, A., Huang, J., Terrones, H., and Sumpter, B. G.: Boron nitride nanoribbons become metallic. Nano Letters, 11(8):3267–3273, 2011.

120. Park, C.-H. and Louie, S. G.: Energy gaps and stark effect in boron nitride nanoribbons. Nano Letters, 8(8):2200–2203, 2008.

121. Zheng, F., Zhou, G., Liu, Z., Wu, J., Duan, W., Gu, B.-L., and Zhang, S.: Half metallicity along the edge of zigzag boron nitride nanoribbons. Physical Review B, 78(20):205415, 2008.

122. Kou, L., Tang, C., Zhang, Y., Heine, T., Chen, C., and Frauenheim, T.: Tuning magnetism and electronic phase transitions by strain and electric field in zigzag mos_2 nanoribbons. Journal of Physical Chemistry Letters, 3(20):2934–2941, 2012.

123. Liu, Z., Suenaga, K., Wang, Z., Shi, Z., Okunishi, E., and Iijima, S.: Identification of active atomic defects in a monolayered tungsten disulphide nanoribbon. Nature Communications, 2:213, 2011.

124. Dolui, K., Pemmaraju, C. D., and Sanvito, S.: Electric field effects on armchair mos_2 nanoribbons. ACS Nano, 6(6):4823–4834, 2012.

125. Li, Y., Zhou, Z., Zhang, S., and Chen, Z.: Mos2 nanoribbons: High stability and unusual electronic and magnetic properties. Journal of the American Chemical Society, 130(49):16739–16744, 2008.

126. Reyes-Retana, J., Naumis, G., and Cervantes-Sodi, F.: Centered honeycomb $nise_2$ nanoribbons: Structure and electronic properties. Journal of Physical Chemistry C, 118(6):3295–3304, 2014.

127. Tapasztó, L., Dobrik, G., Lambin, P., and Biró, L. P.: Tailoring the atomic structure of graphene nanoribbons by scanning tunnelling microscope lithography. Nature Nanotechnology, 3(7):397–401, 2008.

128. Jiao, L., Zhang, L., Wang, X., Diankov, G., and Dai, H.: Narrow graphene nanoribbons from carbon nanotubes. Nature, 458(7240):877–880, 2009.

129. Cai, J., Ruffieux, P., Jaafar, R., Bieri, M., Braun, T., Blankenburg, S., Muoth, M., Seitsonen, A. P., Saleh, M., Feng, X., et al.: Atomically precise bottom-up fabrication of graphene nanoribbons. Nature, 466(7305):470–473, 2010.

130. Zhang, X., Zhao, X., Wu, D., Jing, Y., and Zhou, Z.: High and anisotropic carrier mobility in experimentally possible ti_2co_2 (mxene) monolayer and nanoribbons. Nanoscale, 7:16020–16025, 2015.

131. Tang, Q., Zhou, Z., and Shen, P.: Are mxenes promising anode materials for li ion batteries? computational studies on electronic properties and li storage capability of ti3c2 and ti3c2x2 (x= f, oh) monolayer. Journal of the American Chemical Society, 134(40):16909–16916, 2012.

132. Haug, H. and Koch, S.: Quantum Theory of the Optical and Electronic Properties of Semiconductors. World Scientific, 1994.

133. Bredow, T., Giordano, L., Cinquini, F., and Pacchioni, G.: Electronic properties of rutile tio_2 ultrathin films: Odd-even oscillations with the number of layers. Physical Review B, 70(3):035419, 2004.

134. Okubo, M., Hosono, E., Kim, J., Enomoto, M., Kojima, N., Kudo, T., Zhou, H., and Honma, I.: Nanosize effect on high-rate li-ion intercalation in $licoo_2$ electrode. Journal of the American Chemical Society, 129(23):7444–7452, 2007.

135. Chen, H. and Grey, C. P.: Molten salt synthesis and high rate performance of the "desert-rose" form of $licoo_2$. Advanced Materials, 20(11):2206–2210, 2008.

136. Okubo, M., Kim, J., Kudo, T., Zhou, H., and Honma, I.: Anisotropic surface effect on electronic structures and electrochemical properties of $licoo_2$. The Journal of Physical Chemistry C, 113(34):15337–15342, 2009.

137. Alva, G., Kim, C., Yi, T., Cook, J. B., Xu, L., Nolis, G. M., and Cabana, J.: Surface chemistry consequences of mg-based coatings on lini0. 5mn1. 5o4 electrode materials upon operation at high voltage. The Journal of Physical Chemistry C, 118(20):10596–10605, 2014.

138. Hu, L., Bruner, P., Grehl, T., Brongersma, H. H., and Cabana, J.: Control of chemical structure in core-shell nanocrystals for the stabilization of battery electrode/electrolyte interfaces. Chemistry of Materials, 29(14):5896–5905, 2017.

139. Kramer, D. and Ceder, G.: Tailoring the morphology of $licoo_2$: A first-principles study. Chemistry of Materials, 21(16):3799–3809, 2009.

140. Qian, D., Hinuma, Y., Chen, H., Du, L.-S., Carroll, K. J., Ceder, G., Grey, C. P., and Meng, Y. S.: Electronic spin transition in nanosize stoichiometric lithium cobalt oxide. Journal of the American Chemical Society, 134(14):6096–6099, 2012.

141. Han, B., Qian, D., Risch, M., Chen, H., Chi, M., Meng, Y. S., and Shao-Horn, Y.: Role of $licoo_2$ surface terminations in oxygen reduction and evolution kinetics. The journal of physical chemistry letters, 6(8):1357–1362, 2015.

142. Cabana, J., Kwon, B. J., and Hu, L.: Mechanisms of degradation and strategies for the stabilization of cathode-electrolyte interfaces in li-ion batteries. Accounts of Chemical Research, 51(2):299–308, 2018.

143. Garcia, J. C., Bareño, J., Yan, J., Chen, G., Hauser, A., Croy, J. R., and Iddir, H.: Surface structure, morphology, and stability of $li(ni_{1/3}mn_{1/3}co_{1/3})o_2$ cathode material. The Journal of Physical Chemistry C, 121(15):8290–8299, 2017.

144. Yogi, C., Takamatsu, D., Yamanaka, K., Arai, H., Uchimoto, Y., Kojima, K., Watanabe, I., Ohta, T., and Ogumi, Z.: Soft x-ray absorption spectroscopic studies with different probing depths: Effect of an electrolyte additive on electrode surfaces. Journal of Power Sources, 248:994–999, 2014.

145. Klie, R. F., Qiao, Q., Paulauskas, T., Gulec, A., Rebola, A., Öğüt, S., Prange, M. P., Idrobo, J., Pantelides, S. T., Kolesnik, S., et al.: Observations of co^{4+} in a higher spin state and the increase in the seebeck coefficient of thermoelectric $ca_3co_4o_9$. Physical Review Letters, 108(19):196601, 2012.

146. Li, C.-N., Yang, J.-M., Krasnov, V., Arias, J., and Nieh, K.-W.: Phase transformation of nanocrystalline $licoo_2$ cathode after high-temperature cycling. Electrochemical and Solid-State Letters, 11(5):A81–A83, 2008.

147. Chattopadhyay, S., Ayyub, P., Palkar, V., and Multani, M.: Size-induced diffuse phase transition in the nanocrystalline ferroelectric $pbtio_3$. Physical Review B, 52(18):13177, 1995.

148. Zhong, W., Wang, Y., Zhang, P., and Qu, B.: Phenomenological study of the size effect on phase transitions in ferroelectric particles. Physical Review B, 50(2):698, 1994.

149. Smith, M. B., Page, K., Siegrist, T., Redmond, P. L., Walter, E. C., Seshadri, R., Brus, L. E., and Steigerwald, M. L.: Crystal structure and the paraelectric-to-ferroelectric phase transition of nanoscale batio$_3$. Journal of the American Chemical Society, 130(22):6955–6963, 2008.

150. Petkov, V., Gateshki, M., Niederberger, M., and Ren, Y.: Atomic-scale structure of nanocrystalline ba$_x$sr$_{1-x}$tio$_3$ (x = 1, 0.5, 0) by x-ray diffraction and the atomic pair distribution function technique. Chemistry of Materials, 18(3):814–821, 2006.

151. Page, K., Proffen, T., Niederberger, M., and Seshadri, R.: Probing local dipoles and ligand structure in batio$_3$ nanoparticles. Chemistry of Materials, 22(15):4386–4391, 2010.

152. Naumov, I. I., Bellaiche, L., and Fu, H.: Unusual phase transitions in ferroelectric nanodisks and nanorods. Nature, 432(7018):737, 2004.

153. Kretschmer, R. and Binder, K.: Surface effects on phase transitions in ferroelectrics and dipolar magnets. Physical Review B, 20(3):1065, 1979.

154. Morozovska, A. N., Glinchuk, M. D., and Eliseev, E. A.: Phase transitions induced by confinement of ferroic nanoparticles. Physical Review B, 76(1):014102, 2007.

155. Adireddy, S., Lin, C., Cao, B., Zhou, W., and Caruntu, G.: Solution-based growth of monodisperse cube-like batio$_3$ colloidal nanocrystals. Chemistry of Materials, 22(6):1946–1948, 2010.

156. Polking, M. J., Han, M.-G., Yourdkhani, A., Petkov, V., Kisielowski, C. F., Volkov, V. V., Zhu, Y., Caruntu, G., Alivisatos, A. P., and Ramesh, R.: Ferroelectric order in individual nanometre-scale crystals. Nature Materials, 11(8):700, 2012.

157. Caruntu, D., Rostamzadeh, T., Costanzo, T., Parizi, S. S., and Caruntu, G.: Solvothermal synthesis and controlled self-assembly of monodisperse titanium-based perovskite colloidal nanocrystals. Nanoscale, 7(30):12955–12969, 2015.

158. Lencer, D., Salinga, M., Grabowski, B., Hickel, T., Neugebauer, J., and Wuttig, M.: A map for phase-change materials. Nature Materials, 7(12):972, 2008.

159. Egerton, R. F.: Electron energy-loss spectroscopy in the electron microscope. Springer Science & Business Media, 2011.

160. Langreth, D. C. and Mehl, M.: Beyond the local-density approximation in calculations of ground-state electronic properties. Physical Review B, 28(4):1809, 1983.

161. Becke, A. D.: Density-functional exchange-energy approximation with correct asymptotic behavior. Physical Review A, 38(6):3098, 1988.

162. Lee, C., Yang, W., and Parr, R. G.: Development of the colle-salvetti correlation-energy formula into a functional of the electron density. Physical Review B, 37(2):785, 1988.

163. Hong, M., Kwo, J., Kortan, A., Mannaerts, J., and Sergent, A.: Epitaxial cubic gadolinium oxide as a dielectric for gallium arsenide passivation. Science, 283(5409):1897–1900, 1999.

164. Ahn, C., Rabe, K., and Triscone, J.-M.: Ferroelectricity at the nanoscale: Local polarization in oxide thin films and heterostructures. Science, 303(5657):488–491, 2004.

165. Haeni, J., Irvin, P., Chang, W., Uecker, R., Reiche, P., Li, Y., Choudhury, S., Tian, W., Hawley, M., Craigo, B., et al.: Room-temperature ferroelectricity in strained srtio$_3$. Nature, 430(7001):758–761, 2004.

166. Blamire, M. G., MacManus-Driscoll, J. L., Mathur, N. D., and Barber, Z. H.: The materials science of functional oxide thin films. Advanced Materials, 21(38-39):3827–3839, 2009.

167. LaBella, V. P., Krause, M. R., Ding, Z., and Thibado, P. M.: Arsenic-rich gaas (001) surface structure. Surface Science Reports, 60(1):1–53, 2005.

168. Ohtake, A.: Surface reconstructions on gaas (001). Surface Science Reports, 63(7):295–327, 2008.

169. Hybertsen, M. S. and Louie, S. G.: First-principles theory of quasiparticles: Calculation of band gaps in semiconductors and insulators. Physical Review Letter, 55(13):1418, 1985.

170. Pauli, S. and Willmott, P.: Conducting interfaces between polar and non-polar insulating perovskites. Journal of Physics: Condensed Matter, 20(26):264012, 2008.

171. Stull, D. R. and Prophet, H.: Janaf thermochemical tables. Technical report, DTIC Document, 1971.

172. Demkov, A. A. and Posadas, A. B.: Integration of functional oxides with semiconductors. Springer, 2014.

173. Chambers, S. A.: Epitaxial growth and properties of doped transition metal and complex oxide films. Advanced Materials, 22(2):219–248, 2010.

174. Hong, L., Klie, R. F., and Öğüt, S.: First-principles study of size-and edge-dependent properties of mxene nanoribbons. Physical Review B, 93(11):115412, 2016.

175. Mizokawa, T. and Fujimori, A.: Unrestricted hartree-fock study of transition-metal oxides: Spin and orbital ordering in perovskite-type lattice. Physical Review B, 51(18):12880, 1995.

176. Gogoi, P. K., Trevisanutto, P. E., Yang, M., Santoso, I., Asmara, T. C., Terentjevs, A., Della Sala, F., Breese, M. B., Venkatesan, T., Feng, Y. P., et al.: Optical conductivity renormalization of graphene on $srtio_3$ due to resonant excitonic effects mediated by ti $3d$ orbitals. Physical Review B, 91(3):035424, 2015.

177. Okamoto, S., Millis, A. J., and Spaldin, N. A.: Lattice relaxation in oxide heterostructures: $Latio_3/srtio_3$ superlattices. Physical Review Letter, 97(5):056802, 2006.

178. Van de Walle, C. G. and Martin, R. M.: Theoretical calculations of heterojunction discontinuities in the si/ge system. Physical Review B, 34(8):5621, 1986.

179. Baldereschi, A., Baroni, S., and Resta, R.: Band offsets in lattice-matched heterojunctions: A model and first-principles calculations for gaas/alas. Physical Review Letter, 61(6):734, 1988.

180. Krishnaswamy, K., Dreyer, C., Janotti, A., and Van de Walle, C. G.: First-principles study of surface charging in $laalo_3/srtio_3$ heterostructures. Physical Review B, 92(8):085420, 2015.

181. Hong, L., Droopad, R., Öğüt, S., and Klie, R. F.: Structural properties of $srtio_3$/gaas hetero-interfaces. Microscopy & Microanalysis, 22(S3):1454–1455, 2016.

182. Bristowe, N., Ghosez, P., Littlewood, P., and Artacho, E.: The origin of two-dimensional electron gases at oxide interfaces: Insights from theory. Journal of Physics: Condensed Matter, 26(14):143201, 2014.

183. Wei, Y., Hu, X., Liang, Y., Jordan, D., Craigo, B., Droopad, R., Yu, Z., Demkov, A., Edwards Jr, J. L., and Ooms, W. J.: Mechanism of cleaning si (100) surface using sr or sro for the growth of crystalline srtio$_3$ films. Journal of Vacuum Science & Technology. B, 20(4):1402–1405, 2002.

184. Sun, L., Li, Y., Li, Z., Li, Q., Zhou, Z., Chen, Z., Yang, J., and Hou, J.: Electronic structures of sic nanoribbons. Journal of Chemical Physics, 129(17):174114, 2008.

185. Ivanovskii, A. L. and Enyashin, A. N.: Graphene-like transition-metal nanocarbides and nanonitrides. Russian Chemical Reviews, 82(8):735, 2013.

186. Chang, S.-L., Wu, B.-R., Yang, P.-H., and Lin, M.-F.: Curvature effects on electronic properties of armchair graphene nanoribbons without passivation. Physical Chemistry Chemical Physics, 14(47):16409–16414, 2012.

187. Zhang, L., Wang, E., Xue, Q.-K., Zhang, S., and Zhang, Z.: Generalized electron counting in determination of metal-induced reconstruction of compound semiconductor surfaces. Physical Review Letter, 97(12):126103, 2006.

188. Duke, C. B.: Semiconductor surface reconstruction: The structural chemistry of two-dimensional surface compounds. Chemical Reviews, 96(4):1237–1260, 1996.

189. Chadi, D.: Atomic structure of gaas (100)-(2 $\times$ 1) and (2 $\times$ 4) reconstructed surfaces. Journal of Vacuum Science & Technology A, 5(4):834–837, 1987.

190. Li, Z., Hong, L., Jornada, F., Cao, T., Öğüt, S., and Louie, S. G.: Gw-bse calculations on two-dimensional mxene phases. 1:2007, 2015.

191. Maram, P. S., Costa, G. C., and Navrotsky, A.: Experimental confirmation of low surface energy in licoo$_2$ and implications for lithium battery electrodes. Angewandte Chemie International Edition, 52(46):12139–12142, 2013.

192. Cha, H.-W., Kang, M.-C., Shin, K., and Yang, C.-W.: Transmission electron microscopy specimen preparation of delicate materials using tripod polisher. Applied Microscopy, 46(2):110–115, 2016.

193. Durgun, E., Ghosez, P., Shaltaf, R., Gonze, X., and Raty, J.-Y.: Polarization vortices in germanium telluride nanoplatelets: A theoretical study. Physical Review Letters, 103(24):247601, 2009.

194. Kikkawa, J., Terada, S., Gunji, A., Nagai, T., Kurashima, K., and Kimoto, K.: Chemical states of overcharged licoo2 particle surfaces and interiors observed using electron energy-loss spectroscopy. The Journal of Physical Chemistry C, 119(28):15823–15830, 2015.

195. Yoon, W.-S., Kim, K.-B., Kim, M.-G., Lee, M.-K., Shin, H.-J., Lee, J.-M., Lee, J.-S., and Yo, C.-H.: Oxygen contribution on li-ion intercalation- deintercalation in licoo2 investigated by o k-edge and co l-edge x-ray absorption spectroscopy. The Journal of Physical Chemistry B, 106(10):2526–2532, 2002.

196. Graetz, J., Hightower, A., Ahn, C., Yazami, R., Rez, P., and Fultz, B.: Electronic structure of chemically-delithiated licoo2 studied by electron energy-loss spectrometry. The Journal of Physical Chemistry B, 106(6):1286–1289, 2002.

APPENDICES

Appendix A: Reuse License for Figure 2.1.2 and Figure 2.1.3

SPRINGER NATURE LICENSE
TERMS AND CONDITIONS

Jul 06, 2018

This Agreement between University of Illinois at Chicago -- Liang Hong ("You") and Springer Nature ("Springer Nature") consists of your license details and the terms and conditions provided by Springer Nature and Copyright Clearance Center.

License Number	4383281133325
License date	Jul 06, 2018
Licensed Content Publisher	Springer Nature
Licensed Content Publication	Springer eBook
Licensed Content Title	Scanning Transmission Electron Microscopy for Nanostructure Characterization
Licensed Content Author	S. J. Pennycook, A. R. Lupini, M. Varela et al
Licensed Content Date	Jan 1, 2006
Type of Use	Thesis/Dissertation
Requestor type	academic/university or research institute
Format	electronic
Portion	figures/tables/illustrations
Number of figures/tables/illustrations	2
Will you be translating?	no
Circulation/distribution	<501
Author of this Springer Nature content	no
Title	Atomic-Scale Scanning Transmission Electron Microscopy and First-Principles Study of Functional Oxides
Instructor name	Robert Klie
Institution name	University of Illinois at Chicago
Expected presentation date	Jul 2018
Portions	Figure 6.4 and Figure 6.5
Requestor Location	University of Illinois at Chicago 845 W Taylor St MC 273 CHICAGO, IL 60607 United States Attn: University of Illinois at Chicago
Billing Type	Invoice
Billing Address	University of Illinois at Chicago 845 W Taylor St MC 273

Appendix B: Reuse License for Figure 2.1.6

SPRINGER NATURE LICENSE
TERMS AND CONDITIONS

Jul 06, 2018

This Agreement between University of Illinois at Chicago -- Liang Hong ("You") and Springer Nature ("Springer Nature") consists of your license details and the terms and conditions provided by Springer Nature and Copyright Clearance Center.

License Number	4383290006501
License date	Jul 06, 2018
Licensed Content Publisher	Springer Nature
Licensed Content Publication	Springer eBook
Licensed Content Title	Low-Loss and No-Loss Spectra and Images
Licensed Content Author	David B. Williams, C. Barry Carter
Licensed Content Date	Jan 1, 2009
Type of Use	Thesis/Dissertation
Requestor type	academic/university or research institute
Format	electronic
Portion	figures/tables/illustrations
Number of figures/tables/illustrations	1
Will you be translating?	no
Circulation/distribution	<501
Author of this Springer Nature content	no
Title	Atomic-Scale Scanning Transmission Electron Microscopy and First-Principles Study of Functional Oxides
Instructor name	Robert Klie
Institution name	University of Illinois at Chicago
Expected presentation date	Jul 2018
Portions	Figure 40.3
Requestor Location	University of Illinois at Chicago 845 W Taylor St MC 273 CHICAGO, IL 60607 United States Attn: University of Illinois at Chicago
Billing Type	Invoice
Billing Address	University of Illinois at Chicago 845 W Taylor St MC 273

Appendix C: Reuse License for Section 3.1 and 3.2

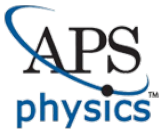

American Physical Society Reuse and Permissions License

06-Jul-2018

This license agreement between the American Physical Society ("APS") and Liang Hong ("You") consists of your license details and the terms and conditions provided by the American Physical Society and SciPris.

Licensed Content Information

License Number:	**RNP/18/JUL/005825**
License date:	06-Jul-2018
DOI:	10.1103/PhysRevB.96.035311
Title:	Atomic-scale structural and electronic properties of ${\mathrm{SrTiO}}_{3}/\mathrm{GaAs}$ interfaces: A combined STEM-EELS and first-principles study
Author:	Liang Hong et al.
Publication:	Physical Review B
Publisher:	American Physical Society
Cost:	USD $ 0.00

Request Details

Does your reuse require significant modifications: No

Specify intended distribution locations:	United States
Reuse Category:	Reuse in a thesis/dissertation
Requestor Type:	Author of requested content
Items for Reuse:	Whole Article
Format for Reuse:	Electronic

Information about New Publication:

University/Publisher:	University of Illinois at Chicago
Title of dissertation/thesis:	Atomic-Scale Scanning Transmission Electron Microscopy and First-Principles Study of Functional Oxides
Author(s):	Liang Hong
Expected completion date:	Jul. 2018

License Requestor Information

Name:	Liang Hong
Affiliation:	Individual
Email Id:	ikiddo1412@gmail.com
Country:	United States

Appendix D: Reuse License for Section 3.3

CAMBRIDGE UNIVERSITY PRESS LICENSE
TERMS AND CONDITIONS

Jul 06, 2018

This Agreement between University of Illinois at Chicago -- Liang Hong ("You") and Cambridge University Press ("Cambridge University Press") consists of your license details and the terms and conditions provided by Cambridge University Press and Copyright Clearance Center.

License Number	4383300947478
License date	Jul 06, 2018
Licensed Content Publisher	Cambridge University Press
Licensed Content Publication	Microscopy and Microanalysis
Licensed Content Title	In-situ STEM-EELS observation of ferroelectric switching of BaTiO3 film on GaAs
Licensed Content Author	Liang Hong, Daniel Huber, Rocio Contreras-Guerrero, Ravi Droopad, Robert F. Klie
Licensed Content Date	Aug 4, 2017
Licensed Content Volume	23
Licensed Content Issue	S1
Start page	1628
End page	1629
Type of Use	Dissertation/Thesis
Requestor type	Author
Portion	Full article
Author of this Cambridge University Press article	Yes
Author / editor of the new work	Yes
Order reference number	
Territory for reuse	North America Only
Title of your thesis / dissertation	Atomic-Scale Scanning Transmission Electron Microscopy and First-Principles Study of Functional Oxides
Expected completion date	Jul 2018
Estimated size(pages)	1
Requestor Location	University of Illinois at Chicago 845 W Taylor St MC 273 CHICAGO, IL 60607 United States Attn: University of Illinois at Chicago
Publisher Tax ID	GB823847609

Appendix E: Reuse License for Chapter 4

American Physical Society Reuse and Permissions License

06-Jul-2018

This license agreement between the American Physical Society ("APS") and Liang Hong ("You") consists of your license details and the terms and conditions provided by the American Physical Society and SciPris.

Licensed Content Information

License Number:	**RNP/18/JUL/005824**
License date:	06-Jul-2018
DOI:	10.1103/PhysRevB.93.115412
Title:	First-principles study of size- and edge-dependent properties of MXene nanoribbons
Author:	Liang Hong, Robert F. Klie, and Serdar Öğüt
Publication:	Physical Review B
Publisher:	American Physical Society
Cost:	USD $ 0.00

Request Details

Does your reuse require significant modifications: No

Specify intended distribution locations:	United States
Reuse Category:	Reuse in a thesis/dissertation
Requestor Type:	Author of requested content
Items for Reuse:	Whole Article
Format for Reuse:	Electronic

Information about New Publication:

University/Publisher:	University of Illinois at Chicago
Title of dissertation/thesis:	Atomic-Scale Scanning Transmission Electron Microscopy and First-Principles Study of Functional Oxides
Author(s):	Liang Hong
Expected completion date:	Jul. 2018

License Requestor Information

Name:	Liang Hong
Affiliation:	Individual
Email Id:	ikiddo1412@gmail.com
Country:	United States

VITA

Liang Hong

Department of Physics · University of Illinois at Chicago
845 W Taylor St, M/C 273 · Chicago, IL 60607, United States
Tel: +1 (312)-888-6350 · Email: lhong7@uic.edu

EDUCATION

University of Illinois at Chicago, United States *Aug. 2012 – Jul. 2018*
Ph.D. in Condensed Matter and Materials Physics
Thesis: "Atomic-scale Scanning Transmission Electron Microscopy and First-Principles Study of Functional Oxides"
Advisors: Dr. Robert F. Klie; Co-Advisor: Dr. Serdar Öğüt

Dalian University of Technology, China *Sept. 2008 – Jun. 2012*
B.Sc. in Physics
Thesis: "First-Principles Simulation of the Ground-State Structures of Binary Clusters"
Advisor: Dr. Jijun Zhao

PUBLICATIONS

Journal Articles

- L. Hong, K. Bhatnagar, R. Droopad, S. Öğüt, R. Klie, "Atomic-scale structural and electronic properties of $SrTiO_3$/GaAs interfaces: A combined STEM-EELS and first-principles study", *Physical Review B*, v.96, p.035311 (2017).
- S. Ghose, M. Rahman, L. Hong, J. Rojas-Ramirez, H. Jin, K. Park, R. Klie, R. Droopad, "Growth and characterization of β-Ga_2O_3 thin films by molecular beam epitaxy for deep-ultraviolet photodetector", *Journal of Applied Physics*, v.122, p.095302 (2017).
- M. Rahman, S. Ghose, L. Hong, P. Dhungana, A. Fahami, J.R. Gatabi, J.S. Rojas-Ramirez, A. Zakhidov, R.F. Klie, R.K. Pandey, R. Droopad, "Integration of $BiFeO_3$/$La_{0.7}Sr_{0.3}MnO_3$ heterostructures with III-V semiconductors for low-power non-volatile memory and multiferroic field effect device", *Journal of Materials Chemistry C*, v.4, p.10386 (2016).
- L. Hong, R. Klie, S. Öğüt, "First-principles study of size- and edge-dependent properties of MXene nanoribbons", *Physical Review B*, v.93, p.115412 (2016).
- L. Hong, H. Wang, J. Cheng, X. Huang, L. Sai, J. Zhao, "Atomic structures and electronic properties of small Au-Ag binary clusters: Effects of size and composition", *Computational and Theoretical Chemistry*, v.993, p.36 (2012).
- L. Hong, H. Wang, J. Cheng, L. Tang, J. Zhao, "Lowest-energy structures of $(MgO)_n$ $(n = 2 - 7)$ clusters from a topological method and first-principles calculations", *Computational and Theoretical Chemistry*, v.980, p.62 (2012).

Manuscripts in Process

- L. Hong, L. Hu, J. Freeland, J. Cabana, S. Öğüt, R. Klie, "Electronic structure of $LiCoO_2$ surfaces and effect of Al substitution", submitted to *Physical Review B* (2018).
- P. Yasaei, Z. Hemmat, C. Foss, S. Li, L. Hong, A. Behranginia, L. Majidi, R. Klie, M. Barsoum, Z. Aksamija, A. Salehi-Khojin, "Enhanced thermal boundary conductance in few-layer Ti_3C_2 MXene with encapsulation", accepted in *Advanced Materials* (2018).
- Z. Hemmat, P. Yasaei, J. Schultz, L. Hong, L. Majidi, A. Behranginia, L. Verger, N. Jiang, M. Barsoum, R. Klie, A. Salehi-Khojin, "Tuning thermal transport through atomically thin $Ti_3C_2T_z$ MXene by current-annealing in vacuum", submitted to *Science Advances* (2018).

- A. Hazarika, I. Fedin, L. Hong, J. Guo, V. Srivastava, J. Portner, I. Coropceanu, W. Cho, B. Diroll, G. Galli, R. Klie, D. Talapin, "Precisely engineered nano-heterostructures through colloidal Atomic Layer Deposition (c-ALD) with stationary phase reactants", submitted to *Nature Materials* (2018).
- V. Srivastava, V. Kamysbayev, L. Hong, E. Dunietz, R. Klie, D. Talapin, "Colloidal chemistry in molten salts: Synthesis of luminescent $In_{1-x}Ga_xP$ and $In_{1-x}Ga_xAs$ quantum dots", submitted to *Journal of the American Chemical Society* (2018).

Conference Proceedings

- L. Hong, L. Hu, J. Garcia, H. Iddir, S. Öğüt, J. Cabana, R. Klie, "Structural and magnetic properties of nanosized $LiCoO_2$ surfaces", submitted to *Microscopy and Microanalysis* (2018).
- L. Hong, D. Huber, R. Contreras-Guerrero, R. Droopad, R. Klie, "In-situ STEM-EELS observation of ferroelectric switching of $BaTiO_3$ film on GaAs", *Microscopy and Microanalysis*, v.23(S1), p.1628 (2017).
- L. Hong, R. Droopad, S. Öğüt, R. Klie, "Structural properties of $SrTiO_3$/GaAs hetero-interfaces", *Microscopy and Microanalysis*, v.22(S3), p.1454 (2016).
- L. Hong, S. Öğüt, R. Klie, "Transmission electron microscopic and first-principles study of $SrTiO_3$/GaAs hetero-interfaces", *Microscopy and Microanalysis*, v.21(S3), p.1647 (2015).

HONORS AND AWARDS

- M&M Student Scholar Award, *Microscopy Society of America and Microanalysis Society* (2017).
- Ovshinsky Student Travel Grant Award, *American Physical Society* (2016).
- Scholarship for Winter School on High Resolution Electron Microscopy, *Arizona State University* (2015).
- China MEMSIC Sensor Application Contest Silver Award, *Ministry of Education of China* (2011).

CONFERENCE PRESENTATIONS

- "Tailoring the properties of Al-doped $LiCoO_2$ surfaces", *American Physical Society March Meeting*, Baltimore, MD (Mar. 2016).
- (Awarded) "*In-situ* STEM-EELS observation of ferroelectric switching of $BaTiO_3$ film on GaAs", *Microscopy and Microanalysis Meeting*, St. Louis, MO (Aug. 2017).
- "Structural and electronic properties of $SrTiO_3$/GaAs hetero-interfaces", *Materials Research Society Spring Meeting*, Phoenix, AZ (Apr. 2017).
- "Structures, properties and defects of $SrTiO_3$/GaAs hetero-interfaces", *American Physical Society March Meeting*, New Orleans, LA (Mar. 2017).
- "Structural properties of $SrTiO_3$/GaAs hetero-interfaces", *Microscopy and Microanalysis Meeting*, Columbus, OH (Jul. 2016).
- (Awarded) "First-principles study of size- and edge-dependent properties of MXene nanoribbons", *American Physical Society March Meeting*, Baltimore, MD (Mar. 2016).
- "Transmission electron microscopic and first-principles study of $SrTiO_3$/GaAs hetero-interfaces", *Microscopy and Microanalysis Meeting*, Portland, OR (Aug. 2015).

WORKSHOPS AND TRAININGS

- Winter school on HREM and aberration-corrected STEM/TEM, LeRoy Eyring Center for Solid State Science at Arizona State University, Tempe, AZ (Jan. 2015).
- JEOL JEM-ARM200CF STEM and JEM-3010 TEM training, Research Resources Center at University of Illinois at Chicago, Chicago, IL (Jun. – Sept. 2014).